Forward Modelling of Transient Events in the Solar Atmosphere

Daniel James Price

Department of Physics

Aberystwyth University

June 2017

Supervisor: Dr Youra Taroyan

Thesis submitted for the degree of

Doctor of Philosophy

Word count of thesis: 26108

Declaration

This work has not previously been accepted in substance for any degree and is not concurrently submitted in candidature for any degree.

Signed ..... (candidate)

Date 16/06/2017

Statement 1

This thesis is the result of my own investigations, except where otherwise stated. Where correction services have been used, the extent and nature of the correction is clearly marked in a footnote(s). Other sources are acknowledged by footnotes giving explicit references. A bibliography is appended.

Signed ..... (candidate)

Date 16/06/2017

Statement 2

I hereby give consent for my thesis, if accepted, to be available for photocopying and for interlibrary loan, and for the title and summary to be made available to outside organisations.

Signed ..... (candidate)

Date 16/06/2017

Abstract

The solar atmosphere is a highly magnetised plasma covering a wide range of temperatures from the thousands of Kelvin to the millions. How exactly it reaches such extreme temperatures remains unknown. There are however numerous events that take place, concerned with the movement of energy and plasma throughout the solar atmosphere.

This thesis makes use of four instruments that have studied the Sun in the past, and in three cases continue to do so today. Observations from these instruments are combined with synthetic observations obtained from a detailed non-equilibrium ionisation hydrodynamic radiation code to understand the nature of what was observed and deduce physical information.

One study presents the replication of light curves of a loop obtained by the Atmospheric Imaging Assembly (AIA). It finds that it was a cold loop heated by a pulse of energy at its footpoint consistent with the energy of a nanoflare. Another study replicates line profiles of a structure observed by the Extreme-Ultraviolet Imaging Spectrometer (EIS) within an outflow region. We find that it is best modelled by a long loop consisting of at least 100 strands undergoing a cyclical process of heating and cooling on timescales of approximately 80 minutes. A final study replicates line profiles from the Solar Ultraviolet Measurements of Emitted Radiation (SUMER) instrument, and uses images from the Transition Region and Coronal Explorer (TRACE) to add context to the interpretation.

Acknowledgements

First I would like to thank my supervisor Youra Taroyan for his extensive guidance and limitless availability, I may have been your first PhD student but I would never have been able to tell. I look forward to our collaborations continuing long into the future.

My eternal gratitude goes out to my parents, Angela and Adrian, for their unwavering support and encouragement over the years. I certainly would not have gotten to this point without you, and I really cannot thank you enough.

It has been a genuine pleasure getting to know my fellow PhD students here in Aberystwyth and elsewhere. I have to thank Ben, Doğa, Drew, Dylan, Jay, Joe, Nathan, Patrick, Rose, Tom, and Zoë for making the past four years unforgettable. I am a better person for knowing each of you.

I would like to thank my co-authors for their time and patience in the publishing of our papers. In particular Steve Bradshaw for providing me with his HYDRAD code, which is used extensively throughout this thesis, and his timely assistance with it when needed.

This work was all made possible by a PhD studentship funded by the Science and Technology Facilities Council. CHIANTI is a collaborative project involving George Mason University, the University of Michigan (USA), and the University of Cambridge (UK). SDO data is courtesy of NASA/SDO and the AIA, EVE, and HMI science teams. Hinode is a Japanese mission developed and launched by ISAS/JAXA, with NAOJ as domestic partner and NASA and UKSA as international partners. It is operated by these agencies in co-operation with ESA and NSC (Norway).

Contents

List of Figures

List of Tables

Citations to Previously Published Work

Chapter 3 and portions of Section 2.5 appear in the following:

Price, D. J., Y. Taroyan, D. E. Innes, and S. J. Bradshaw (2015), "Forward Modelling of a Brightening Observed by AIA." *Solar Phys.*, 290, 1931-1945

Portions of Chapter 4 appear in the following:

Price, D. J. and Y. Taroyan (2015), "Physics of outflows near solar active regions." *Ann. Geophys.*, 33, 25-29

Chapter 1

Introduction

The Sun is a key feature of human civilization, continually basking the Earth with energy that goes on to be used in a multitude of ways whether as heat, for photosynthesis in plants, or even electricity. The Sun has been recognised as a significant entity throughout our history, being present in ancient paintings, illuminating monuments during certain times of the year, and being increasingly studied.

The core of the Sun is approximately the innermost 25% region (García et al., 2007) where nuclear fusion is continually converting hydrogen into helium and releasing vast amounts of energy primarily through the proton-proton chain reaction and much less significantly the CNO cycle (Figure 1.1; Adelberger et al., 2011). The 15 MK core temperature and the 1.6×10^5 kg m^{-3} central density allow the reaction to take place (Priest, 2014). Like the rest of the solar interior, it is not possible to directly observe the core as no radiation escapes the interior. Instead, properties of the interior are inferred indirectly based on the observable effects of its behaviour. The two key sources of information on the interior are solar oscillations and solar neutrinos (Phillips, 1992).

The radiative zone extends from above the core until approximately 0.7 $R_\odot$ (García et al., 2007) and is where the energy is primarily conveyed outward by radiation as photons rather than by convection. It is mostly made up of protons and high-energy electrons, making collisions highly probable for photons resulting in them taking on the order of tens of thousands of years to reach the photosphere

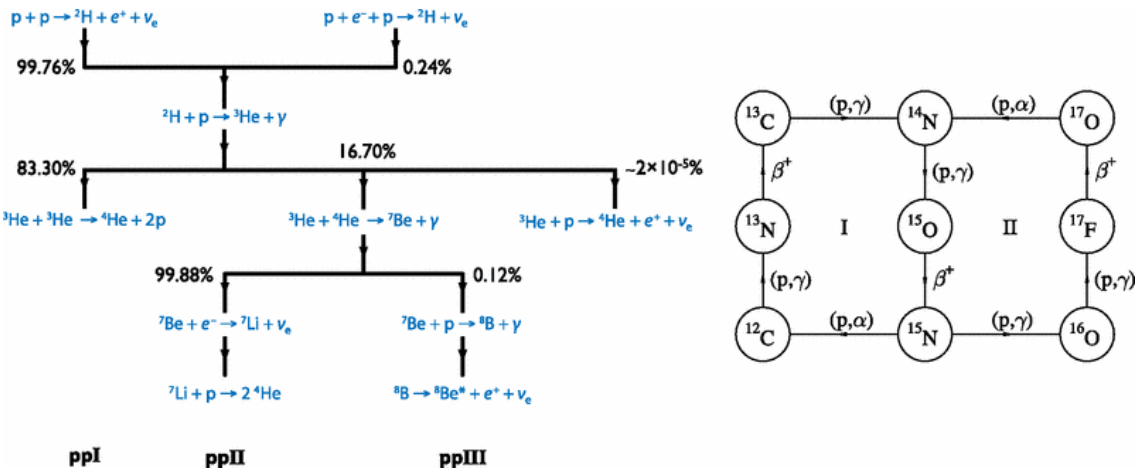

Figure 1.1: The left image shows three main cycles making up the proton-proton chain reaction, plus a minor branch on the right which creates the most energetic neutrinos. Here the percentages indicate how often the reactions proceed down that route, for example the first row indicates that ^{2}H is produced by the reaction on the left 99.76% of the time. The right image shows the CNO-I and CNO-II cycles. Reprinted figure with permission from E. G. Adelberger et al., Reviews of Modern Physics, 83, 201, 2011, `https://dx.doi.org/10.1103/RevModPhys.83.195`. Copyright 2011 by the American Physical Society.

(Mitalas and Sills, 1992). Due to the high frequency of collisions here, resulting in scattered or re-emitted photons, energy transport is dominated by radiation.

Above this up until the surface sits the convective zone where the reverse is true, in that the energy transport is dominated by convective processes rather than radiative. Here the plasma carries heat as it rises towards the surface before losing a portion of it and falling back down to collect more. By the time they reach the surface, the gamma rays generated in the core turn into visible light due to the photons being continually absorbed and re-emitted on the way.

The photosphere is the layer of the Sun generally considered to be the surface for the sake of defining the solar radius and other such values. This, the first layer of the solar atmosphere only a few hundred kilometres thick, is defined by its low optical depth which allows visible light to escape the Sun. The increasing opacity with depth is due to the rising abundance of H^- ions whose additional electron is easily displaced, allowing them to readily absorb photons over a wide range of energies. This change in abundance results in a range of temperatures from approximately 6400 K at the base of the photosphere to approximately 4400 K at the top (Phillips,

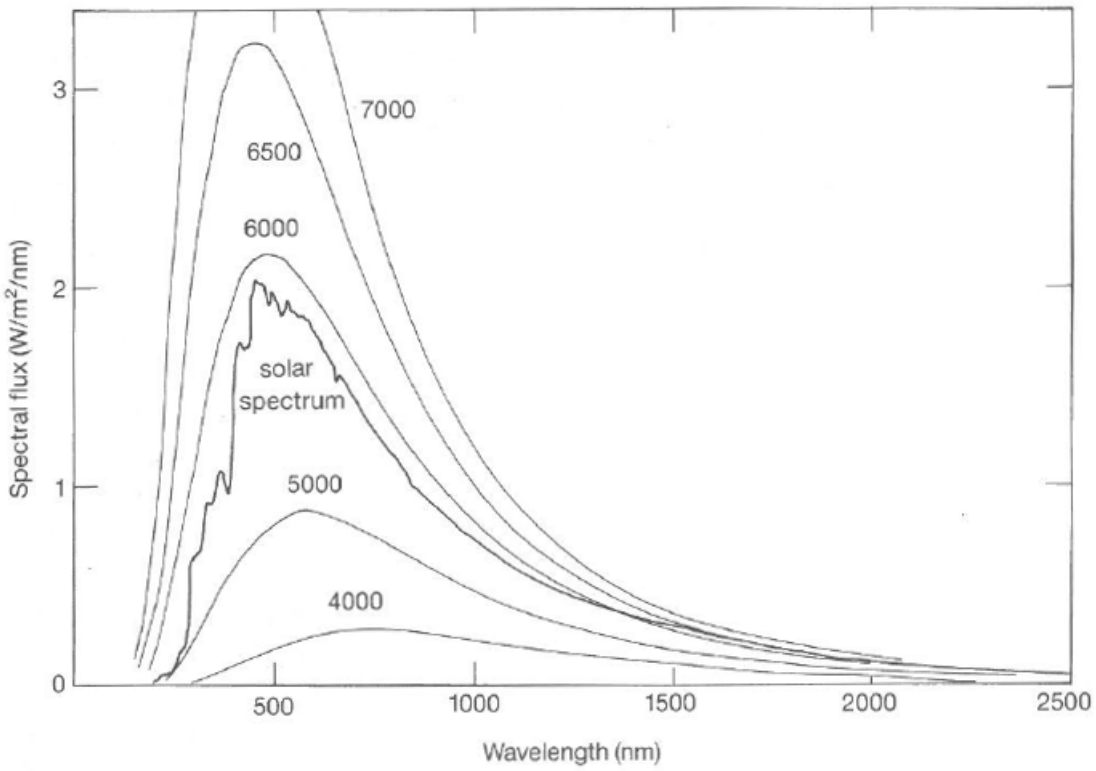

Figure 1.2: Spectrum of the radiation of the photosphere displayed as spectral flux against wavelength. For comparison, black body lines from Labs and Neckel (1968) are plotted with their absolute temperatures indicated in Kelvin. Reprinted figure with permission from K. J. H. Phillips, Guide to the Sun, 1992, New York, NY: Cambridge University Press. Copyright 1992 by Cambridge University Press.

1992), where there is a temperature minimum region due to the temperature then rising in the higher layers of the atmosphere. The emission from the photosphere resembles quite closely that of a black body (Figure 1.2). Therefore by taking the total solar flux of the Sun in all wavelengths and then assuming the Sun to be a black body, one can calculate the effective temperature to be 5778 K (Phillips, 1992).

A small-scale magnetic field pervades the photosphere. It is not a uniform field however, and gives rise to phenomena visible on the surface. Where there are particular concentrations of magnetic flux a black dot, known as a sunspot, can be seen in visible light. These consist of a dark core called the umbra which is surrounded by the lighter, though still darker than the photosphere, penumbra. Typically sunspots form in pairs of opposite polarity, however they can also form in complex groups.

The much less dense, hotter, chromosphere sits above the photosphere. This low density usually renders it visually unobservable due to the overwhelming emission of the photosphere, but during solar eclipses the moon blocks out the photosphere revealing the chromosphere as red flashes around the edge of the disk. Full disk observations are commonly carried out by applying a Hα filter or by using the strong Ca II H and K Fraunhofer lines. Here the temperature rises with height in contrast to the photosphere.

Observing the chromosphere in Hα reveals spicules, fine jet-like strands around the edge of the disk (see Sterling (2000) for a review of spicules). Consisting of magnetic flux tubes containing plasma, spicules are capable of extending into the corona with an average temperature of 10^4 K (Stix, 2004). More recently de Pontieu et al. (2007) found there to be two distinct types of spicules with the key difference being that the original type I spicules move up and down while the new type II spicules fade from view.

The transition region is a layer of highly variable thickness where the temperature sharply rises from the chromosphere into the corona. The jump from the approximately 10^4 K chromosphere to the approximately 10^6 K corona can be so sharp that it is appropriate to regard the transition region as a temperature regime

(Stix, 2004). It is here that explosive events were originally discovered by Brueckner and Bartoe (1983) in spectra of transition region lines. They are not strictly defined, but can be characterised by their line profiles possessing strong non-Gaussian wing enhancements resulting from a high velocity component (Bewsher et al., 2005). Explosive events in active regions were found to be associated with transition region loop brightenings by Huang et al. (2017).

The corona is the uppermost layer of the solar atmosphere, here we find the greatest temperatures and the lowest densities. The extent of the corona is not easily defined as it technically extends to the edge of the solar system, but it is generally considered to be within a few solar radii of the Sun past which the density noticeably drops with distance making up the solar wind. The high temperatures result in the corona, comprised mostly of hydrogen, being a fully ionised plasma. Consequently, despite the corona producing much less radiation compared to the photosphere, its radiation covers a much wider range of wavelengths (Phillips, 1992).

That the temperature of the solar atmosphere remains above 1 million Kelvin and does not fall off with distance as one would expect is the essence of the coronal heating problem. If the corona was purely heated by radiation from below then reaching millions of Kelvin would not be possible. This leads to the conclusion that other mechanisms of heating must be at work to sustain the high temperatures of the corona and to balance the losses suffered through thermal conduction and radiation. Determining what these mechanisms are and how they operate is still very much an active field today with no conclusive theory of coronal heating yet put forward.

One such mechanism, under steady investigation since being proposed by Parker (1988), is nanoflares. These are small bursts of energy on the order of around 10^{24} erg, originally proposed to be the result of reconnection caused by random photospheric motions braiding magnetic field lines. However the term today refers to any impulsive mechanism delivering energy in that range. The heating of the corona by such events was found to have theoretical backing by Browning et al. (2008), while more recently Klimchuk and Bradshaw (2014) concluded that chromospheric

nanoflares are not a primary source of hot coronal plasma as opposed to nanoflares occurring higher up in the corona. Ding et al. (2011) showed that plasma outflows in the chromosphere and transition region can be efficiently driven by magnetic reconnection.

Alfvén waves have also been proposed as the source of coronal heating (Wentzel, 1974, 1976), however their weak damping means that actually imparting their energy into the corona is troublesome. To enhance the dissipation of these waves, the resonant absorption (Ionson, 1978) mechanism was derived whereby in some circumstances Alfvén waves can be in resonance with local oscillations allowing for the energy to transfer into the local oscillations and thus dissipate more effectively at the smaller scales. Based on the same property, that individual surfaces within an inhomogeneous plasma can oscillate with their own Alfvén frequency, phase mixing (Heyvaerts and Priest, 1983) also attempts to enhance Alfvén wave dissipation. This mechanism underlines how Alfvén waves on neighbouring field lines slowly become out of phase, which generates increasingly large transverse gradients until dissipative length scales are reached.

Active regions make up a small portion of the solar atmosphere but contain most of the activity. Located where the magnetic field is strongly concentrated, they are visible above sunspot groups. As an area home to mainly closed magnetic field lines it plays host to a range of processes, due to the continual magnetic activity of the Sun and the high concentration of field lines, such as flares and coronal mass ejections.

Coronal holes make up the darker northern and southern poles of the Sun. They are dominated by open magnetic field lines that allow for plasma to leave the Sun and flow into the solar wind, resulting in their diminished brightness. They are detectable across a range of wavelengths, but appear clearest in soft X-ray images.

The areas outside of active regions were historically called quiet Sun regions, however this has since been found to be a misleading name due to the wide range of dynamic activity discovered to be taking place there. This blurs the lines between

the quiet Sun and active regions somewhat, a modern definition is that the quiet Sun consists of all closed magnetic field regions except for active regions (Aschwanden, 2006).

Coronal loops are magnetic flux tubes anchored at both ends to the photosphere that contain plasma. They appear as bright closed arches in the corona because of the increased pressure and density of the contained plasma relative to that of the tenuous corona. There is still much to understand about the underlying mechanisms that result in the filling of such flux tubes. However coronal loops are intensely studied to identify how they contribute to coronal heating. This is because they provide an avenue for relatively cold chromospheric plasma to shoot up to coronal heights and temperatures. Loops are generally classified thermally into three broad groups, hot loops observed best in soft X-rays at 2 MK or above, warm loops best observed in EUV bands at around 1 MK, and cool loops observed in UV lines at 10^5–10^6 K. Reale (2014) suggested that these differences may be more substantial with different classes of loops potentially being governed by different physical processes.

This thesis uses powerful numerical simulations to reproduce solar events observed by a number of the above satellites, of which greater details follow. The combination of the numerical and the observational yields greater results than focusing on just one or the other. The numerical helps to understand what has been observed, and the observations act as a target constraining the simulations to ensure their veracity. The first study reproduces the light curves of a loop that was heated by an explosive event using a single heating pulse at the footpoint of the loop, the second study replicates the line profiles of a structure observed within a complicated outflow region, and the final study reproduces the line profiles of an observed loop believed to have multiple pulses occurring along its length.

Chapter 2

Instrumentation & Software

Space based observations of the Sun have been taking place since 1946 when a team from the US Naval Research Laboratory (NRL) was allowed to place an instrument on a V2 rocket launched by the US Army. These were followed by a series of eight Orbiting Solar Observatory (OSO) satellites launched from 1962–1975, which allowed for longer observations than are possible from a sounding rocket. The US space station Skylab, carrying the Apollo Telescope Mount (ATM) which operated from 1973–1974 with an array of eight instruments observing the Sun in X-ray, EUV, UV, and white light, was a big step forward in solar physics returning the first images of the Sun in detail. The Solar Maximum Mission (SMM), a satellite dedicated to solar observations lasting from 1980–1989, expanded on the observing capabilities of the ATM by additionally observing in gamma-ray and infrared wavelengths. The Yohkoh satellite operated from 1991–2001 carrying four instruments with a heavy, but not complete, focus on X-ray wavelengths. The Solar and Heliospheric Observatory (SOHO) was launched in 1995 with twelve instruments for observing the solar atmosphere, monitoring the solar wind, and helioseismology and it remains operational at the time of writing. The Transition Region and Coronal Explorer (TRACE) followed from 1998–2010 and was comprised of a single telescope designed to provide unprecedented spatial resolution. Hinode was launched in 2006 to study the Sun's magnetic fields as the successor to Yohkoh and continues to operate at the time of writing. The Solar Dynamics Observatory (SDO) was launched

in 2010 and is also currently operational, providing full-disk observations with its three instruments.

The technological capabilities of space based solar observation satellites have increased with time, with each advancement revealing new information. Continuing improvement in areas such as spatial resolution and temporal cadence is essential for completing our understanding of the Sun. For example Doyle et al. (2012) found that increases in the intensity of transition region spectral lines on a subsecond timescale could be explained through transient ionisation, but at the time of publication no spectrographs were capable of carrying out observations at a high enough cadence to diagnose it.

2.1 Solar and Heliospheric Observatory

The Solar and Heliospheric Observatory (SOHO) is a joint project of ESA and NASA launched in 1995 to study the Sun. While originally planned to be a two year mission it has been repeatedly extended and continues to operate twenty years later. The satellite carries three helioseismology experiments, Global Oscillations at Low Frequencies (GOLF; Gabriel et al., 1995), Variability of solar IRradiance and Gravity Oscillations (VIRGO; Fröhlich et al., 1995), and the Michelson Doppler Imager (MDI; Scherrer et al., 1995). There are a further six instruments for solar atmosphere remote sensing investigations, Solar Ultraviolet Measurements of Emitted Radiation (SUMER; Wilhelm et al., 1995), the Coronal Diagnostic Spectrometer (CDS; Harrison et al., 1995), the Extreme-ultraviolet Imaging Telescope (EIT; Delaboudinière et al., 1995), the UltraViolet Coronagraph Spectrometer (UVCS; Kohl et al., 1995), the Large Angle and Spectrometric COronagraph (LASCO; Brueckner et al., 1995), and Solar Wind ANisotropies (SWAN; Bertaux et al., 1995). Finally there are three solar wind 'in-situ' instruments, the Charge, ELement and Isotope Analysis System (CELIAS; Hovestadt et al., 1995), the COmprehensive SupraThermal and Energetic Particle analyser (COSTEP; Müller-Mellin et al., 1995), and the Energetic and Relativistic Nuclei and Electron experiment (ERNE; Torsti et al., 1995). The satellite

orbits around the L_1 Lagrangian point allowing it to continuously observe the Sun (Domingo et al., 1995).

2.1.1 Solar Ultraviolet Measurements of Emitted Radiation

The SUMER instrument is a ultraviolet spectrograph used to study the solar chromosphere, transition region, and low corona. It can obtain spectra and monochromatic images. It has two detectors with differing wavelength ranges, and only one can be operated at a time. Detector A can record first order lines from 780 Å to 1610 Å and second order lines from 390 Å to 805 Å, while detector B can record from 660 Å to 1500 Å and 330 Å to 750 Å respectively. The spectrograph has an angular resolution of close to $1''$, spectral resolutions in the vicinity of 43 mÅ (1st order) and 22 mÅ (2nd order) which vary by wavelength observed, and a temporal resolution down to 1 s or 60 ms in the case of certain observations.

The spectrograph mainly consists of two parabolic mirrors, a plane mirror, and a spherical concave grating which optionally feeds into one detector or the other. The first parabolic mirror is capable of pointing adjustments in two perpendicular directions of $\pm 32'$, and can be used to compensate for solar rotation or to raster areas of the Sun. The pointing is verified with the help of a visible light rear slit camera.

2.2 Transition Region and Coronal Explorer

The Transition Region and Coronal Explorer (TRACE) was a NASA satellite that observed the Sun from 1998 until 2010. It was placed in a Sun-synchronous polar orbit to allow it to cycle between approximately 7–9 months of uninterrupted observing and an eclipse season each year. The satellite itself was the sole instrument, housing a Cassegrain telescope with a field of view equivalent to one-tenth of the solar disk ($8.5' \times 8.5'$) at a $1''$ resolution and $0.5''$ pixel size with typical temporal resolutions of less than 1 minute. A guide telescope and limb sensor on top of the

Channel (Å)	Bandwidth (Å)	Primary ion(s)	$\log_{10}$T (K)
171	6.4	Fe IX/X	5.2–6.3
195	6.5	Fe XII/XXIV	5.7–5.7, 7.0–7.4
284	10.7	Fe XV	6.1–6.6
1216	84	H I Lα	4.0–4.5
1550	30	C IV	4.8–5.4
1600	275	UV cont., C I, Fe II	3.6–4.0
1700	200	continuum	3.6–4.0
5000	broad	white light	3.6–3.8

Table 2.1: The primary ions, their wavelengths, bandwidth, and temperatures as observed by TRACE (Handy et al., 1999).

main telescope were used for pointing. It imaged the photosphere, transition region, and corona using three extreme-ultraviolet wavelengths (171 Å, 195 Å, and 284 Å), four ultraviolet wavelengths (1216 Å, 1550 Å, 1600 Å, and 1700 Å), and white light (5000 Å) as detailed in Table 2.1 (Handy et al., 1999).

2.3 Hinode

Hinode is a Sun observation satellite launched by JAXA in collaboration with NAOJ, NASA, and STFC (UK). It consists of three instruments, the Solar Optical Telescope (SOT; Tsuneta et al., 2008), the X-ray Telescope (XRT; Golub et al., 2007), and the Extreme-Ultraviolet Imaging Spectrometer (EIS; Culhane et al., 2007). Operating since 2006 it sits in a Sun-synchronous orbit that allows it to collect near-continuous observations of the Sun.

2.3.1 Extreme-Ultraviolet Imaging Spectrometer

The EIS instrument is an extreme ultraviolet spectrometer that observes coronal and upper transition region emission lines within two wavelength bands, 170–210 Å and 250–290 Å. The bands were chosen to allow for the detailed measurement of plasma properties, flow velocities and non-thermal plasma processes in particular. The instrument has a spatial resolution of 2″ (pixel size 1″), a field of view of 360″ × 512″, a spectral resolution of approximately 25 km s^{-1} pixel^{-1}, and a temporal resolution

of approximately 1–10 s depending on the observing mode used.

Notably the spectrometer operates at normal incidence due to using multilayer coatings on both the mirror and the grating, plus thinned back-illuminated CCDs. The coatings result in the narrow passbands, but they were accepted for the purposes of high throughput. An electric drive to rotate the primary mirror provides the raster capability of the instrument.

2.4 Solar Dynamics Observatory

The Solar Dynamics Observatory (SDO) is a NASA satellite that has been observing the Sun since 2010. It contains three instruments, the Helioseismic and Magnetic Imager (HMI; Scherrer et al., 2012), the Extreme Ultraviolet Variability Experiment (EVE; Woods et al., 2012), and the Atmospheric Imaging Assembly (AIA; Lemen et al., 2012). The satellite sits in an inclined geosynchronous orbit that allows it to maintain continuous contact with its ground station. This was necessary due to the large data rate making onboard storage and temporary downlinks impossible (Pesnell et al., 2012).

2.4.1 Atmospheric Imaging Assembly

The full-disk of the Sun is continuously observed by AIA, providing 4096 × 4096 pixel images for ten wavelengths with a pixel size of 0.6″ and resolution of 1.5″. The bulk of the wavelengths are seven in the extreme-ultraviolet range, centred on 94 Å, 131 Å, 171 Å, 193 Å, 211 Å, 304 Å, and 335 Å observed at a cadence of 12 s. It also takes two images centred on the ultraviolet wavelengths of 1600 Å and 1700 Å at a cadence of 24 s, and the continuum observed at 4500 Å with a cadence of 1 hour. Their associated primary ions and characteristic temperatures are given in Table 2.2, while example images are given by Figure 2.1. A detailed breakdown of the contributions made to the channels by spectral lines and continuum emission is given by O'Dwyer et al. (2010). The range of temperatures covered, combined with

Channel (Å)	Primary ion(s)	Region of atmosphere	$\log_{10}$T (K)
4500	continuum	photosphere	3.7
1700	continuum	temperature minimum, photosphere	3.7
304	He II	chromosphere, transition region	4.7
1600	C IV + cont.	transition region, upper photosphere	5.0
171	Fe IX	quiet corona, upper transition region	5.8
193	Fe XII, XXIV	corona and hot flare plasma	6.2, 7.3
211	Fe XIV	active-region corona	6.3
335	Fe XVI	active-region corona	6.4
94	Fe XVIII	flaring corona	6.8
131	Fe VIII, XXI	transition region, flaring corona	5.6, 7.0

Table 2.2: The primary ions and their wavelengths, typical regions, and characteristic temperatures, observed by AIA (Lemen et al., 2012).

the high temporal and spatial resolutions, results in AIA being an invaluable tool for any research requiring images of the Sun.

The instrument is made up of four telescopes, each with a primary mirror and an active secondary mirror. Paired with a dedicated guide telescope, the secondary mirror works to stabilise the image on the CCD which is protected from charged particles by interior baffles. The mirrors have multilayer coatings that are optimised for their respective EUV wavelengths. Three of the telescopes have two different EUV band passes, while the fourth possesses one plus the remaining three UV wavelengths.

2.5 Hydrodynamics and Radiation Code

All loop simulations within this thesis were carried out using the one-dimensional hydrodynamics and radiation code HYDRAD (Bradshaw and Mason, 2003a,b; Bradshaw and Cargill, 2013). It first generates a set of initial conditions from a series of specified parameters, and then proceeds to evolve the loop over time according to further settings. The code is able to consider the first thirty elements of the periodic table to be in either equilibrium or non-equilibrium, however we consider only the fifteen most abundant elements in the solar atmosphere due to their majority and to save computational time. Key features for this work include the non-equilibrium

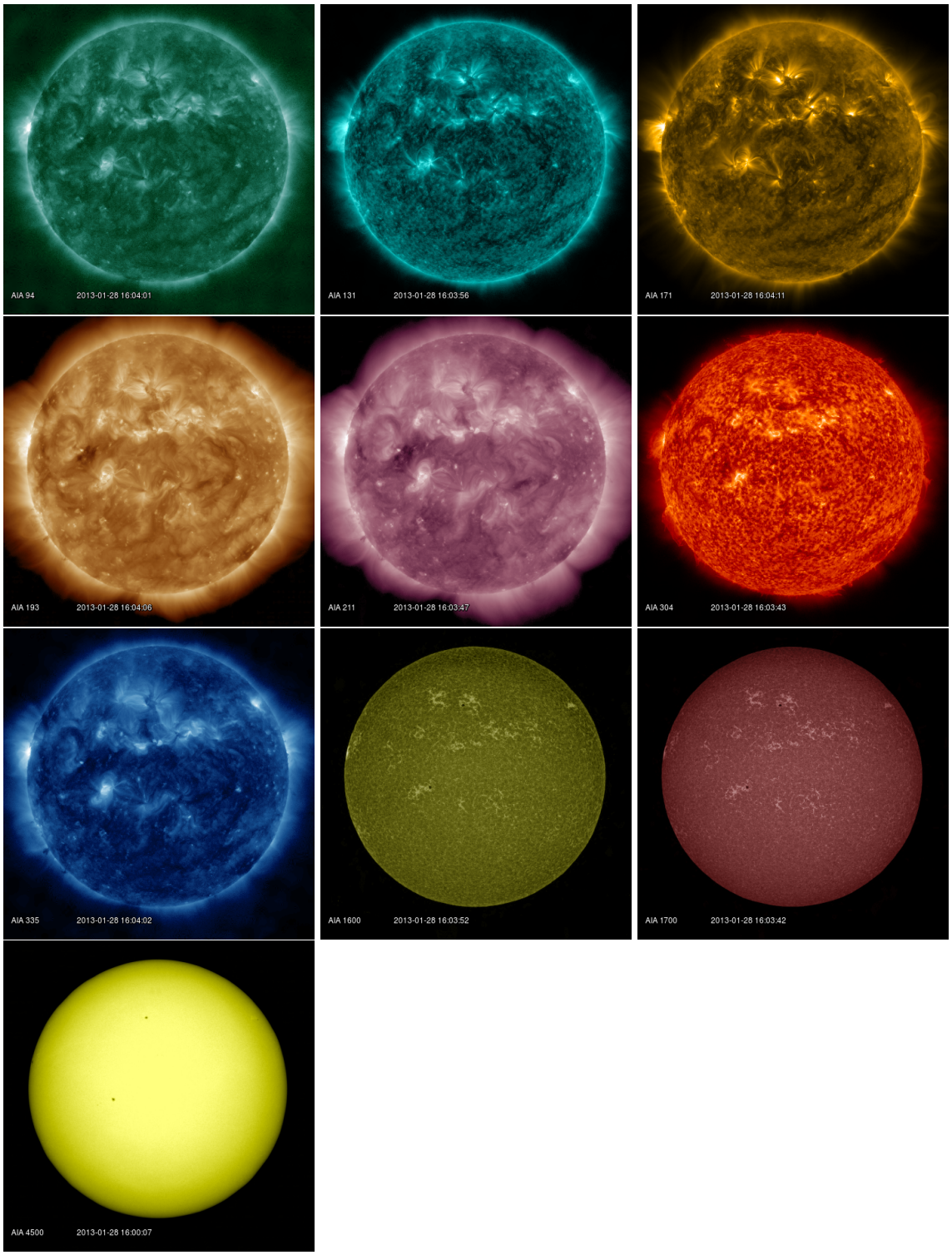

Figure 2.1: Example images from each of the AIA filters. Courtesy of NASA, created using Helioviewer.

capability and the adaptive mesh because it allows the code to accurately maintain a high resolution representation of the sensitive transition region during periods of heating (Taroyan and Erdélyi, 2009). The importance of considering non-equilibrium ionisation when modelling solar transient events was demonstrated by Roussev et al. (2001). Doyle et al. (2012) showed the importance of non-equilibrium effects, namely transient ionisation, when studying transition region intensities. Inadequate resolution of the transition region has been found to primarily lead to underestimated coronal density by Bradshaw and Cargill (2013), and others, which would have knock on effects to the results.

The code solves the conservative form of the hydrodynamic equations and a detailed ionisation balance equation for each ion:

$$\frac{\partial \rho}{\partial t} + \frac{\partial}{\partial s}(\rho \upsilon) = 0, \tag{2.1}$$

$$\frac{\partial}{\partial t}(\rho \upsilon) + \frac{\partial}{\partial s}(\rho \upsilon^2) = \rho g_{\parallel} - \frac{\partial P}{\partial s} + F, \tag{2.2}$$

$$\frac{\partial E}{\partial t} + \frac{\partial}{\partial s}[(E+P)\upsilon] = \rho \upsilon g_{\parallel} + \frac{\partial}{\partial s}\left(\kappa T^{5/2}\frac{\partial T}{\partial s}\right) + E_H(s,t) - E_R(s,t), \tag{2.3}$$

$$E = \frac{1}{2}\rho \upsilon^2 + 3k_B n T, \tag{2.4}$$

$$P = 2k_B n T, \tag{2.5}$$

$$\frac{\partial Y_i}{\partial t} + \frac{\partial}{\partial s}(Y_i \upsilon) = n(I_{i-1}Y_{i-1} + R_i Y_{i+1} - I_i Y_i - R_{i-1}Y_i). \tag{2.6}$$

ρ denotes the mass density; υ the bulk velocity; P the total pressure; T the temperature; $g_{\parallel}$ the gravitational acceleration parallel to the magnetic field; k_B the Boltzmann constant; κ the coefficient of thermal conductivity; E_H the volumetric heating rate consisting of time-independent uniform heating and a time-dependent impulsive heating rate; E_R the radiative energy loss rate, which assumes optically thin emission and a fully ionised plasma, as a function of s and t accounting for the non-equilibrium state of the ions; Y_i the fractional population, normalised to 1, of ion stage i of element Y; I_i and R_i are the ionisation and recombination rates

from/to ion stage i; n is the electron number density; and F is a forcing term that drives cold plasma injection. Note that the second term of the energy equation (2.4) is the sum of the electron and ion thermal energies. Also the forcing term is zero for impulsive heating, and the time-dependent impulsive heating rate is zero for cold plasma injection.

Elements were considered to be in equilibrium for the generation of initial conditions however all ensuing simulations were carried out under full non-equilibrium ionisation. This was necessary to ensure the simulations painted a realistic picture of the evolution of the loops because the assumption that the ion populations remain in equilibrium does not hold once a heating pulse is introduced to a stable loop. Borrini and Noci (1982) reported considerable deviation from equilibrium in loops characterised by high-speed flows, especially in cold loops, as a result of the greater temperature and density gradients involved. Bradshaw (2009) concluded that rapid heating can still result in a lack of equilibrium even at high densities around 10^{10} cm^{-3}, although the differences decrease with increasing density.

An important feature of HYDRAD is its handling of heating, allowing for time-independent background heating and time-dependent heating pulses. These dynamic heating pulses can be introduced to the loop with specified volumetric heating rates, spatial locations, spatial scales, and temporal profiles. It is possible to adjust the governing equation but it was fixed as follows for this work:

$$E_t = E_0 \exp\left[-\frac{(s-s_0)^2}{2(s_H)^2}\right] \begin{cases} \frac{(t-t_0)}{(t_1-t_0)} & t_0 < t < t_1 \\ 1 & t_1 \leq t \leq t_2 \\ 1 - \frac{(t-t_2)}{(t_3-t_2)} & t_2 < t < t_3 \end{cases} \tag{2.7}$$

where E_t denotes the heating energy per unit area due to the pulse at time t; E_0 the impulsive heating rate; L the length of the loop; s the loop position; s_0 the heating location; s_H the heating scale length; t_0 the time the heating rise phase begins; t_1 the time the heating rise phase ends; t_2 the time the heating decay phase begins; and t_3 the time the heating decay phase ends.

The output physical and ion data can then be fed into the forward modelling part of the code for comparison to observations by instruments. They are combined with instrumental response functions and ion emissivity tables to generate intensity in units of DN s^{-1} $pixel^{-1}$ by:

$$I(\lambda, n, T) = \frac{0.83 \times G(\lambda) \times Ab(Y) \times Y_i \times \epsilon(\lambda, n, T) \times \langle EM \rangle}{4\pi \times (\frac{hc}{\lambda})} \tag{2.8}$$

$G(\lambda)$ denotes the instrumental response function in DN $pixel^{-1}$ $photon^{-1}$ sr cm^2; $\frac{hc}{\lambda}$ the photon energy in erg; 0.83 the ratio of protons to electrons; $Ab(Y)$ the abundance of element Y relative to hydrogen; Y_i the population fraction of charge state i of element Y; $\epsilon(\lambda, n, T)$ the emissivity of the line in erg s^{-1} cm^3; and $\langle EM \rangle$ the spatially averaged column emission measure in the pixel, in units of cm^{-5}.

The response functions in the case of imagers, such as AIA, are a product of the plate scale, effective area, and gain of the instrument (Bradshaw and Klimchuk, 2011). This allows for the modelled intensity to be directly compared to the real observed intensity. However for spectrographs we set the response functions to a value of one meaning that relative intensities must be used. The intensities can be used in conjunction with the physical data from the original simulation to calculate a range of variables for further comparisons to observations such as the Doppler shift or the Doppler width.

Chapter 3

Forward Modelling of a Brightening Observed by AIA

A comprehensive understanding of the different transient events is necessary for any eventual solution of the coronal heating problem. We present a cold loop whose heating caused a short-lived small-scale brightening that was observed by AIA. The loop was simulated using an adaptive hydrodynamic radiation code that considers the ions to be in a state of non-equilibrium. Forward modelling was used to create synthetic AIA intensity plots, which were tested against the observational data to confirm the simulated properties of the event. The hydrodynamic properties of the loop were determined. We found that the energy released by the heating event is within the canonical energy range of a nanoflare.

3.1 Introduction

The underlying cause of coronal heating is a long-standing problem whose solution continues to elude the scientific community. In theory it should be a simple matter to account for the 0.01% of solar output (Golub and Pasachoff, 1997) that is required to sustain the corona. However, in reality, the Sun is a very dynamic and complicated stellar object, which makes the task more difficult than first thought. A comprehensive understanding of the multitude of solar phenomena, and the movement of

energy that comes with them, is essential for solving the problem.

Coronal loops are one such phenomenon, linking the photosphere to the corona, potentially providing a conduit for the energy of the solar interior to reach the atmosphere. Extensive overviews of coronal loops are given by Bray et al. (1991), with Reale (2014) specifically addressing them as bright structures confining plasma, while insight into their structure is given by Peter et al. (2013). Reale et al. (2000) presented detailed modelling of a coronal loop that was found to be impulsively heated.

Small bursts of energy of around 10^{24} erg, called nanoflares, are potential candidates for the source of coronal heating, as originally proposed by Parker (1988). Originally referring solely to energy release through magnetic reconnection, the term nanoflare now encompasses any impulsive mechanism that delivers energy in that range, for example, heating by Alfvén waves (Moriyasu et al., 2004). It has yet to be confirmed as the source of coronal heating despite studies of the frequency distribution of thermal energies for hard X-ray flares (Crosby et al., 1993), active region transient brightenings (Shimizu, 1995), and quiet-Sun nanoflares and microflares (Krucker and Benz, 1998; Parnell and Jupp, 2000; Aschwanden et al., 2000; Benz and Krucker, 2002; Aschwanden and Parnell, 2002; Taroyan et al., 2011). However, it remains an open avenue of investigation.

As with any phenomenon that involves energy release, explosive events are also of interest to those investigating heating. Explosive events are defined by their non-Gaussian line profiles and short-lived nature. Since their discovery by Brueckner and Bartoe (1983), they have been the focus of numerous studies. Dere et al. (1991) used explosive events to examine magnetic reconnection by assuming that they are all the result of reconnection. Innes and Tóth (1999) conducted simulations of explosive events to examine the behaviour of temperature emission lines from reconnection. Winebarger et al. (2002) explored the energetics of explosive events and found that individual events were not energetically significant with regard to coronal and chromospheric heating. Teriaca et al. (2002) analysed spectral lines to

determine whether or not transition region explosive events have coronal counterparts. Teriaca et al. (2004) found cases where supersonic flows in small loops were associated with non-Gaussian line profiles. More recently, Madjarska et al. (2009) have demonstrated that explosive events and other transient phenomena may be the same processes, but observed in different ways.

The differences between non-equilibrium ionisation and local thermodynamic equilibrium modelling have been known for some time, with Mariska et al. (1982) finding substantial differences in relative ionic abundances of the quiet Sun. Müller et al. (2003) investigated the effects of non-equilibrium ionisation on condensation in transition region spectral lines. Bradshaw and Cargill (2006) found significant departure from equilibrium in models of coronal loops heated by nanoflares. In this work we factor in the effects of non-equilibrium ionisation by using the established HYDRAD code (Section 2.5) for our simulations and modelling.

In the following work we investigate a pair of brightenings reported by Innes and Teriaca (2013) that are believed to have occurred in a loop. Hydrodynamic simulations combined with forward modelling allow us to replicate the observations and suggest physical parameters such as density, loop temperature, loop length, and heating rate. The initial brightening represents a nanoflare that subsequently caused the second brightening through a heating pulse in the loop. This is supported by the results of Winebarger et al. (2013), who found that cool dense loops were impulsively heated by nanoflares.

3.2 Observations

A pair of explosive events were observed by Innes and Teriaca (2013) using SUMER (Section 2.1.1), and then co-aligned with corresponding data from AIA (Section 2.4.1). Both explosive events were associated with small-scale brightenings in the AIA data. There was a delay of 60 s between the AIA brightenings at the two sites, and each brightening coincided with an explosive event. The authors therefore concluded the likely cause to be a brightening that released energy at a loop footpoint and drove

a flow along to the other footpoint where the second brightening took place. There was a delay between the two explosive events seen by SUMER, but due to the 60 s exposure time, the exact length of time could not be determined. It is reasonable to assume, however, that the delay is similar to the delay between the two brightening peaks. Because of the long exposure time used for the SUMER data, we only make use of the AIA data due to the short-lived nature of the events.

Additional evidence for the involvement of a loop is shown by Figure 3.1, where the two sites of the brightenings are connected by a band of increased emission shortly after the appearance of both sites. By considering the Sun to be flat in the relatively small area covered and using basic geometry, it is possible to obtain a simple approximation for the length of the loop. Earlier observations indicate that the loop is not observed before the two brightenings appear.

Sets of AIA data were plotted onto intensity maps with a pixel size of $0.6''$ (Figure 3.1). A square of three by three pixels centred on each footpoint was summed and divided by the duration of the observations to create plots of intensity in units of DN against time in seconds (Figure 3.2). The intensity between the footpoints was also examined, but it did not accurately represent the loop structure, therefore we did not analyse it here. The discrepancy may be due to the greater column depth of material making up the observations at the footpoints compared to the middle of the loop, resulting in more background contamination of the intensity in the middle. This was carried out for the 304 Å, 171 Å, 193 Å, and the 131 Å extreme ultraviolet channels. While the event was also visible in the 211 Å channel, the emission was weak. Therefore it was not included in our analysis as presented, but it was found to be modelled as successfully as the other channels. We note that the 12 s cadence of the AIA data means that the true peaks of the intensity data may not have been observed. An improved cadence could have resulted in a better or poorer agreement with the results of our forward modelling, but our aim was to be consistent with the available data.

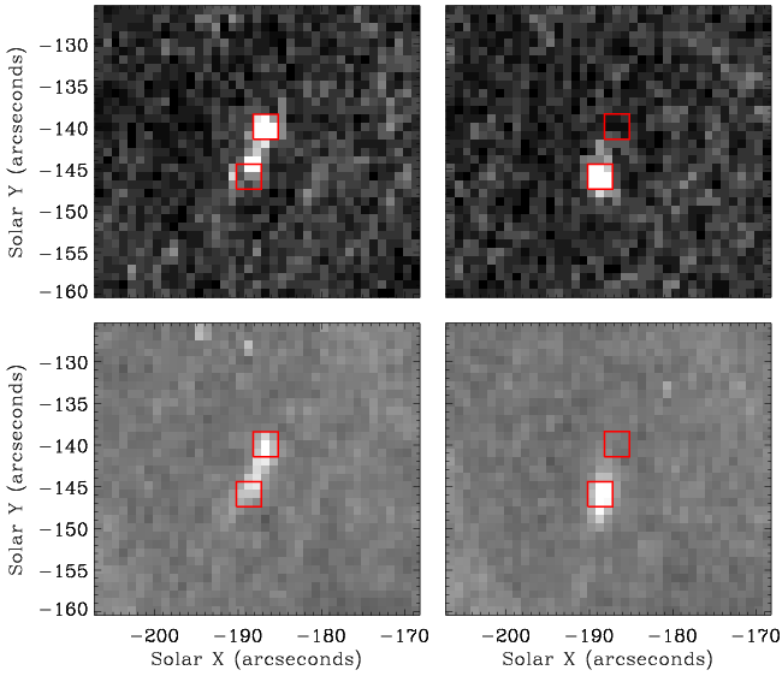

Figure 3.1: Excerpt of the observational AIA intensity data for the 131 Å channel in the top row and the 193 Å channel in the bottom row. The images from the first column are approximately from the same time, the second column shows images obtained 70 s later. The axes indicate solar coordinates in arcseconds, and the pixels are squares of side length 0.6″. The colour of the pixels indicates the intensity, with white being the most intense. The red boxes indicate the nine pixels that correspond to the explosive events at each footpoint that are summed to produce the observational intensity plots (Figure 3.2).

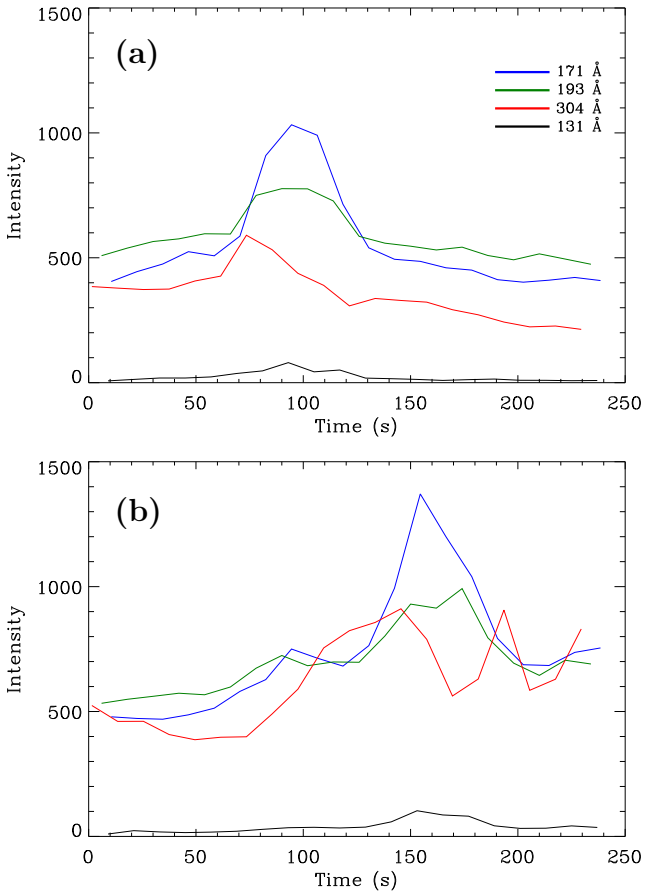

Figure 3.2: Observational AIA intensity data for the four spectral channels showing the first (a) and second footpoint (b).

3.3 Numerical Simulations

The evolution of the impulsively heated loop was simulated using the 1D hydrodynamics and radiation code HYDRAD. A heating pulse was injected into one of the footpoints at the top of the chromosphere, and its evolution was computed until the loop settled back into a static state. The temporal profile of the heating pulse consists of a linear increase to the peak volumetric heating rate, followed by a plateau, followed by a linear decrease to zero. In this work, the resolution was such that the smallest grid cell width was 0.12 km.

It is possible that ionisation may be close to equilibrium in our case, but simulating under non-equilibrium ionisation is still favourable. Our forward modelling relies heavily on the emission from the ions, so if they were to be erroneously distributed within the loop, the accuracy of the models would suffer.

For simplicity, the loop was assumed to have zero inclination such that it was perpendicular to the solar surface. The approximate coordinates in arcseconds of the observed loop footpoints are -193, -140 for the first (northern) and -191, -146 for the second (southern) footpoint. The ends of the loop were rooted in a chromosphere of temperature 2×10^4 K. The other parameters were varied through a process of trial and error in an effort to determine their value.

3.4 Forward Modelling

The physical data generated by the simulations were fed into the forward-modelling component of HYDRAD. We used the same response functions for equation (2.8) as Bradshaw and Klimchuk (2011); these functions are a product of the plate scale, effective area, and gain of the AIA instrument.

Intensity plots corresponding to Figure 3.2 were created from the numerical results by forward modelling. The emission might be optically thick in the 304 Å channel, therefore the modelled intensity may be inaccurate for this channel because the code does not include optically thick emission. However, the use of multiple other

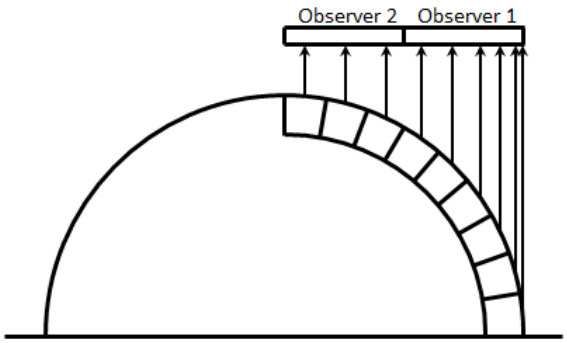

Figure 3.3: Two observers are shown, highlighting how the line-of-sight depth through the loop increases closer to the footpoints when using arbitrarily equally spaced portions. Not to scale.

channels minimises any effects of this. To create synthetic observations that could be compared to the observed intensities, the loop was projected onto a flat base and was regridded to the AIA pixel size to account for the geometry (Figure 3.3). Then the data points in a corresponding three-pixel length of loop were summed to create the synthetic intensity. The location of this loop section was varied to find the best observational match.

3.5 Results and Discussion

We went through a cyclic process of trial and error whereby the results of the forward modelling were compared to the observations to inform the choice of parameters for a new set of simulations in an attempt to approach the observed values. The final results yielded a footpoint density of 1.2×10^{10} cm^{-3}, which resulted in a loop peak temperature of 4×10^5 K before any heating. The temperature of the loop was derived from the footpoint density and not chosen independently. The uniform background heating rate was 1.68×10^{-4} erg cm^{-3} s^{-1}. The heating event of the loop had a maximum impulsive heating rate of 0.08 erg cm^{-3} s^{-1} and a scale length of 1×10^5 m. The heating pulse was applied to the top of the chromosphere at the first footpoint because the observations show the first footpoint to peak in intensity before the second footpoint.

It was found that as the total duration of the heating event increased, the inten-

sity peaks broadened, and secondary peaks to the right became more pronounced. A duration of 50 s was found to give the best match to the observations, which is comparable to the peak width at the first footpoint shown in Figure 3.2. This was split between the three parts of the pulse's temporal profile as 20 s for the linear increase, 10 s for the plateau, and 20 s for the linear decrease. The similarities between the observed pulse width and the simulated heating duration provides support for the proposed scenario.

The evolution of the impulsively heated loop can be seen in the hydrodynamic data in Figure 3.4. The initial state is clearly shown with almost symmetric density and temperature profiles before the heating event. The influx of energy approximately triples the temperature of the loop near to its first footpoint and significantly heats the nearby chromosphere, triggering an evaporation of material. The hot material flows into the loop, causing an increase in density and temperature as it travels to the other end. The flow rebounds and travels back along the loop, most clearly seen by the velocity, but with much less energy, having imparted much of it to the chromosphere at the second footpoint during the rebound.

After 240 simulations we found that a loop heated to a peak of 5.8×10^5 K from an initial temperature at the apex of 4×10^5 K (Figure 3.5) had emission lines that matched the ordering of the spectral filters observed (Figure 3.2). For example, the 304 Å filter peaks first, followed by the three others peaking shortly after each other, and the positioning of the peaks relative to each other is approximately consistent with the observations. The loop was taken to be 10.2 Mm long, including 1 Mm of chromosphere at each end, to match the observed 60-second delay between peak intensities, which was found to decrease with shorter lengths and increase with longer lengths. For example, a previous loop with a length of 9 Mm had a delay of 50 s between the peaks.

With the loop length and peak separation known, it is possible to derive the propagation speed of the heating pulse from the intensity plot. Using the distance in loop coordinates between parts of the summed loop sections at each footpoint, the outer

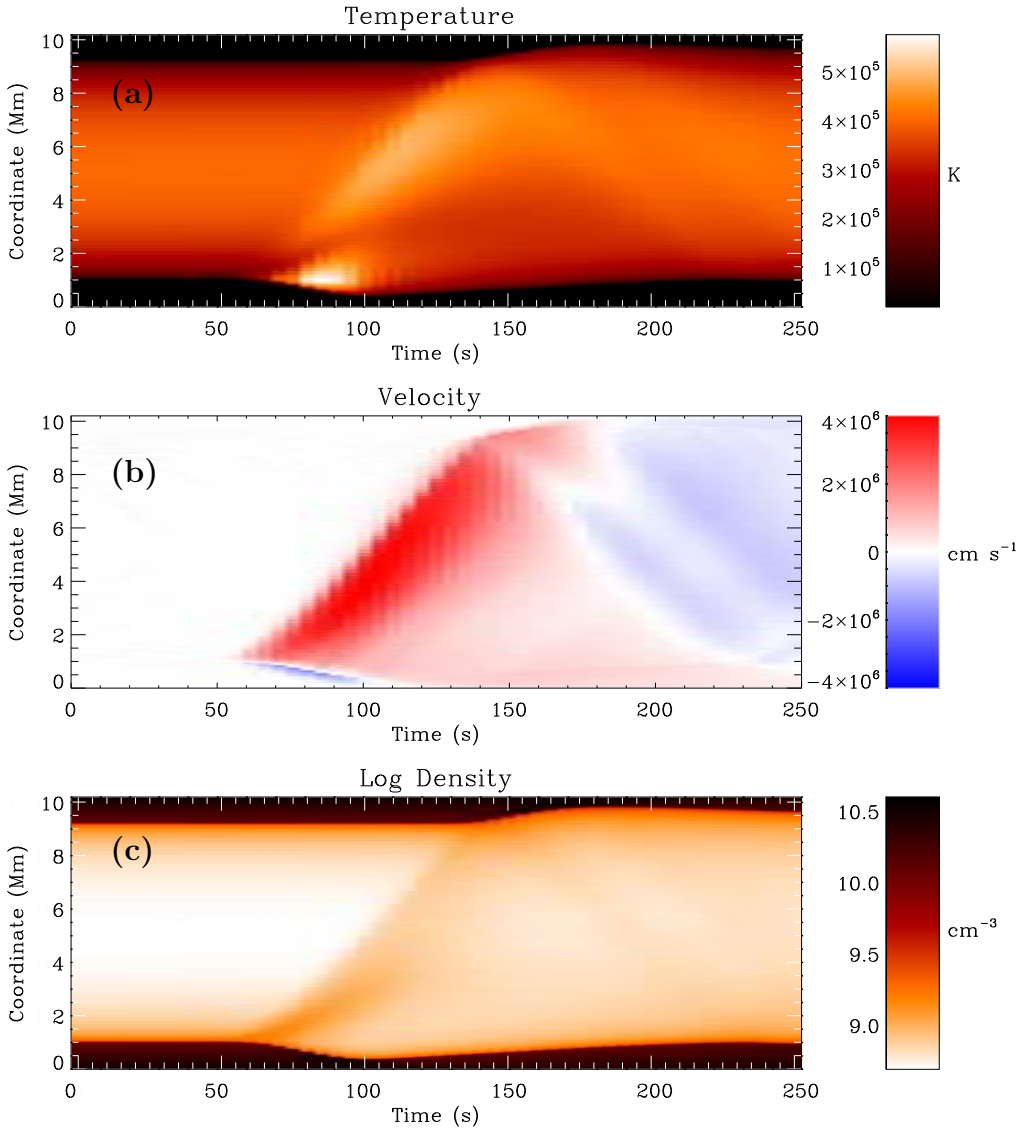

Figure 3.4: Simulated hydrodynamic parameters of the dynamically heated loop used in the final result. All plots are in a field of the loop coordinate (Mm) against time (s), with (a) showing temperature (K), (b) showing velocity (cm s^{-1}), with red indicating positive velocity in the increasing loop coordinate direction, and (c) showing base 10 logarithmic density (cm^{-3}).

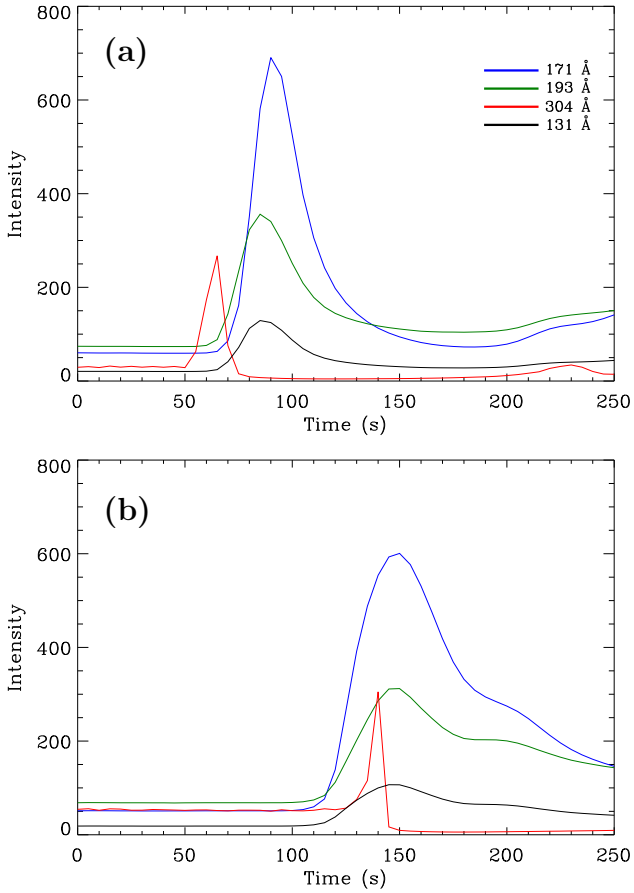

Figure 3.5: Forward-modelled intensity for the impulsively heated loop showing the first footpoint (a) and the second footpoint (b). The heating event lasted for 50 s and had a maximum heating rate of 0.08 erg cm^{-3} s^{-1}. It had a scale length of 1×10^5 m and was injected 1 Mm into the loop, at the top of the chromosphere.

edges, the centres, and the inner edges, a distance-over-time calculation is possible. We took the average of the three values, with the edges being the upper and lower error bounds. This yielded a propagation speed of 100 ± 37 km s^{-1}. By combining the known 60-second delay between the brightenings with simple geometry and the observed image (Figure 3.1), it is possible to obtain an approximate propagation speed of 102 ± 15 km s^{-1}. This is done by calculating the length of a semi-circle connecting the centre pixels of the red boxes, and the length of one connecting the two outermost pixels. These two lengths give us our upper and lower bounds, with the average yielding the stated value. The approximate observed propagation speed agrees well with the simulated value. We found that higher temperatures resulted in higher propagation speeds and that greater heating rates increased the maximum velocity in the loop.

Loops with a higher initial apex temperature, and therefore density, resulted in an intensity that was seen to drop during the pulse for some AIA channels. However, where the initial temperature was too low, the 304 Å line dominated the profiles for all of the heating pulses we studied. Higher temperatures in general yielded intensities that were orders of magnitude greater than those observed and had more jagged lines. Where the initial temperature was low enough to allow for pulses to cause increases in intensity, the pulses with higher heating rates tended to favour the 171 Å filter. It deviated significantly from the other three filters and made a second peak more pronounced. For comparison we include Figure 3.7, where the parameters are identical to those of Figure 3.5, except for a ten times increase in footpoint density that yields an initial apex temperature of 8.7×10^5 K. The higher temperature results in initial intensities almost two orders of magnitude above the observed values.

The intensity of the first footpoint tended to be increasingly favoured over the second in the case of high pulse scale lengths, in contrast to the observations where the second footpoint has greater intensity. This effect at the first footpoint is because higher scale lengths lead to a greater column depth of material being at a

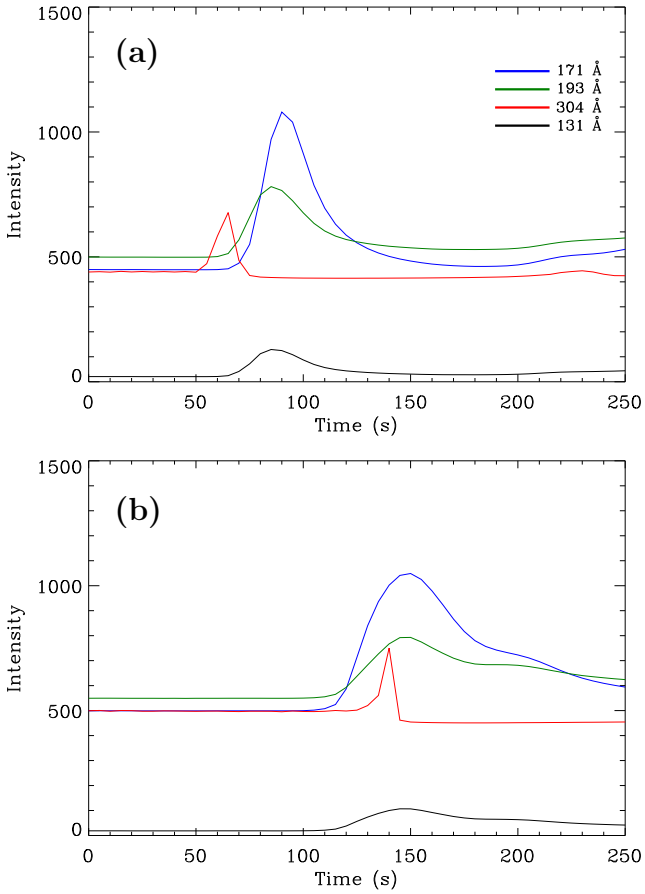

Figure 3.6: Forward-modelled intensity for the dynamically heated loop (Figure 3.5) plus background addition, showing the first footpoint (a) and the second footpoint (b). The heating event lasted for 50 s and had a maximum heating rate of 0.08 erg cm^{-3} s^{-1}. It had a scale length of 1×10^5 m and was injected 1 Mm into the loop, at the top of the chromosphere.

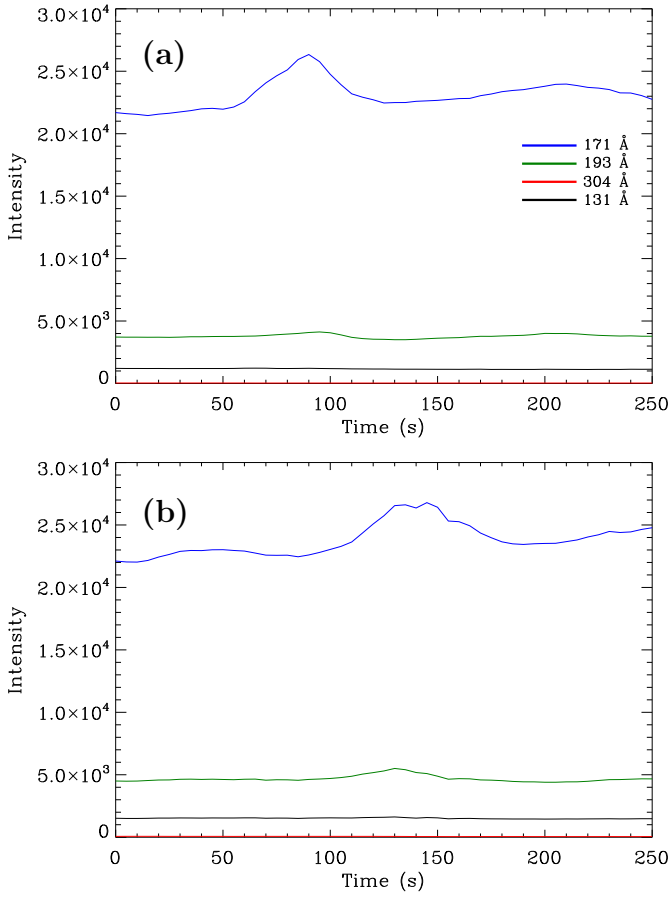

Figure 3.7: Forward-modelled intensity for an impulsively heated loop showing the first footpoint (a) and the second footpoint (b). The parameters are identical to those of the final impulsively heated loop (Figure 3.5) except for a ten times increase in footpoint density. The heating event lasted for 50 s and had a maximum heating rate of 0.08 erg cm^{-3} s^{-1}. It had a scale length of 1 $\times$ 10^5 m and was injected 1 Mm into the loop, at the top of the chromosphere.

higher temperature, so the intensity increases commensurately. The scale length was subsequently set at 1×10^5 m which yielded footpoints with more comparable intensities.

The success in reproducing the appearance of the line profiles with this pulse leads us to believe there were other contributions from the Sun, which were not taken into account by our model. These probably caused the second footpoint to have greater intensity in the observations. This position is supported by the fluctuations seen in the observations before the pulse begins. They suggest another source, independent from the heating event, of temperature variance or intensity. Another possibility is that the loop may not be symmetrical about the apex, which could lead to different density stratifications for the two ends, which in turn may lead to a higher intensity for the second footpoint.

Originally, the loops had peak intensities several times greater than the observed values. An effort was made to reduce these because the overall shape of the line profiles agreed well. By reducing the width of the loops in the forward model to 2 Mm, the intensities across the loops were reduced by a proportional amount to be more reasonable (Figure 3.5). However, this also reduced the initial intensities before the pulse, which were below target to begin with. To mitigate this, we attributed the initial intensity from the observations to unresolved background emission and added an appropriate number to all points in each channel to make the first points comparable to their observed counterparts. This reduced the peaks and improved the initial intensities (Figure 3.6).

The equation (2.7) governing the heating pulse was integrated in time and space along the loop to determine the total amount of energy deposited by the event. The integral took the form of

$$E_p = E_0 \int_0^L e^{-\frac{(s-s_0)^2}{2(s_H)^2}} ds \left\{ \int_{t_0}^{t_1} \frac{(t-t_0)}{(t_1-t_0)} dt + \int_{t_1}^{t_2} dt + \int_{t_2}^{t_3} \left[1 - \frac{(t-t_2)}{(t_3-t_2)} \right] dt \right\} \quad (3.1)$$

where E_p denotes the total heating energy per unit area due to the pulse, E_0 the

impulsive heating rate, L the length of the loop, s the position along the loop, s_0 the heating location, s_H the heating scale length, t the time, t_0 the time the heating rise phase begins, t_1 the time the heating rise phase ends, t_2 the time the heating decay phase begins, and t_3 the time the heating decay phase ends. This was solved by using a standard definite integral

$$\int_0^u e^{-x^2} dx = \frac{\sqrt{\pi}}{2} erf(u) \tag{3.2}$$

where erf is the error function. The calculation, using our circular cross-sectional area of 3.14×10^{16} cm^2, yielded a total heating energy of 1.89×10^{24} erg, which is consistent with the energy of a nanoflare (Parker, 1988).

In an effort to improve on this result, we tried to recreate the observations with an injection of cold plasma instead of with a heating pulse. For this the forcing term from the momentum equation (2.2) that had not existed up until this point took the following form:

$$F = A\rho \sin\left(\frac{t - t_o}{t_d}\pi\right) \cos\left(\frac{s - s_0}{2s_H}\pi\right) \tag{3.3}$$

where A is the acceleration of the plasma, t_0 the injection start time, t_d the duration, s_0 the location, and s_H is the scale length. The best results were achieved where the physical parameters were the same as used for the most accurate impulsively heated loop.

The physical evolution of the loop is shown in Figure 3.8, with an initial state identical to that of Figure 3.4. The cold plasma is shown by the temperature plot to extend the black chromosphere up into the loop. The density plot for the same region indicates a peak of high density moving with the footpoint until the plasma injection ceases and it falls back as a result of gravity. While the bulk of the material was contained in this peak, there was also a much smaller pulse of density that traversed the loop similarly to the impulsive heating case. This caused the same effects as seen previously, with all three plots indicating a flow of material from the first footpoint

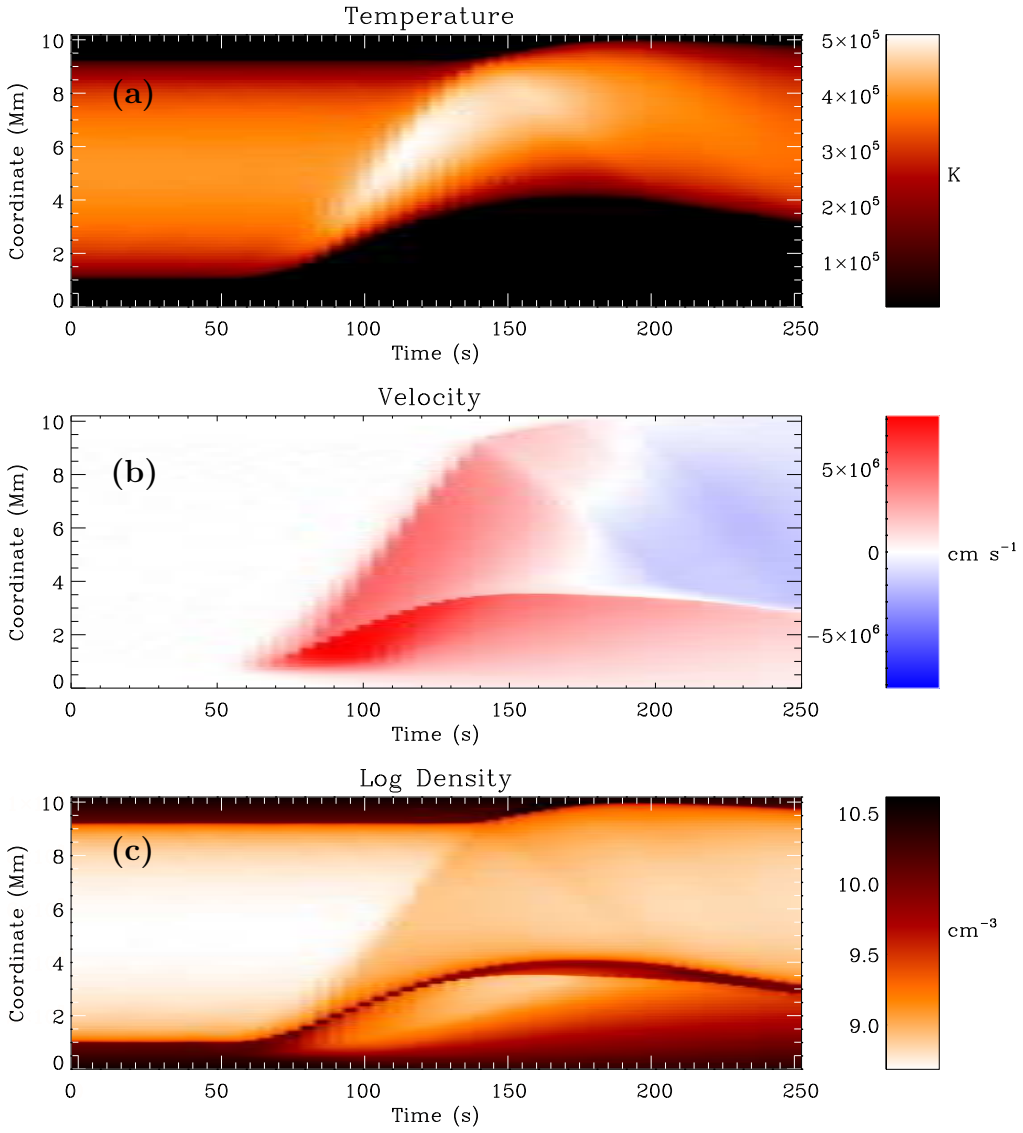

Figure 3.8: Simulated hydrodynamic parameters for the best loop from the cold plasma injection efforts. All plots are in a field of the loop coordinate (Mm) against time (s), with (a) showing temperature (K), (b) showing velocity (cm s^{-1}) with red indicating positive velocity in the increasing loop coordinate direction, and (c) showing base 10 logarithmic density (cm^{-3}).

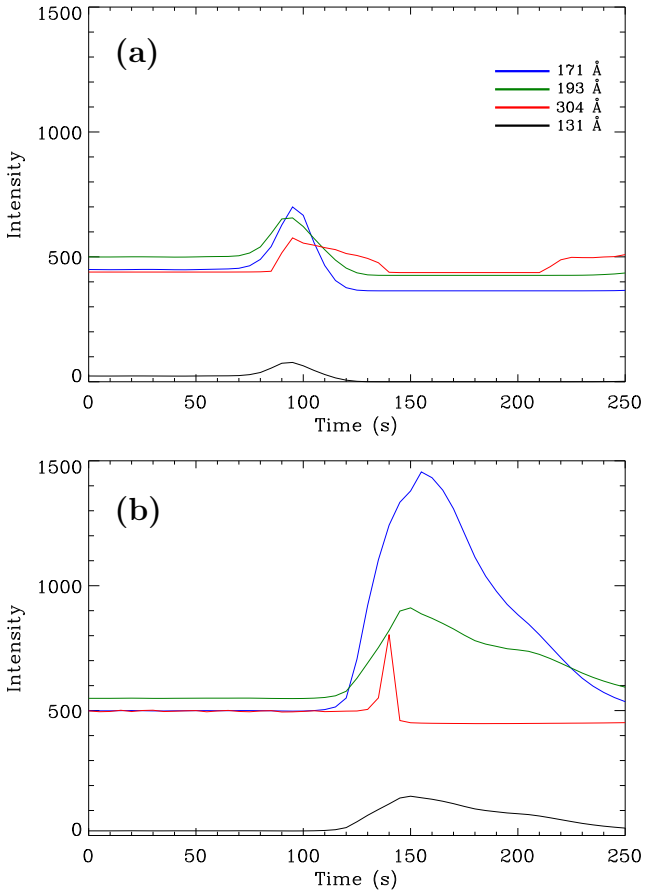

Figure 3.9: Forward-modelled intensity for the loop subjected to cold plasma injection plus background addition, showing the first footpoint (a) and the second footpoint (b). The plasma injection lasted for 60 s and had an acceleration of 6×10^5 cm s^{-2}. It had a scale length of 5×10^5 m and was injected 1 Mm into the loop, at the top of the chromosphere.

to the second footpoint and then back again. The second footpoint is fairly similar to the one shown in Figure 3.4. In this instance, the pulse duration was 60 s, the scale length was 5×10^5 m, and the acceleration was 6×10^5 cm s^{-2}.

The propagation speed was determined in the same manner as before from the intensity plot, yielding a value of 87 ± 33 km s^{-1}. While the error bounds overlap with those of the observed speed, it is less comparable than the value derived from the impulsive heating simulations.

The loop reached a peak temperature of 5.1×10^5 K and was found after 14 simulations to yield the most accurate intensity plot of the cold plasma injection simulations. It had the same initial problems as the impulsively heated loop, however, and was found to be improved by the addition of background values in the same manner (Figure 3.9).

3.6 Summary and Conclusions

We used hydrodynamic simulations and forward modelling to recreate the intensity profile of a loop event observed by AIA. The initial conditions assumed the fifteen most abundant solar elements to be in equilibrium, and the loop was kept stable by time-independent uniform heating. During the simulations the elements were considered as not in equilibrium, and a single heating pulse was injected at the first footpoint, later replaced with an injection of cold plasma. The output was fed into forward models to create synthetic intensity profiles that were compared to the observed ones.

The results depicted in Figure 3.6 approximately agree, but the shape and ordering of the profiles are notably affected by relatively small changes in the parameters. The addition of the background was necessary to create plots that better matched the observations. However, the observed intensity before and after the events fluctuated whereas we added a constant value to each channel, so the comparison is not perfect.

In Figure 3.9, which shows the cold plasma injection, the intensity of the second

footpoint is a much better match to the observations. However, the first footpoint is noticeably worse because the cold plasma moved the temperature gradient further along the loop, so we had to move the summed loop section along as well. This caused the channels to no longer peak in the correct time order, and they had lower intensities than seen for impulsive heating.

By comparing the propagation speeds of the two methods derived from their intensity plots, we find that the value of 100 ± 37 km s^{-1} from the impulsive heating simulations better matches the approximate observed value of 102 ± 15 km s^{-1} than the value of 87 ± 33 km s^{-1} from the cold plasma injection simulations. We conclude that the observations are better modelled by a heating pulse, similar to the findings of Reale et al. (2000), instead of an injection of cold plasma.

The resemblance between our simulated loop and the observed brightenings appears to confirm the initial suggestions by Innes and Teriaca (2013), who reported that they were studying a loop. The rebounding flow seen in Figure 3.4 could lend support to their theory that the second brightening is a downward and reverse jet. However, modelling the accompanying expanding ring of increased emission around the second footpoint that they observed was beyond the scope of our model here. It might be partially responsible for the greater peak intensity of the second footpoint seen in the observations.

Chapter 4

Physics of Outflows Near Solar Active Regions

Hinode/EIS observations have revealed outflows near active regions which remain unexplained. An outflow region observed by EIS that appears slightly redshifted at low temperatures and blueshifted at higher temperatures is presented. We conduct simulations with different spatial and temporal distributions of heating. We use the simulated output to create synthetic line profiles in order to replicate the observed line profiles of an apparent open structure. The results of the forward modelling support a scenario whereby long loops consisting of multiple strands undergo a cyclical process of pulse footpoint heating and cooling on timescales of approximately 80 minutes.

4.1 Introduction

The EIS instrument (Section 2.3.1) has given us spectacular spectral images of various phenomena since its launch. Of particular interest are outflow regions that may help to explain some of the Sun's remaining mysteries. Such outflow regions are usually located at the periphery of many solar active regions. Large amounts of material leaving the Sun is always of interest in terms of the coronal heating problem, and in terms of the origins of the solar wind.

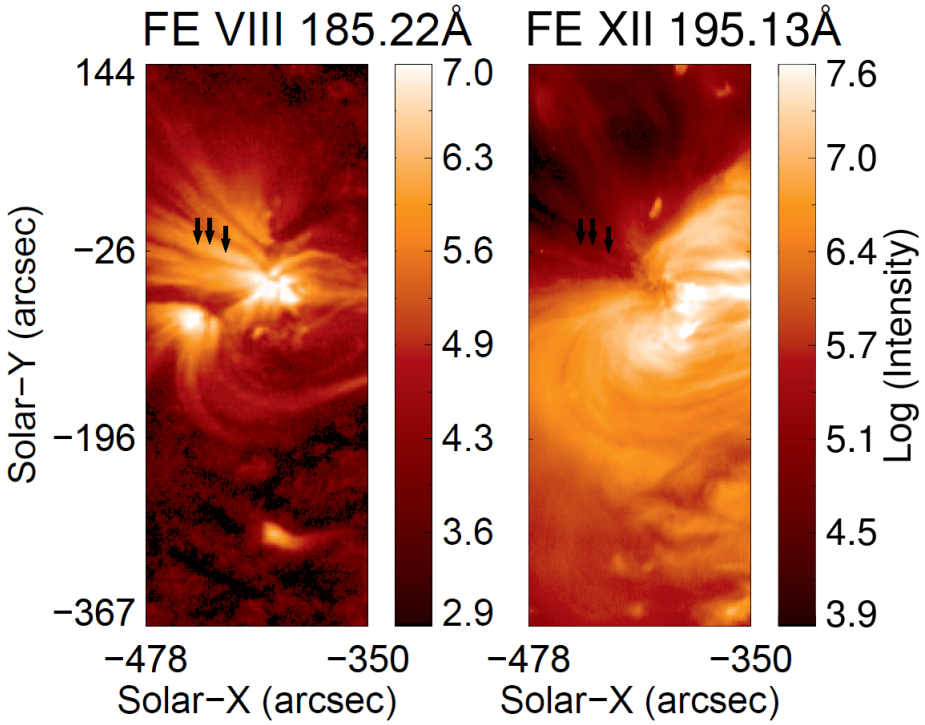

Figure 4.1: Intensity of the Fe VIII, and Fe XII emission lines for the observed area; the outflow region is visible flowing towards the upper left part of the images. The black arrows indicate the approximate locations of the pixels used for the line profiles of Figure 4.2. In order from left to right they correspond to the dashed line, the dotted line, and the solid line respectively (as drawn in Figure 4.2).

It has been established that transition region emission lines display net Doppler shifts or slight redshifts (Doyle et al., 2002), which are often observed together with blueshifted higher-temperature lines. This has been reported in a number of situations: for example, Warren et al. (2011) found redshifted cold loops adjacent to a high-temperature blueshifted outflow region.

In the following work we investigate a particular outflow region that has been noted in several other papers (e.g. McIntosh and De Pontieu, 2009; Warren et al., 2011). We approximate what appears to be an open structure as a long loop and perform hydrodynamic simulations to replicate the observed emission line profiles, allowing us to suggest physical parameters such as temperature and density. We create synthetic line profiles and compare them to the observed profiles to determine the accuracy of our simulations and to establish the physical nature of the outflows.

4.2 Observations

For this study, we concentrated on an active region visible on 20 February 2007. Hinode/EIS observations of the active region were carried out using the 1″ wide slit in raster mode. In the following analysis, we select the Fe VIII 185.21 Å, Fe X 184.54 Å, and Fe XII 195.12 Å spectral lines with formation temperatures of $\log T \approx 5.6$, 6.0, and 6.2.

EIS level 0 data files are processed with the eis_prep software, using the default options. The eis_wave_corr procedure and the level 1 data are used to calculate the wavelength corrections for each spectral line. We fit a single Gaussian profile to each line spectrum, using the eis_auto_fit software. The reference wavelength of each line profile has been updated to match the rest wavelength found in a laboratory, and is taken from Warren et al. (2011). EIS Doppler velocities need calibrating against a reference wavelength, where the quiet Sun velocity averages to zero. For this work the Fe VIII 185.21 Å line is chosen as a reference. The other lines are calculated relative to the final wavelength of this line.

The intensity maps in Figure 4.1 show fan-like structures at the top left corners of the images that become bright mainly in the low-temperature line of Fe VIII 185.21 Å. The connectivity of the fan-like structures is unclear in the small field of view of EIS. These are either long loops or open structures that extend into the solar wind.

We selected three pixels from the outflow region as shown in Figure 4.1 and plotted their line profiles, interpolating between the available data points to complete the curves (Figure 4.2). Although the three sets of line profiles are not identical, they have similar intensity despite being taken from different spatial locations. This was also true for other pixels in the region which are not shown. The Doppler shifts for the pixels show slight redshifts for Fe VIII, barring the dotted centre one, which is slightly blue, and blueshifts for Fe X and Fe XII.

With Warren et al. (2011) suggesting that the region is a combination of outflows and fan loops, we produced a series of scatter plots of intensity (Figure 4.3). If the region contained only fan loops a linear correlation would be expected, as seen in

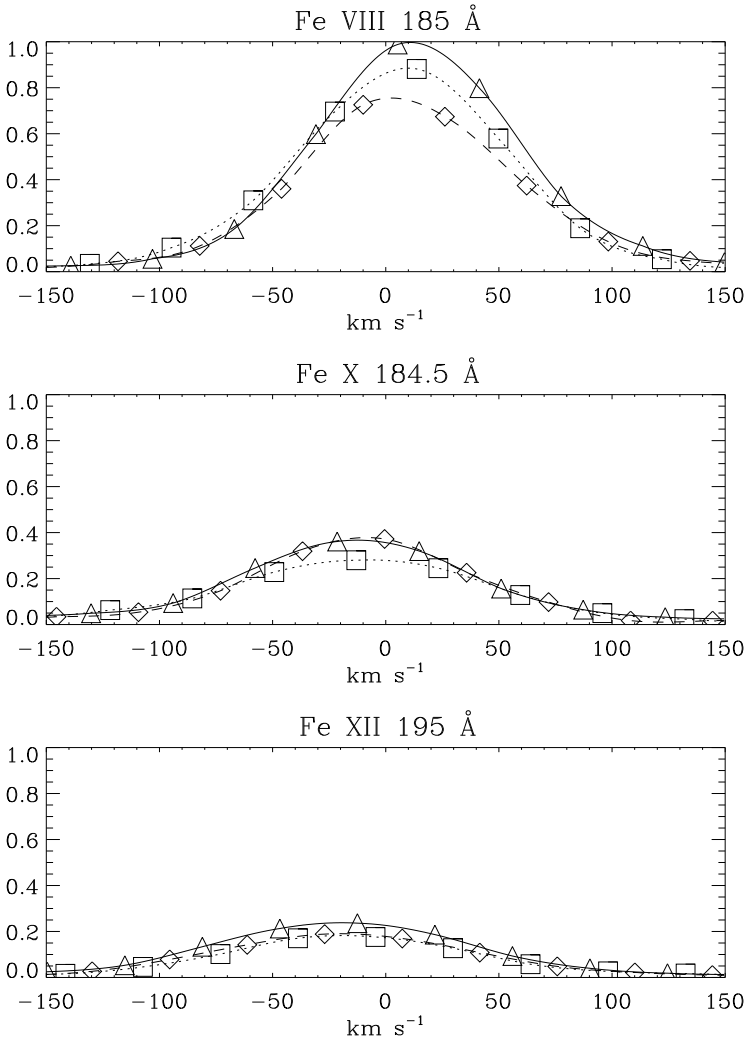

Figure 4.2: Observed line profiles for three pixels chosen from the outflow region seen in Figure 4.1. The different line styles distinguish the different pixels and the symbols indicate the corresponding observed data points; the gaps are filled via interpolation. The top profile is for the 185 Å Fe VIII (4×10^5 K) emission line, the middle profile is for the 184 Å Fe X (1×10^6 K) line, and the bottom profile is for the 195 Å Fe XII (1.3×10^6 K) line. This ordering of lines is consistent throughout the chapter.

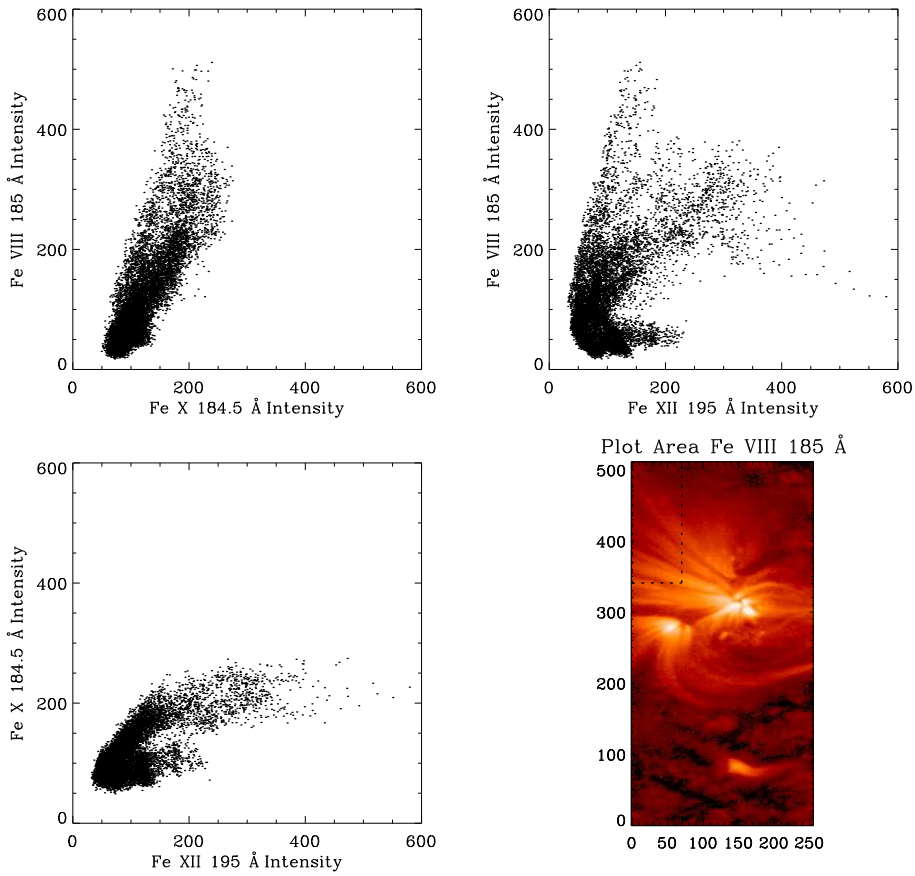

Figure 4.3: Going from left to right, intensity scatter plots of Fe VIII versus Fe X, Fe VIII versus Fe XII, and Fe X versus Fe XII. With an intensity map in Fe VIII whose black dashed box indicates the points used.

the first plot. However the third plot shows two distinct groups, interpreted as being a result of the postulated fan loops and outflows.

4.3 Modelling

We approximated the observed structure as a long loop and modelled it using the 1D hydrodynamics and radiation code HYDRAD (Section 2.5). The simulations were carried out taking into account the 15 most abundant elements in the solar atmosphere; to begin with they were considered to be in equilibrium for calculating the initial state and then not in equilibrium for the ensuing simulations. This ability of the code combined with its adaptive grid allows us to get an accurate picture of how all of the ions are affected throughout the simulations.

The loop was taken to be 100 Mm long, from a visual estimate, including 2 Mm of chromosphere at each end. These footpoints of the loop were held at a constant temperature of 2×10^4 K, and their density varied to find the best value. The initial apex temperature of the loop was determined by the code from the footpoint density, so it varied accordingly. The initial state of the loop is found by uniform time-independent background heating that persists throughout the simulation to prevent it from cooling to collapse.

With this loop we then attempted to recreate the observed line profiles by injecting a single time-dependent heating pulse into the top of the chromosphere at the first footpoint. The parameters of the pulse were varied over a number of simulations, but its temporal evolution always took the form of a linear increase from zero to maximum heating, a plateau, and then a linear decrease back to zero.

The simulations began immediately with the injection of the pulse and continued until the loop had settled back almost to its initial state. The physical and ion data were then forward-modelled using a separate part of the code in order to synthesize the line profiles of interest in the same way as described by Taroyan et al. (2006).

The profiles correspond to the emission of the loop from 18.7 to 20.0 Mm, which corresponds to the 1″ slit of EIS when transformed out of the semi-circular loop coordinate frame. We construct the profiles for a single loop, 10 superimposed threads, and 100 superimposed threads. In the latter two cases there is a random time lag between each two, otherwise identical, neighbouring threads as in the modelling of Taroyan and Bradshaw (2014). The line profiles, superimposed or not, are then fitted with a single Gaussian to determine their Doppler shifts for comparison to the observed values.

4.4 Results and Discussion

It was found that the observations were reproduced most accurately by a loop with an initial density of 7×10^9 cm^{-3} which had a corresponding apex temperature of approximately 7×10^5 K. The pulse consisted of a volumetric heating rate of

6×10^{-3} erg cm^{-3} s^{-1}, a scale height of 2 Mm, and a total duration of 500 s. This was broken into 200 s for the linear increase, 100 s for the plateau, and 200 s for the linear decrease. The loop reached a maximum temperature of 1.1×10^6 K as it was heated. It was found that heating to the same peak temperature but with a lower heating rate over a longer period of time resulted in lower blueshifts.

The physical properties of the simulated loop are shown in Figure 4.4. The effects of the heating injection are reflected by all three plots, including multiple rebounds at the footpoints as the loop undergoes a single cycle of heating and cooling to initial low temperatures. We may be able to obtain a better fit in future with a dedicated open-structure model.

First, we inspect the single-thread case (Figure 4.5): we find bad agreement with the observations; none of the three profiles are persistently Doppler shifted one way or the other; and where they are shifted, the values exceed those observed. Also, the profile peaks are not consistent with the observations. The superposition of 10 threads across the line of sight as shown in Figure 4.6 is a clear improvement, with some periods of time being fairly comparable to the observations; however there is still no consistency in shifts amongst the emission lines. The 100-thread case (Figure 4.7) yields further improvements, with the emission lines being fairly consistent with each other over time, and their peak heights are comparable to those observed. Each thread evolves identically, i.e. a heating pulse is followed by cooling. The corresponding line profile is constructed for the superposition of the threads along the line of sight. The heating pulse along each thread is randomly offset within the 80 minute time interval.

The Gaussian fitting in the 100-thread case, taken forward as the most accurate representation of the observations, revealed Doppler shifts of approximately 0, -10, and -25 km s^{-1} for the Fe VIII, the Fe X, and the Fe XII emission lines respectively. These values are fairly consistent with the observations considering the $\pm$ 5 km s^{-1} instrument error (Culhane et al., 2007).

Following this we investigated other methods of heating the loops to see if the ob-

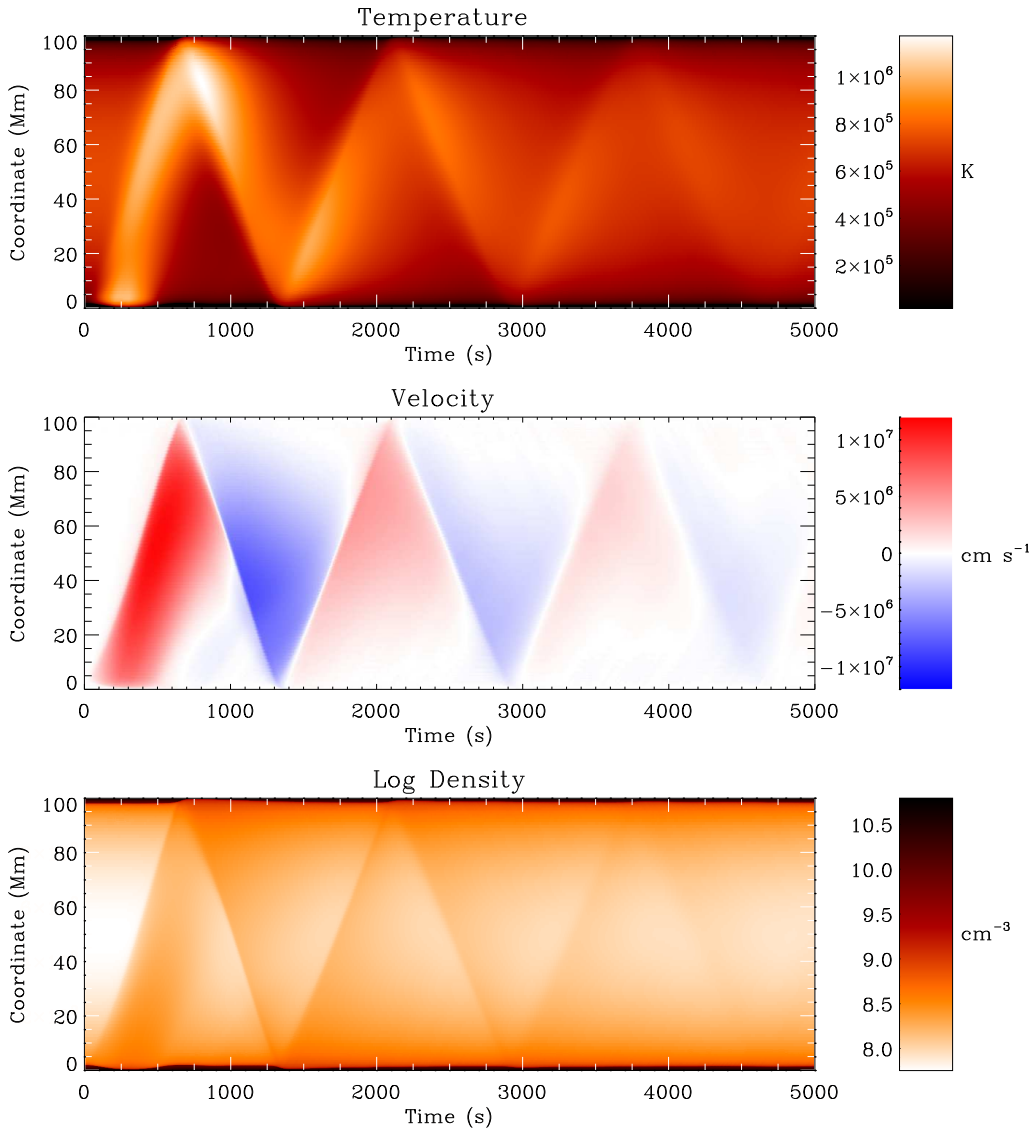

Figure 4.4: Physical properties of the simulated monolithic loop structure using single pulse footpoint heating. The plots show the evolution of the temperature (K, top), velocity (cm s^{-1}, middle), and base 10 logarithmic density (cm^{-3}, bottom) in time and loop coordinate.

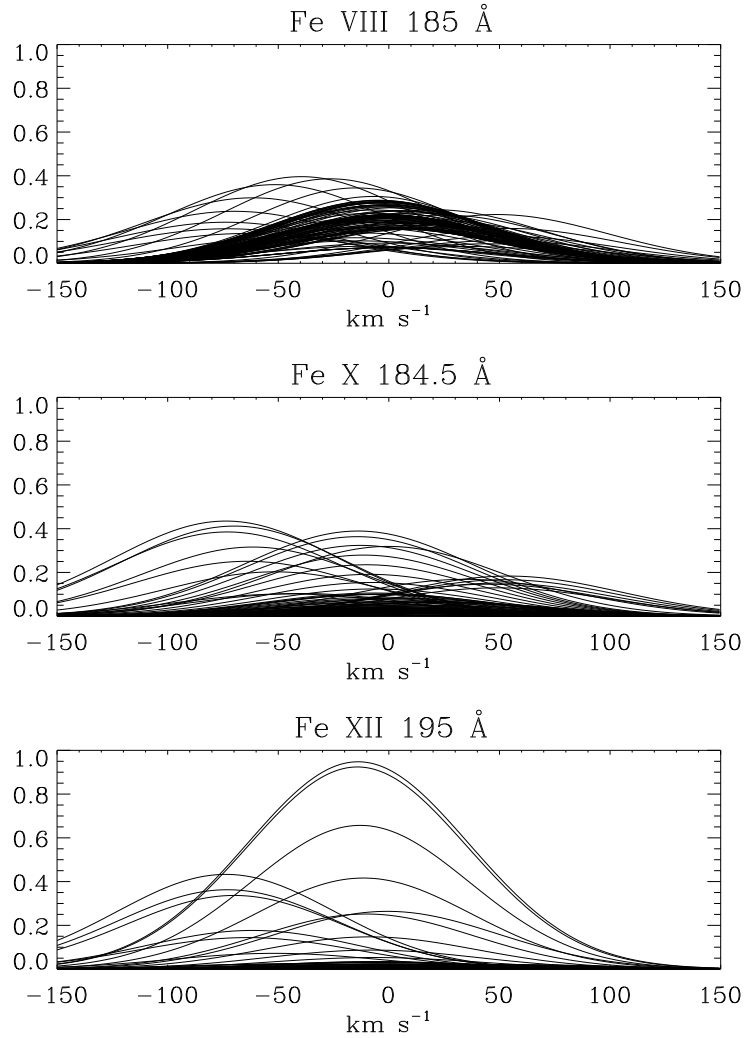

Figure 4.5: Synthetic line profiles, from a 5000 s simulation using single pulse footpoint heating, for a loop consisting of 1 strand. There is a 50 s interval between each plotted line.

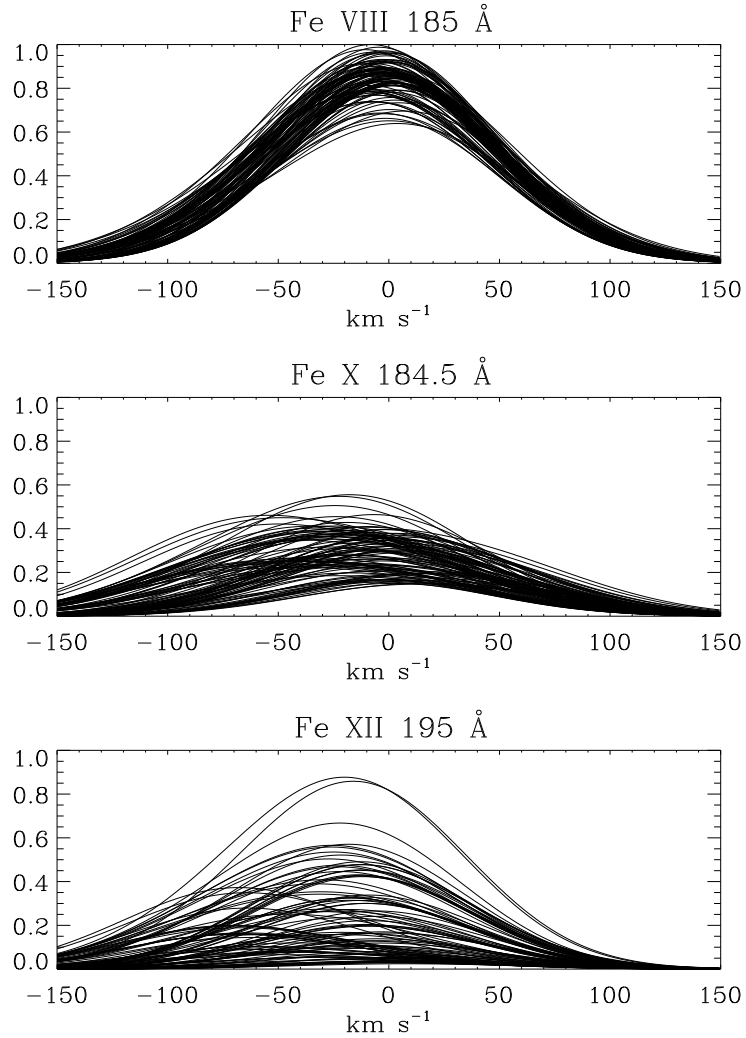

Figure 4.6: Synthetic line profiles, from a 5000 s simulation using single pulse footpoint heating, for a loop consisting of 10 strands. There is a 50 s interval between each plotted line.

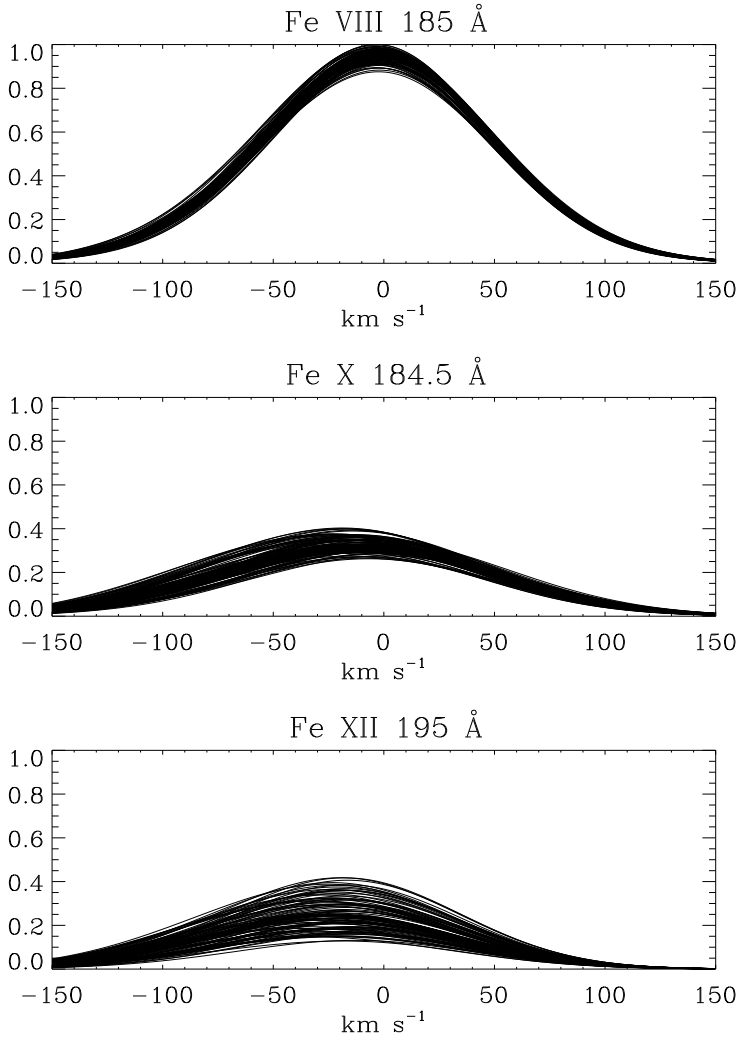

Figure 4.7: Synthetic line profiles, from a 5000 s simulation using single pulse footpoint heating, for a loop consisting of 100 strands. There is a 50 s interval between each plotted line.

served redshift of Fe VIII could be reproduced. Initially we disabled the background time-independent heating to emphasize the cooling behaviour and generated random pulses to replace the single pulse. The random properties of the heating events were determined using the code of Taroyan et al. (2011). However we removed the bounds on the volumetric heating rate and changed the volumetric heating rate calculations to factor in the energy equation (2.7) used in HYDRAD with a temporal profile of a linear increase from zero heating to maximum heating for two-fifths of the event duration, a plateau for one-fifth, and a linear decrease back to zero for the remaining two-fifths. Within a series of bounds on certain parameters, namely the total heating energy, the heating duration, the event energy, the spatial location, and the simulation time, the events were randomly generated according to a power-law index. This random generation encompassed the energy of the event, the onset time of the heating, the duration of the heating, and the number of events.

We note that the initial settings are not sufficient to distinguish different sets of heating events as the random nature can yield different results with each generation. Therefore the corresponding runs were characterized with plots of event energy, duration, and location against event number (Figure 4.8).

After early trials we increased the total simulation time with the intent of providing enough time for the loop to cool to its initial state as required for cyclic heating and the expected redshift generation. We also found that some heating events were generated such that they finished beyond the simulation time, meaning that their expected energy contribution was being partially lost. Therefore we imposed an upper limit on the heating duration to minimize the phenomenon.

Eventually it was found that the best results were generated where the random distribution had one large event close to the footpoint of the loop, and lots of small other events. This is very similar to the heating setup used in the single pulse case which had a single heating pulse heating at the footpoint of the loops. To illustrate this we include two figures with different heating events but randomly generated from the same initial variables, such as the same upper bounds on total energy. Initially

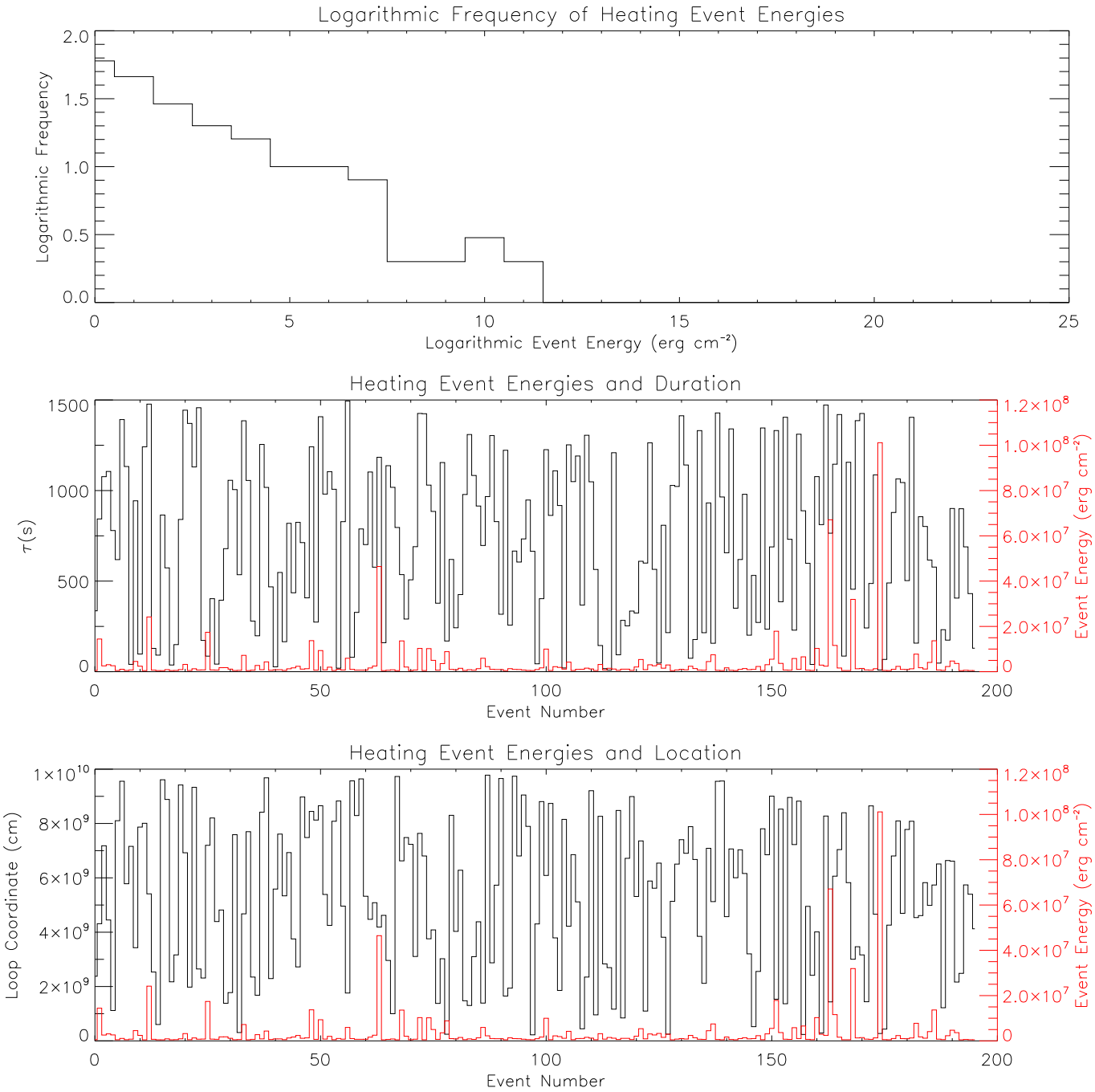

Figure 4.8: A set of plots characterizing an example random heating run. They show the base 10 logarithmic frequency of the heating event energies (top), the heating event energies and duration versus event number (middle), and the heating event energies and location versus event number (bottom).

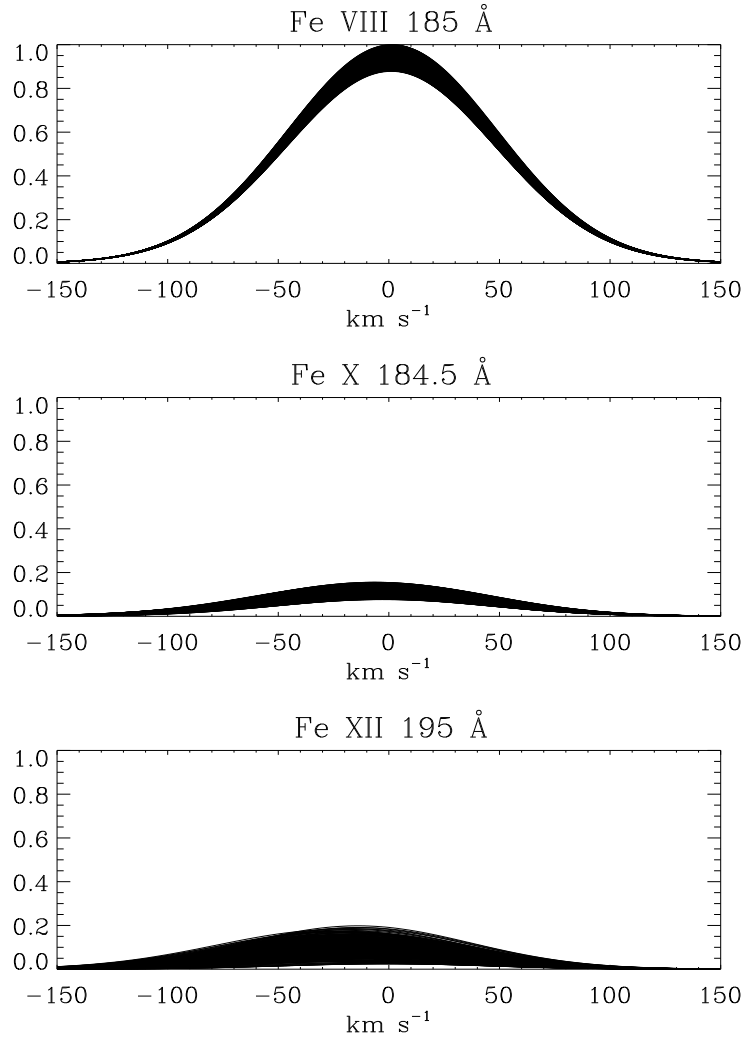

Figure 4.9: Synthetic line profiles, from a 20000 s simulation using random heating, for a loop consisting of 100 strands. There is a 50 s interval between each plotted line.

looking at Figure 4.9 where the heating events are randomly distributed between the footpoints we find bad agreement with the observations for the intensity of Fe X and Fe XII, though the Doppler shifts of 1.2, -6.7, and -16.5 km s^{-1} are promising. In contrast Figure 4.10 has the heating pulse with the most energy near the footpoint, resulting in a raised Fe X more in line with the observations, while the other two lines are very similar. The corresponding Doppler shifts were 1, -9.5, and -15 km s^{-1} for Fe VIII, Fe X, and Fe XII respectively which too are similar. We note that each Figure was generated from different sections of the loop, the amount still corresponds to the instrument as above in the single pulse footpoint heating case but the section providing the best agreement was used in each case.

While the majority of the random heating runs did yield minor redshifts for Fe VIII the other parameters were not as good as in the single pulse case. Consequently with the unreliability of the randomness, and the trend towards a large event being the most important, the simulations were reverted to a single defined pulse model. However we began applying the heating pulse at the apex of the loop rather than at the footpoint.

Starting with a loop that had an apex temperature of approximately 1×10^5 K simulations were ran in an attempt to heat it to 1×10^6 K, briefly enough to give the two high temperature lines enough intensity without them dominating the result, and then cool back down to its initial temperature. However the loop did not respond favourably to such a temperature change, in that it required a relatively large pulse of energy to heat it to 1×10^6 K and such pulses resulted in the apex being proportionally heated more than the rest of the loop during most of the heating rise phase (Figure 4.11). Therefore the initial temperature was doubled to an approximate apex temperature of 2×10^5 K. This initial condition proved to respond better to the heating and was used for the rest of the apex heating simulations.

With the initial conditions set, forward modelling was undertaken on the following simulations. A non-zero, albeit small, redshift was noted after the first run.

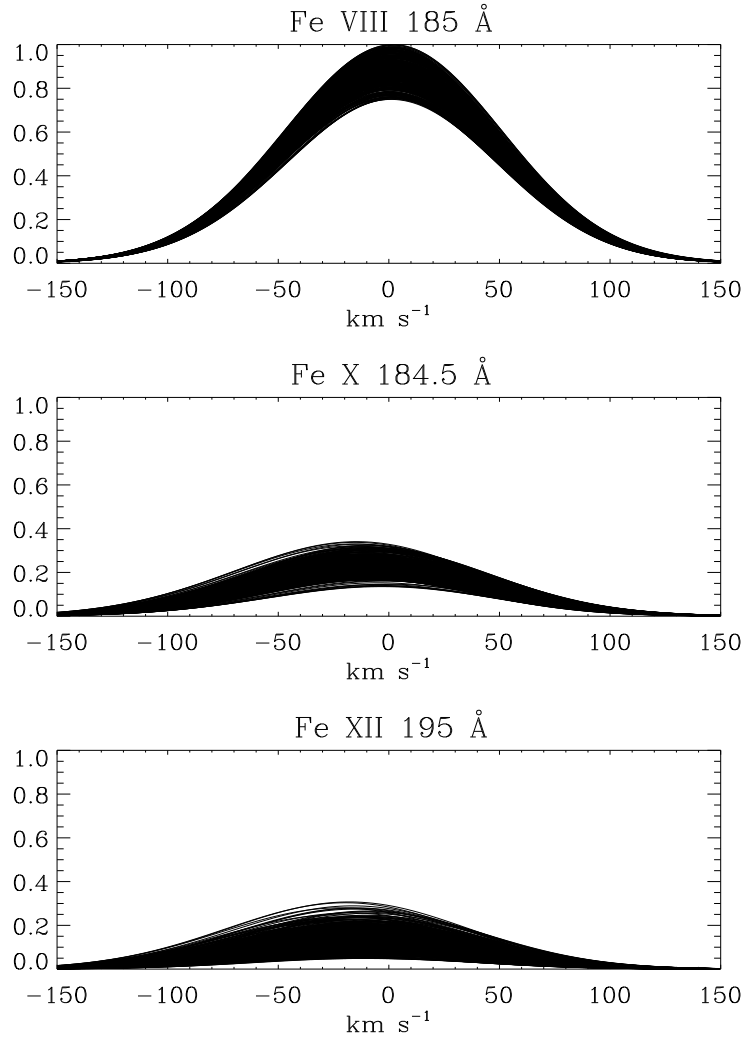

Figure 4.10: Synthetic line profiles, from a 20000 s simulation using random heating where the largest pulse is near the footpoint, for a loop consisting of 100 strands. There is a 50 s interval between each plotted line.

A process of trial and error with the pulse parameters ensued in an attempt to reproduce the observed Doppler shift and intensity. This resulted in intensity profiles similar to those from the single pulse footpoint heating, but with a lower Fe X relative intensity, a lower Fe XII relative intensity and blueshift, and an improved Fe VIII redshift. The best example from apex heating (Figure 4.12) is approximately 2.5, -10.2, and -3 km s^{-1} for the Fe VIII, the Fe X, and the Fe XII emission lines respectively.

Finally a fourth method of heating was used for comparison to the previous three. Using the same initial conditions, single pulse uniform heating was applied across the entire loop. This relatively short study, consisting of heating and then cooling back to the initial apex temperature, tended to produce results similar to the apex heating case but it yielded the biggest redshifts most consistently. However they tended to be around 2.5 km s^{-1} which was still relatively small. The similarity can be seen in Figure 4.13 particularly for the Fe VIII and Fe X intensities, while the Fe XII intensity is higher. The Doppler shifts displayed are 2.8, -9.8, and -1.9 km s^{-1} for Fe VIII, Fe X, and Fe XII respectively. That particular example is notable as a run where the heating rise phase was shorter than the heating decay phase with the aim of extending the cooling period where the redshifts were expected. However it was not pursued further due to the other parameters not matching, further study would be required to determine if a lengthened decay phase yields consistently higher redshifts.

4.5 Summary and Conclusions

We find that the observed structure can be approximated well by an impulsively heated multi-thread loop 100 Mm long, whereby the heating is applied as a single pulse to each loop at its footpoint. We determine the footpoint density to be 7×10^9 cm^{-3}. The superposition of multiple threads, each individually heated by a single pulse, results in the higher-temperature Fe X and Fe XII lines being persistently blueshifted throughout the simulation time, whereas the shifts corresponding

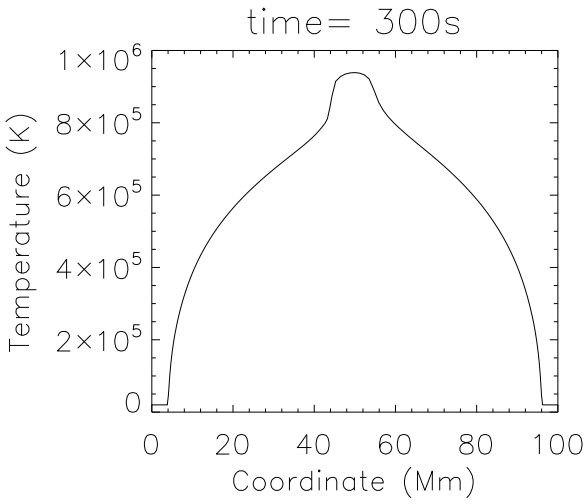

Figure 4.11: A plot of temperature (K) against loop coordinate (Mm) of a loop 300 s into a single pulse apex heating simulation where the apex was initially at approximately 1×10^5 K.

to the cooler Fe VIII line tend towards zero for an increasing number of threads. The good agreement between the observed and simulated line profiles allows us to interpret the physical nature of the outflows and the relatively low intensities at higher temperatures. We conclude that there are at least 100 threads along the line of sight. Each thread undergoes an identical cyclical process of heating to about 1×10^6 K followed by a cooling to about 7×10^5 K on a timescale of approximately 80 minutes, whereby the pulses are randomly offset in time for each thread. While having each thread only heated once over the simulation time is a strong assumption, if we were to have instances of multiple heating in some threads and no heating in other threads our results would cease to match the observations.

In addition to the single pulse footpoint heating deemed to yield the greatest agreement with the observations, we explored single pulse apex heating, single pulse uniform heating, and random heating. The best agreement reached through single pulse apex heating, Figure 4.12, has lower Fe X intensity and lower Fe XII intensity and Doppler shift but a Fe VIII redshift. Single pulse uniform heating yielded similar results, with Figure 4.13 being very comparable to Figure 4.12. Most comparable to the observations out of these additional methods was the random heating, but only when the largest heating pulse was applied near the footpoint as in the single pulse

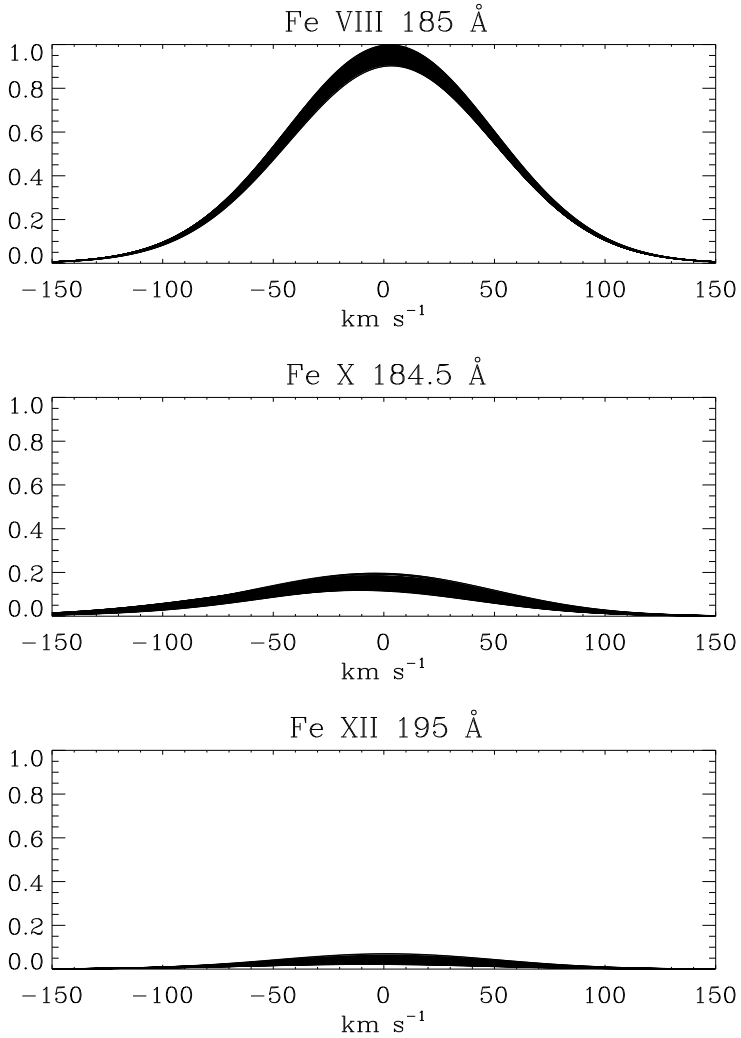

Figure 4.12: Synthetic line profiles, from a 7850 s simulation using single pulse apex heating, for a loop consisting of 100 strands. There is a 50 s interval between each plotted line.

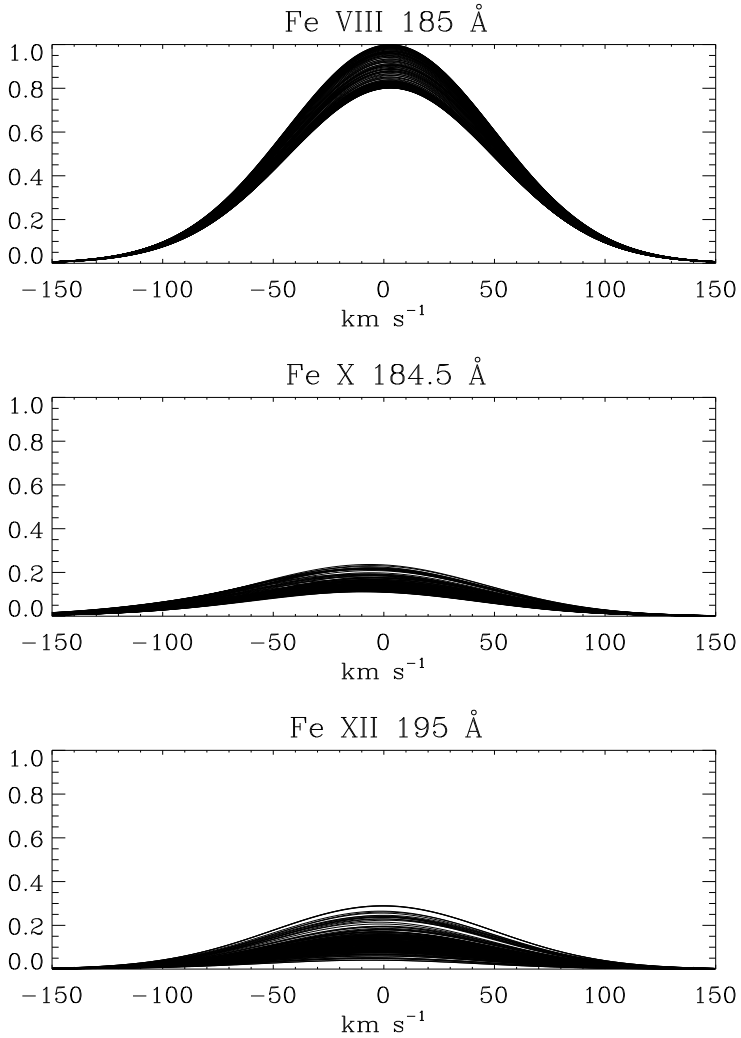

Figure 4.13: Synthetic line profiles, from a 8265 s simulation using single pulse uniform heating, for a loop consisting of 100 strands. There is a 50 s interval between each plotted line.

case.

The case of single pulse footpoint heating yielded the line profiles that best matched the observations compared to the random heating, the single pulse apex heating, and the uniform loop heating. However the single pulse footpoint heating rarely displayed any Fe VIII redshifts in contrast to all three of the other methods yielding them consistently. This could be interpreted to mean that the observed Fe VIII redshift was down to instrument error or other similar factors due to the other attributes comparing favourably to the observations. Alternatively, we may be able to obtain a better fit in future with a dedicated open-structure model.

Chapter 5

Modelling of an Explosive Event Observed by SUMER & TRACE

To fully understand coronal heating, we must first understand the different solar processes that move energy throughout the solar atmosphere. TRACE observations have revealed a short cold loop evolving over a small timescale, seemingly with multiple explosive events occurring along its length. An adaptive hydrodynamic radiation code was used to simulate the loop under non-equilibrium ionisation. Footpoint heating was considered as a possible scenario to reproduce the observations. The simulation results were converted into synthetic observations through forward modelling, for comparison to SOHO/SUMER spectral observations of the loop. The modelling reveals that a single pulse is sufficient to replicate the observed behaviour.

5.1 Introduction

While it is likely that a thorough understanding of all of the different solar phenomena is necessary to solve the coronal heating problem, loops are of particular interest due to their connective nature. They allow for energy to move from the solar interior up into the atmosphere, potentially being released through reconnection (Parker, 1988), shock heating, resonant absorption (Hollweg and Yang, 1988), wave turbulence, or phase mixing (Ofman and Aschwanden, 2002). A comprehensive re-

view of coronal loops is given by Reale (2014), while insight into their spatial scales is presented by Brooks et al. (2013).

First discovered by Brueckner and Bartoe (1983), explosive events are highly dynamic plasma motions defined by their signature non-Gaussian line profiles and short timescales. Innes et al. (1997) found that they can occur in bursts, with Ning et al. (2004) noting a recurrence rate often around 3–5 minutes long and that their profiles can return almost to their quiet Sun shape between events. Doyle et al. (2006b) showed how explosive events can occur as a series of bursts of energy. More recently Huang et al. (2014) found, on a subarcsecond scale, an explosive event associated with continuous plasma ejections and retractions. Doyle et al. (2005a) found that there may be two types of explosive events, their findings suggest that one type is formed in the low chromosphere and the other in the mid-to-high transition region.

The following work is made up of an investigation into a loop observed to be undergoing a transient event. The observations were carried out jointly by TRACE (Section 2.2) and SOHO/SUMER (Section 2.1). Detailed hydrodynamic loop simulations are carried out with the results being forward modelled into synthetic line profiles for comparison to the observations. This is carried out under non-equilibrium ionisation using the HYDRAD code (Section 2.5).

5.2 Observations

The following work investigates an explosive event observed by SUMER on 2 June 1999 from 09:17:11 to 09:39:52 UT. The observations were carried out using slit 8 ($0.3'' \times 120''$) in raster mode with an exposure time of 25 s. The event was also observed by TRACE with a cadence of 10 s.

The SUMER line profiles for N V 1238 Å ($\sim 2 \times 10^5$ K) and O V 629 Å ($\sim 2.5 \times 10^5$ K) are shown in Figures 5.2 and 5.3 respectively. In the case of the N V they are indicative of an explosive event due to the non-Gaussian profiles and Doppler shifts (Madjarska et al., 2009). The O V profiles were attributed to the background radi-

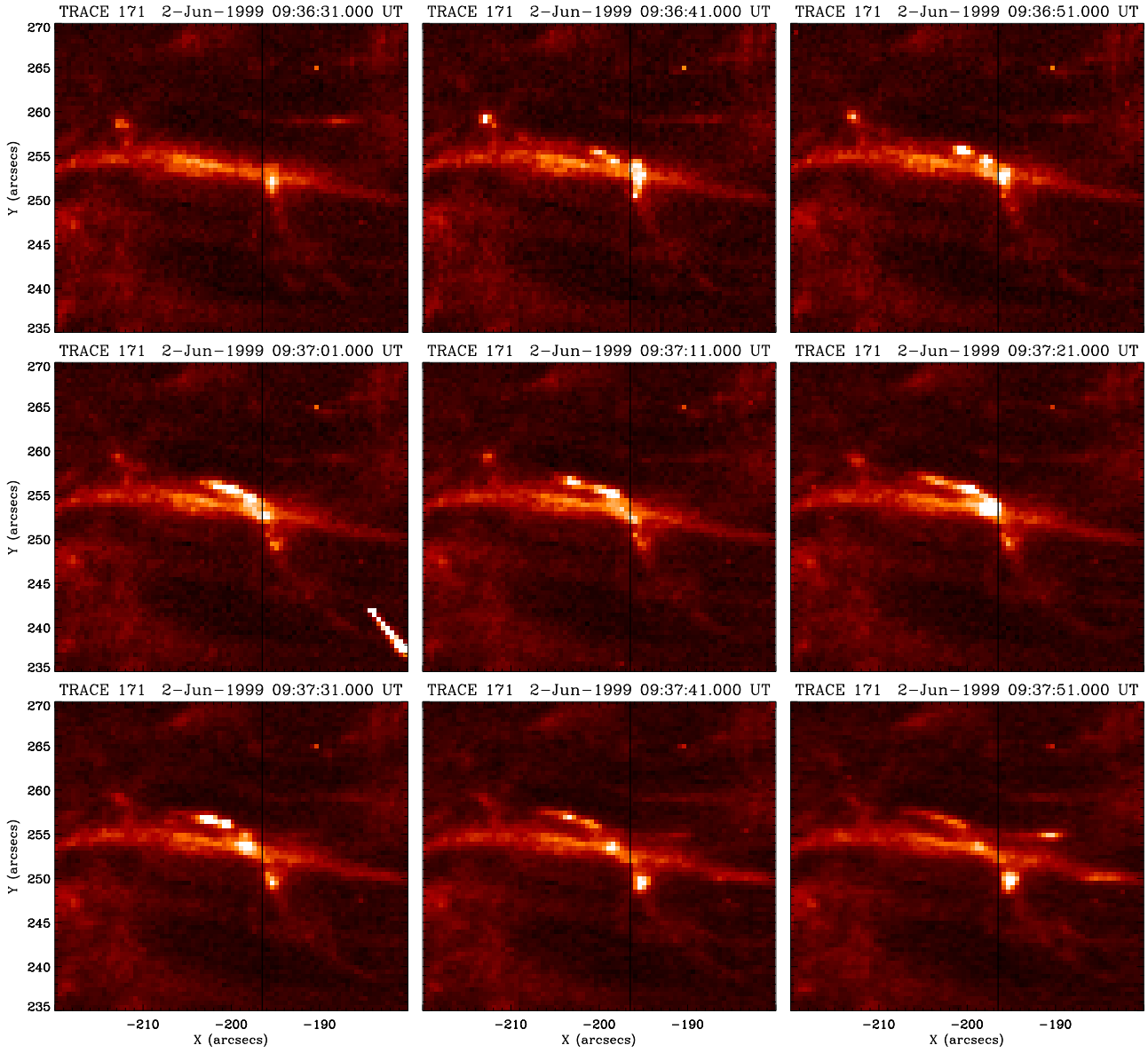

Figure 5.1: TRACE 171 Å images at a cadence of 10 s showing the loop where the event was observed as a diagonal feature. The horizontal bright feature is seen to be intersecting the loop. A solid black vertical line indicates the position of the SUMER slit.

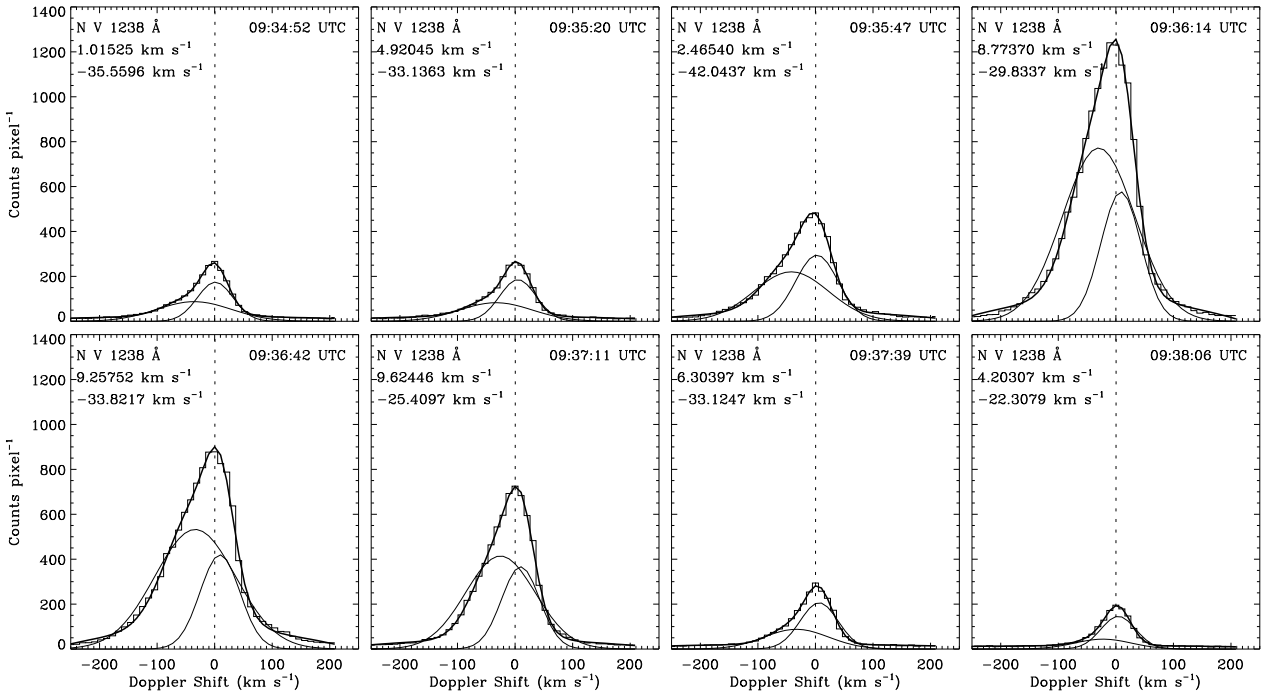

Figure 5.2: Excerpt of the SUMER data showing the double Gaussian fitted N V 1238 Å line profiles made up of 6 pixels (slit Y = 240″–245″) from the loop's first footpoint. The topmost Doppler shifts correspond to the core components and the lower shifts the secondary components. The thin solid lines depict the core and secondary Gaussian fits, while the thick solid line represents the overall fit.

ation due to their strong similarity to the included background profiles taken away from the events. However the ionisation fractions of the ions (Figure 5.4) suggests a response should be visible in both sets of profiles. The observed O V response could be due to the explosive event occurring in a high electron density region, resulting in a diminished line flux because of the metastable populations (Doyle et al., 2005a,b, 2006a). Looking at the same region using the TRACE 171 Å passband (Figure 5.1) and overlaying the position of the SUMER slit the involvement of a loop becomes apparent. The loop targeted by the following simulations can be seen going from the bottom centre up to the centre left of the figure, though the full extent of the loop was not observed.

The N V profiles shown in Figure 5.2 are taken from a lower part of the SUMER slit where the loop is not visible in the TRACE 171 Å image (Figure 5.1), this portion of the loop is termed the first footpoint going forward. Several SUMER pixels are chosen to make up the profiles as opposed to just one in order to minimise

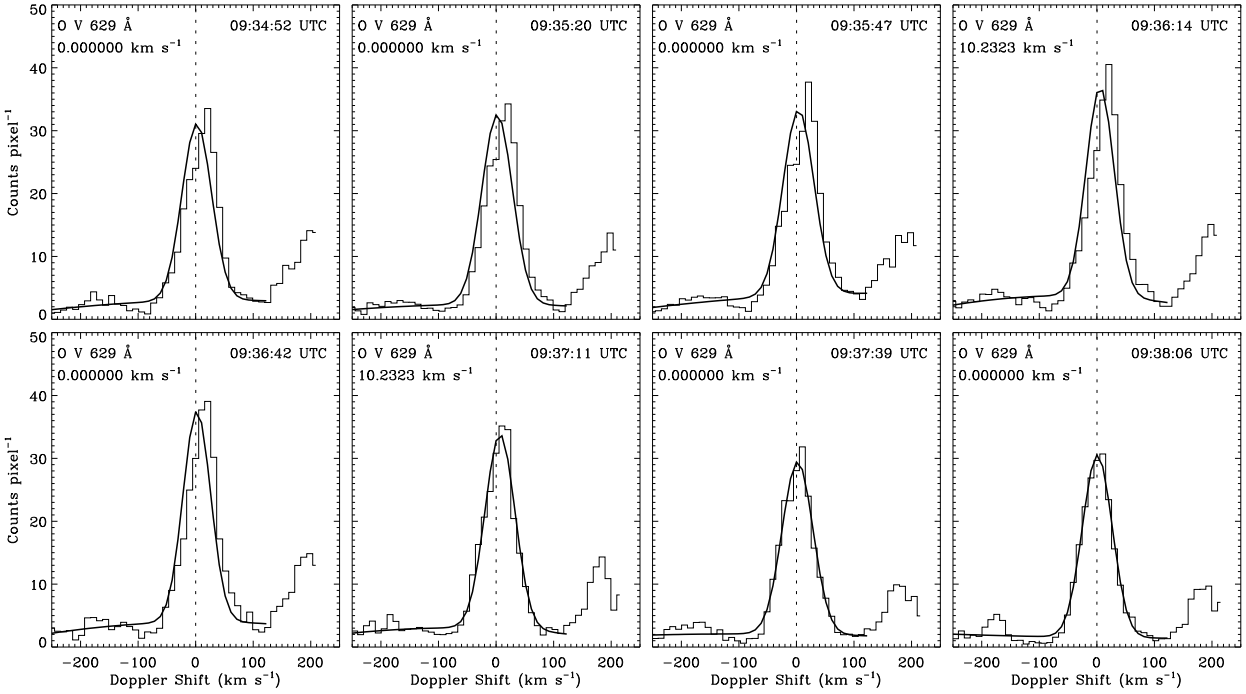

Figure 5.3: Excerpt of the SUMER data showing the single Gaussian fitted O V 629 Å line profiles made up of 6 pixels (slit Y = 240″–245″) from the loop's first footpoint. The thin solid lines depict the Gaussian fit.

noise. These profiles are fitted with a double Gaussian because of the asymmetry, taking the form of a blue wing enhancement, evident in the middle row of the figure. Profiles taken from directly over a visible portion of the loop (Figure 5.5, Figure 5.6) were discarded due to the large, relatively horizontal, bright feature being beyond the scope of our modelling. This meant that only the footpoint region could be modelled because the straight slit could only intercept the loop in up to two places. The presented N V profiles show an initial relatively low intensity small blueshift which undergoes a sudden increase of intensity before returning to its initial state over a period of 175 s. In contrast the corresponding O V profiles (Figure 5.3) show only insignificant fluctuations with central profiles, which combined with the response of the cooler N V line suggested low temperatures.

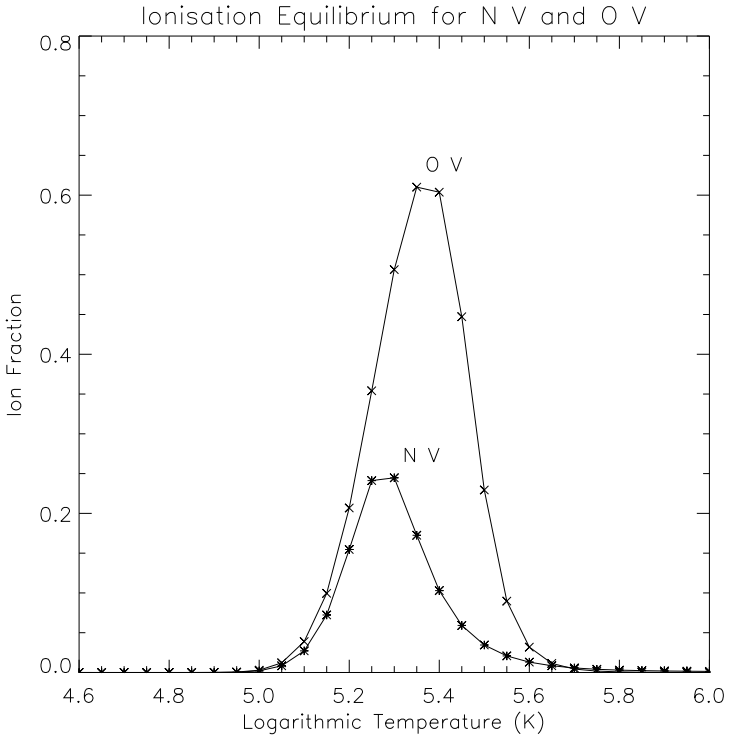

Figure 5.4: The ionisation fraction of the N V and O V ions, created using CHIANTI.

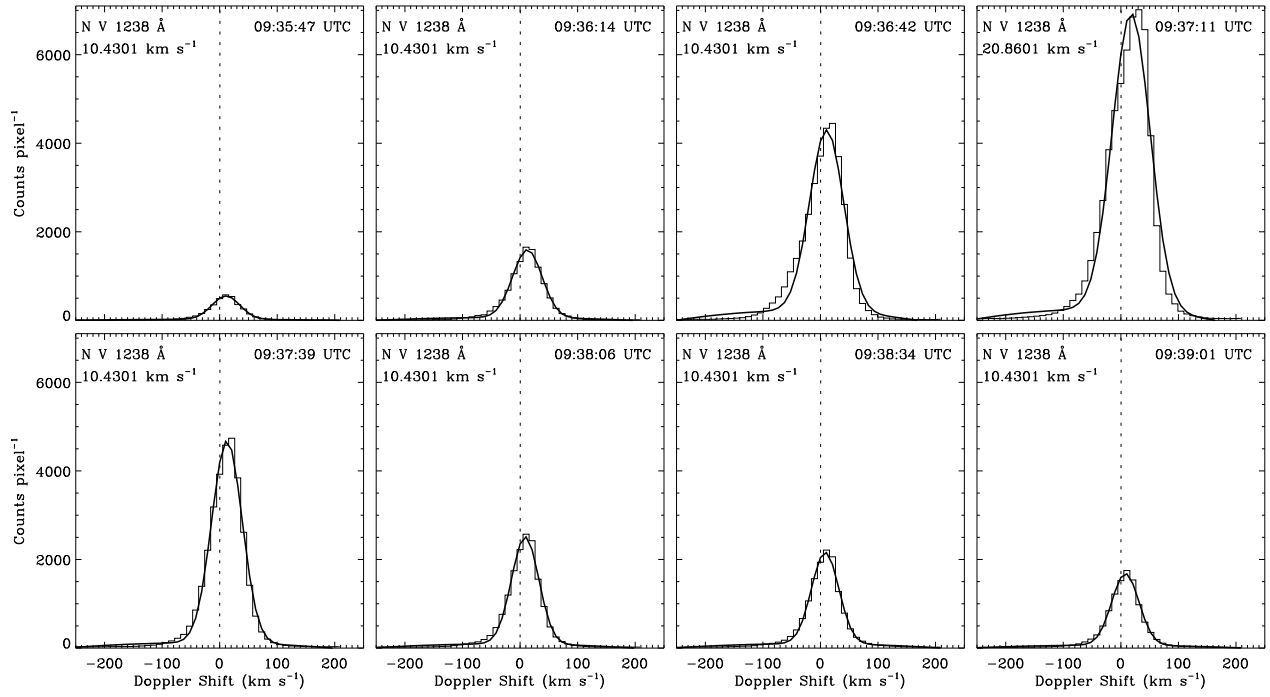

Figure 5.5: Excerpt of the SUMER data showing the single Gaussian fitted N V 1238 Å line profiles made up of 4 pixels (slit Y = 250″–253″) from the loop apex. The thin solid lines depict the Gaussian fit.

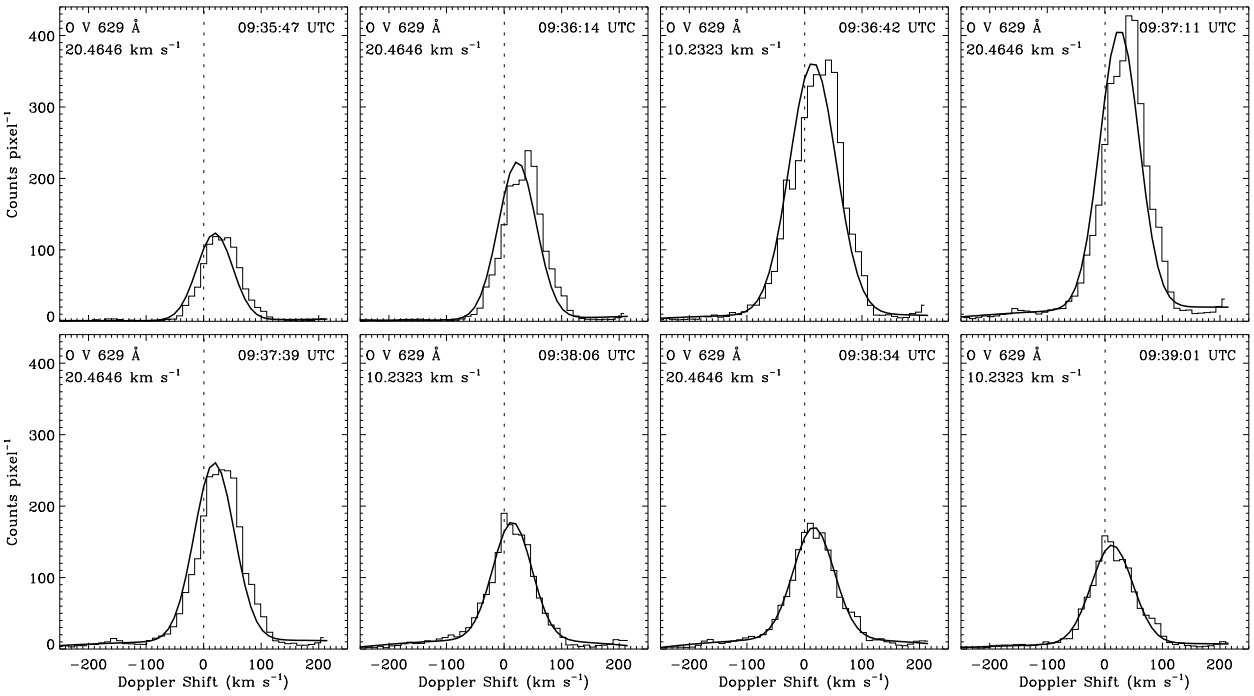

Figure 5.6: Excerpt of the SUMER data showing the single Gaussian fitted O V 629 Å line profiles made up of 4 pixels (slit Y = 250″–253″) from the loop apex. The thin solid lines depict the Gaussian fit.

5.3 Modelling

The N V emissivity table in the forward modelling part of HYDRAD (Section 2.5) was updated to include the 1238.823 Å line using CHIANTI (Dere et al., 1997; Del Zanna et al., 2015). The instrument response functions for the SUMER 629 Å and 1238 Å were set to range from 629.15–633.35 Å and 1238.45-1239.15 Å respectively, corresponding to the width of their response in CHIANTI. The responses themselves were set to 1 resulting in relative intensity comparisons, for example looking to see if a factor increase was replicated, rather than direct comparisons of the values. While there is an actual response value in reality, the constant approximation is valid because there will be almost no variation along the narrow range of the slit.

The loop inclination was assumed to be zero for simplicity, reducing the number of variables to investigate. Other variables were altered in a series of informed trial and error to deduce their likely values, using the results from one simulation to choose the inputs for the next.

It is apparent from the observed TRACE imagery (Figure 5.1) that the overlaid SUMER slit does not align along the axis of the loop. To allow for meaningful comparison of the simulated loop to the observed, a section was taken from near the first footpoint of the simulated loop and used to generate synthetic line profiles. When viewing the semicircular loop from above, looking down at the apex, the section corresponds to one pixel of the SUMER slit. This is a potential source of error due to the footpoint itself not being visible in the TRACE images, therefore deciding how much of the loop likely falls within the slit can not be confirmed directly.

The lack of an observed O V response (Figure 5.3) proved troublesome in determining the temperature regime because of the temperature changes caused by the heating pulses generally causing increases in intensity. To aid what was essentially a parameter search, a plot displaying the temperature, density, and intensity of the summed loop section was devised (Figure 5.7) to use instead of just synthetic line profiles due to the additional information provided.

The simulations were conducted with a cadence of 1 s whereas the observations had an exposure time of 25 s. The model results were grouped into blocks of 25 as far as possible, with the first block additionally containing the initial profile, and the last block sometimes containing less depending on the overall simulation time. These blocks were then simply averaged to produce data for proper comparison to the observations.

5.4 Results and Discussion

The observations were most closely matched when the loop was taken to be 30 Mm long, including two chromospheric footpoints of 2 Mm each, with an initial footpoint density of 1.6×10^{10} cm^{-3} yielding an apex temperature of 7×10^5 K supported by a uniform background heating rate of 1.1×10^{-4} erg cm^{-3} s^{-1}. This density was used for the majority of the simulations undertaken due to it yielding the lowest N V and O V initial intensities while still being able to withstand a relatively large

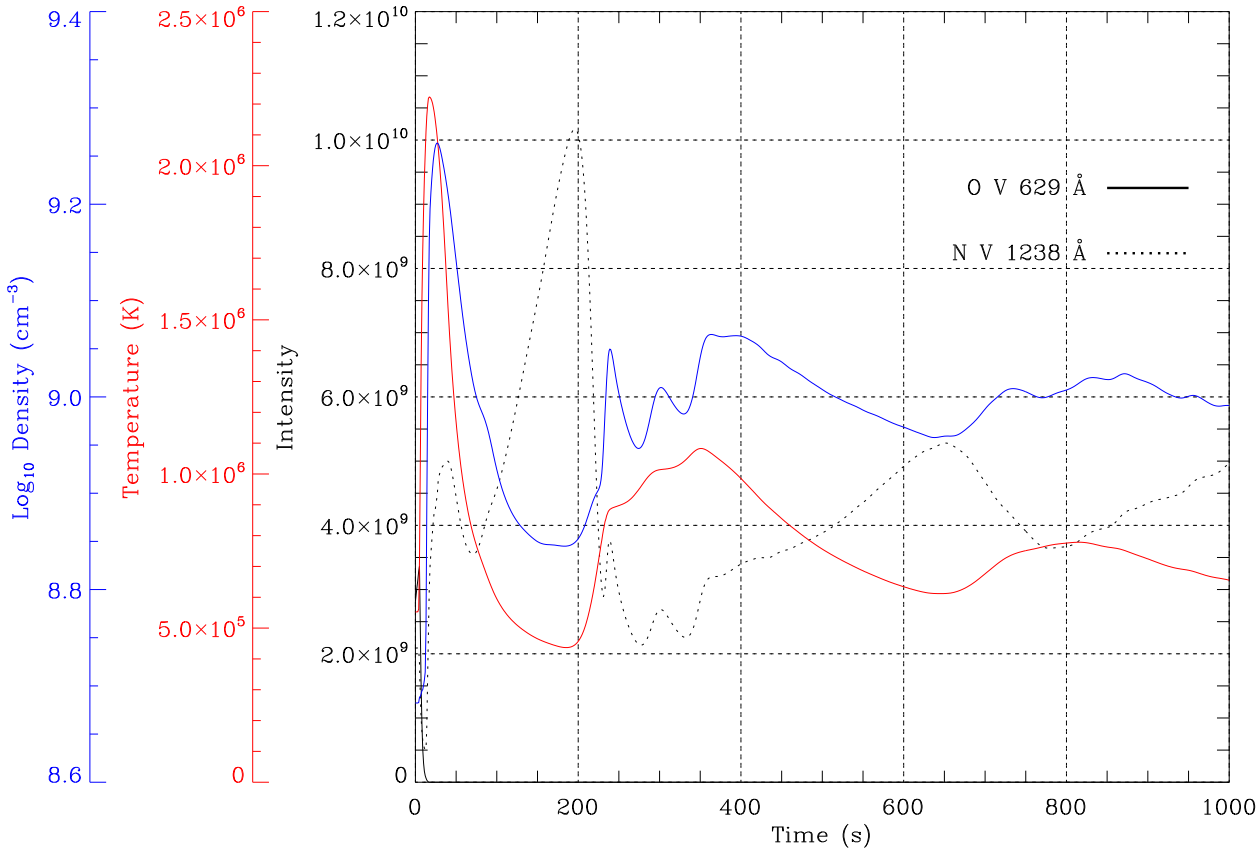

Figure 5.7: The density, temperature, and intensity (arbitrary units) of the loop section summed (4.65–6.00 Mm) to produce the final synthetic line profiles shown in Figure 5.11. The solid black line represents the O V intensity, the dotted black line the N V intensity, the red line the temperature (K), and the blue line the base 10 logarithmic density (cm^{-3}).

heating pulse instead of the chromospheric footpoints getting heated such that the loop touches the boundary. Starting with as little intensity as possible allows for the biggest jump in relative intensity during heating. This initial state was then subjected to a heating pulse with a maximum impulsive heating rate of 2 erg cm^{-3} s^{-1} applied to the top of the chromosphere at the first footpoint. The time dependent heating pulse was applied for a total of 36 s made up of a 4 s linear increase, 2 s plateau, and a 30 s linear decrease.

Initially it was assumed that the loop would be relatively cold due to the low temperatures of the N V and O V lines. Using a footpoint density of 3×10^8 cm^{-3}, which yielded an apex temperature of 1.1×10^5 K, three simulations were conducted which varied only in volumetric heating rate of the time dependent pulse. The logic was that the pulse would raise the temperature of the loop, prompting a rise and fall in the N V response whilst not heating up enough to be noticeable in the O V response. The synthetic N V profiles were initially very promising, depicting a rise and fall in intensity with an almost constant blueshift. However the O V intensity was greater than that of N V, for example in one instance the O V peak was 3 times more intense and this was inconsistent with the observations.

From here the loop length was revised up from 20 Mm to its final 30 Mm and a reference simulation was devised. For this run the initial footpoint density was ramped up such that the apex temperature was 2.9×10^6 K. Both the background heating and the heating pulse were disabled and the loop was just left to cool for a long time. This resulted in some insight into how the two diagnostic lines were reacting to the loop temperature. It was decided that an apex temperature of 7×10^5 K (footpoint density 1.6×10^{10} cm^{-3}) should be used going forward because the N V was shown to be above the O V intensity around that temperature similar to the observations. The loop apex of this simulation is represented by Figure 5.8, notable is that though O V fell to zero it was not noticed at this point and therefore it was not a factor in the choice of parameters for the ensuing simulations.

Due to how quickly the intensity changed in the observations, attempts were

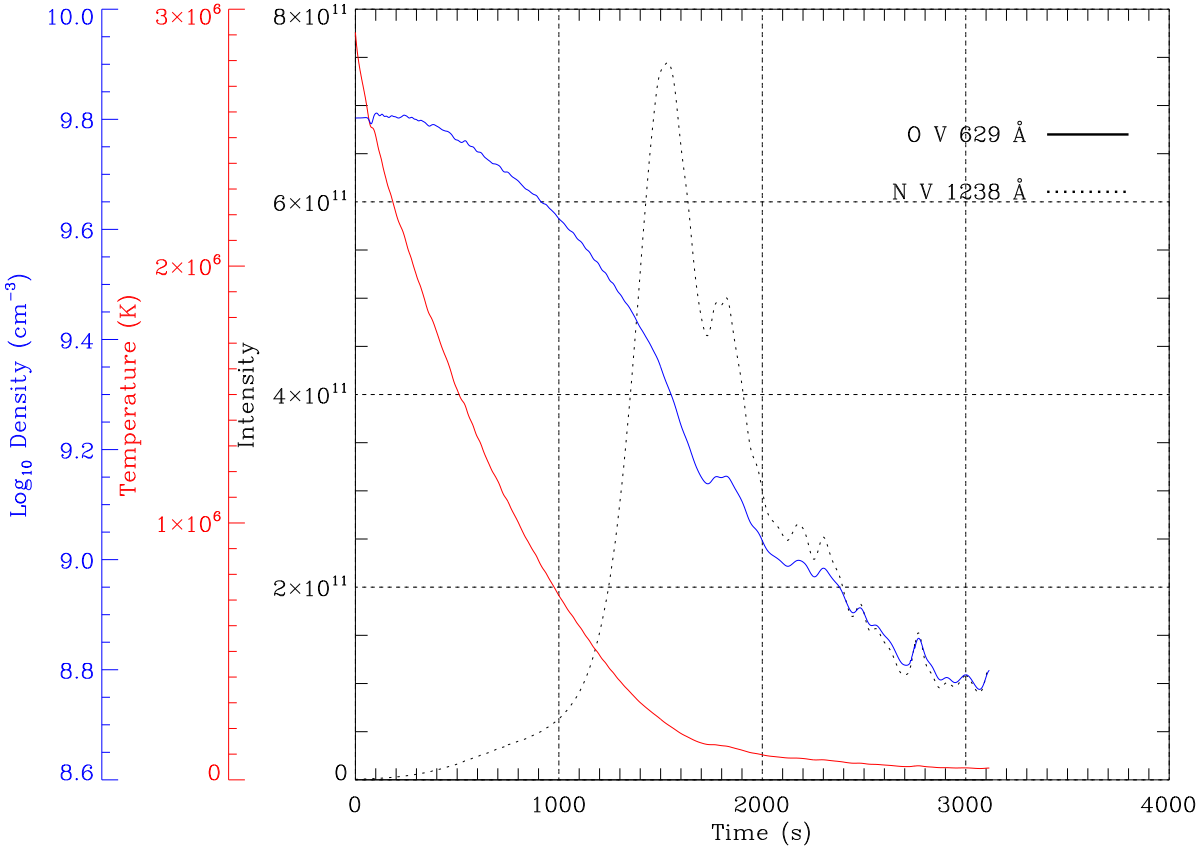

Figure 5.8: The density, temperature, and intensity (arbitrary units) of a loop section summed (14.68–15.40 Mm) at the apex of the loop. The dotted black line represents the N V intensity, the red line the temperature (K), and the blue line the base 10 logarithmic density (cm^{-3}). It is not possible to see the O V solid black line, however its intensity begins at approximately 1×10^8 and generally falls with time before becoming zero for the remainder at approximately 1200 s.

made to create shock heating in the loop. For this the original 60 s heating pulse duration was shortened to 10 s and the heating rate increased. In the runs up to and including a peak temperature of 1.5×10^6 K, O v dominated N v in maximum intensity and had a higher intensity for a majority of the simulation time (Figure 5.9). However in the run a step higher in volumetric heating rate, where the loop reached a peak temperature of 2×10^6 K, O v was seen to plummet to zero during the initial spike in temperature and density after a brief minor increase in intensity (Figure 5.10). Despite the subsequent rapid fall in the temperature and density the O v line remained at zero throughout the rest of the simulation time. The N v line on the other hand initially had a minor decrease in intensity before undergoing an appealing rise and fall. This promising behaviour seen in a simple intensity against time plot did not carry over to the synthetic line profiles due to the summations used to match the observations exposure time, however it was the first time that N v consistently beat O v in intensity.

To further investigate the effects of temperature and density on the intensity of the two diagnostic lines a set of 10 simulations were devised. Here the initial footpoint densities were set such that the apex temperatures ranged from 1×10^5–1×10^6 K in steps of 1×10^5 K. A relatively moderate (0.2 erg cm^{-3} s^{-1}) heating pulse was used for the highest temperature loop, and then scaled down for the cooler ones proportionally to their background heating rates. It was found that both lines peaked in intensity in the same temperature regime of approximately 3.2×10^5 K, with O v eclipsing N v by an order of magnitude. From this peak the intensities decreased for both lines in each temperature direction. However at an unknown point the intensity of N v started recovering while O v continued decreasing. This culminated in N v reaching approximately 60% of its lower temperature peak intensity, approximately two orders of magnitude higher than O v.

This cemented the choice of 1.6×10^{10} cm^{-3} for initial footpoint density because it provided the lowest initial intensity for N v and resulted in N v being more intense than O v during the heating. Here focus shifted to the variables of the heating pulse

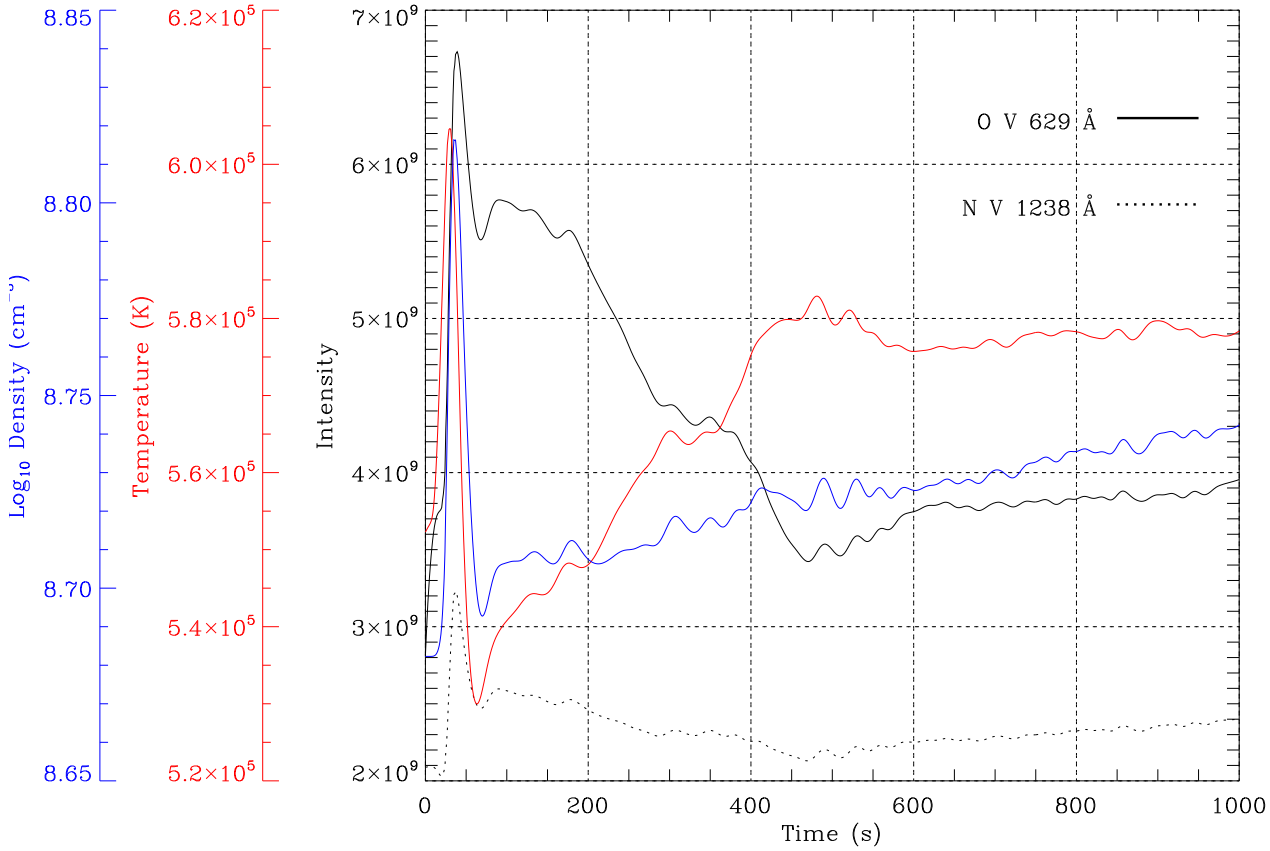

Figure 5.9: The density, temperature, and intensity (arbitrary units) of a summed loop section (4.65–6.00 Mm). The solid black line represents the O v intensity, the dotted black line the N v intensity, the red line the temperature (K), and the blue line the base 10 logarithmic density (cm^{-3}). The simulation parameters are identical to those of Figure 5.7 except for a 20 times decrease in volumetric heating rate and a shorter heating duration of 10 s.

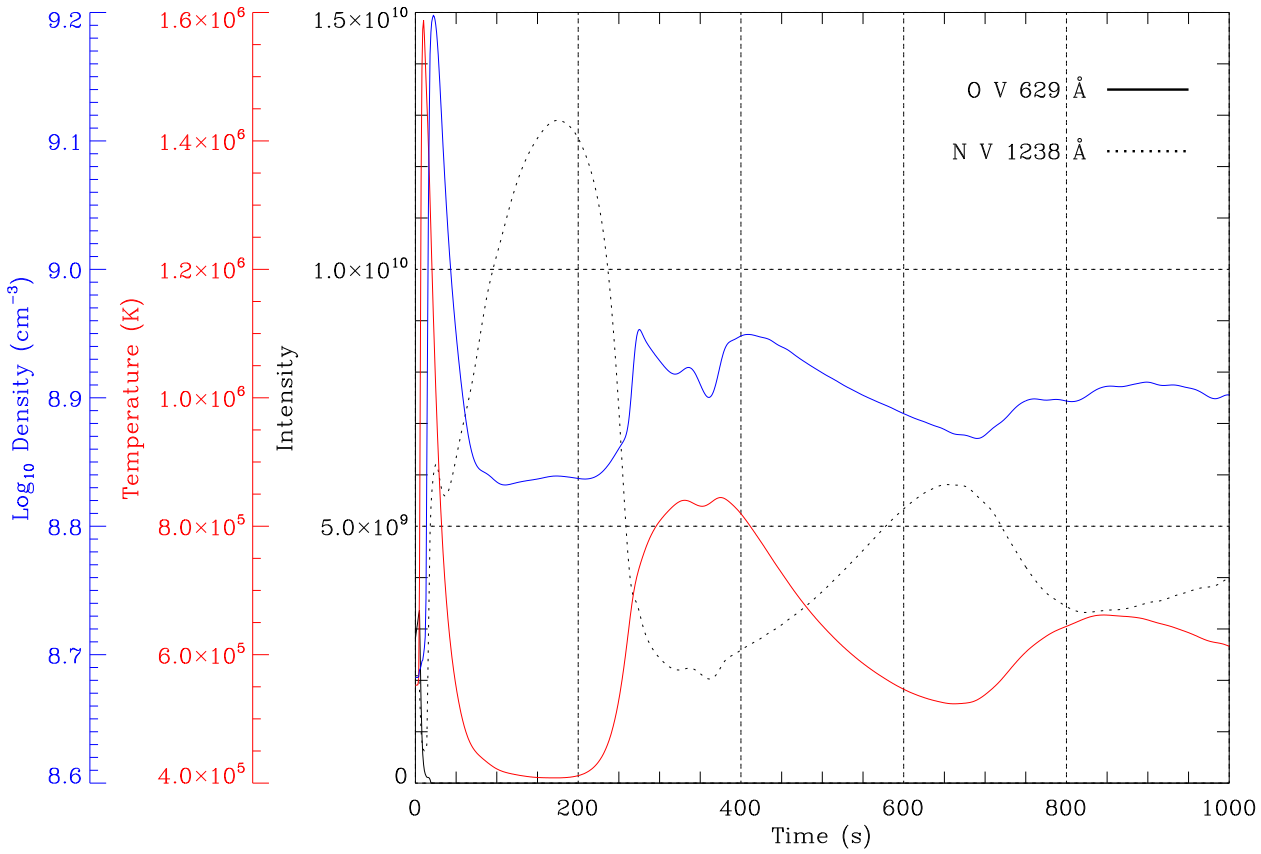

Figure 5.10: The density, temperature, and intensity (arbitrary units) of a summed loop section (4.65–6.00 Mm). The solid black line represents the O V intensity, the dotted black line the N V intensity, the red line the temperature (K), and the blue line the base 10 logarithmic density (cm^{-3}). The simulation parameters are identical to those of Figure 5.9 except for a 20 times increase in volumetric heating rate.

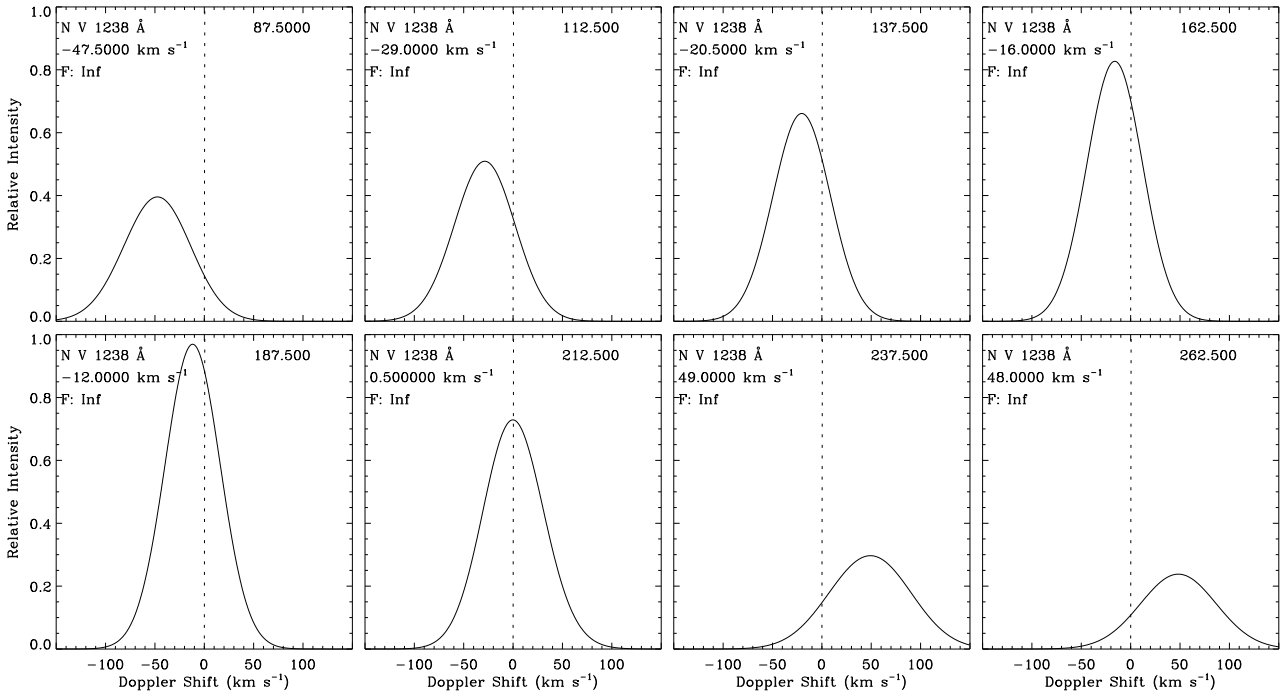

Figure 5.11: Forward-modelled N v line profiles corresponding to Figure 5.7. The top right number is the time in seconds, the velocity is the Gaussian fitted Doppler shift, and the F number is the ratio of the peak of the profile to its corresponding O v peak.

to see if the earlier result with these loop settings could be improved.

In looking at the scale height it was found that it could only be increased by so much before requiring an increase in the duration of the heating pulse in order to keep the O v intensity down. In loops that were heated to temperatures in the same range, meaning 1.7×10^6–1.89×10^6 K, with a heating pulse scale height of 1 Mm the rapid 10 s pulses failed to floor the O v intensity whereas the longer 30 s and 60 s pulses both caused it to drop to zero as before. However at scale heights of 0.5 Mm and below the 10 s pulses were able to achieve the same behaviour, though the turning point is likely to be a bit higher as this was not narrowed down but could be in a future study.

The N v observations at the loop apex (Figure 5.5) show a rise and fall in intensity on the same timescale as at the footpoint (Figure 5.2) but approximately 50 s later and with a peak almost 6 times higher. In contrast however, the O v profiles at the apex also show a rise and fall in intensity while only background is registered at the

footpoint.

5.5 Summary and Conclusions

It was found, through non-equilibrium hydrodynamic modelling, that the observed loop can be approximated well by a 30 Mm loop. The loop includes two chromospheric footpoints of 2 Mm each with an initial footpoint density of 1.6×10^{10} cm^{-3} which corresponds to an initial loop apex temperature of 7×10^5 K. Therefore forward modelling allows us to infer the initial temperature as other temperatures yield profiles inconsistent with the observed line profiles. Recreating the observed flow was achieved by applying a time dependent heating pulse to the top of the chromosphere at the first footpoint. This pulse had a maximum volumetric heating rate of 2 erg cm^{-3} s^{-1} and was applied for a total 36 s in the form of a 4 s linear increase, 2 s plateau, and a 30 s linear decrease.

We find that the O V observations consist entirely of background intensity because of the zeroed response in the synthetic profiles. We note that this is not a computational issue as it has been seen to fall to zero and then rise again later on as loop conditions change. For example Figure 5.12 is the same simulation as Figure 5.10 but it shows the data from a different section of the loop, summed closer to the footpoint. In the figure the O V intensity undergoes a very brief initial increase before falling to zero, but it later recovers and peaks before substantially falling again but remaining above zero.

With regards to the N V observations we find agreement in principle in that we have a rise in intensity and then a fall back to a little bit below the initial intensity (Figure 5.11). However the timing is not in agreement as we have three frames of rise before the peak intensity compared to the observed one. We felt that it could be improved with further simulations. While the observations display a constant blueshift throughout the time period, our initially blueshifted loop becomes redshifted due to the return flow of material as the intensity falls. We postulate that this is due to the background contributing more to the observed Doppler shift than

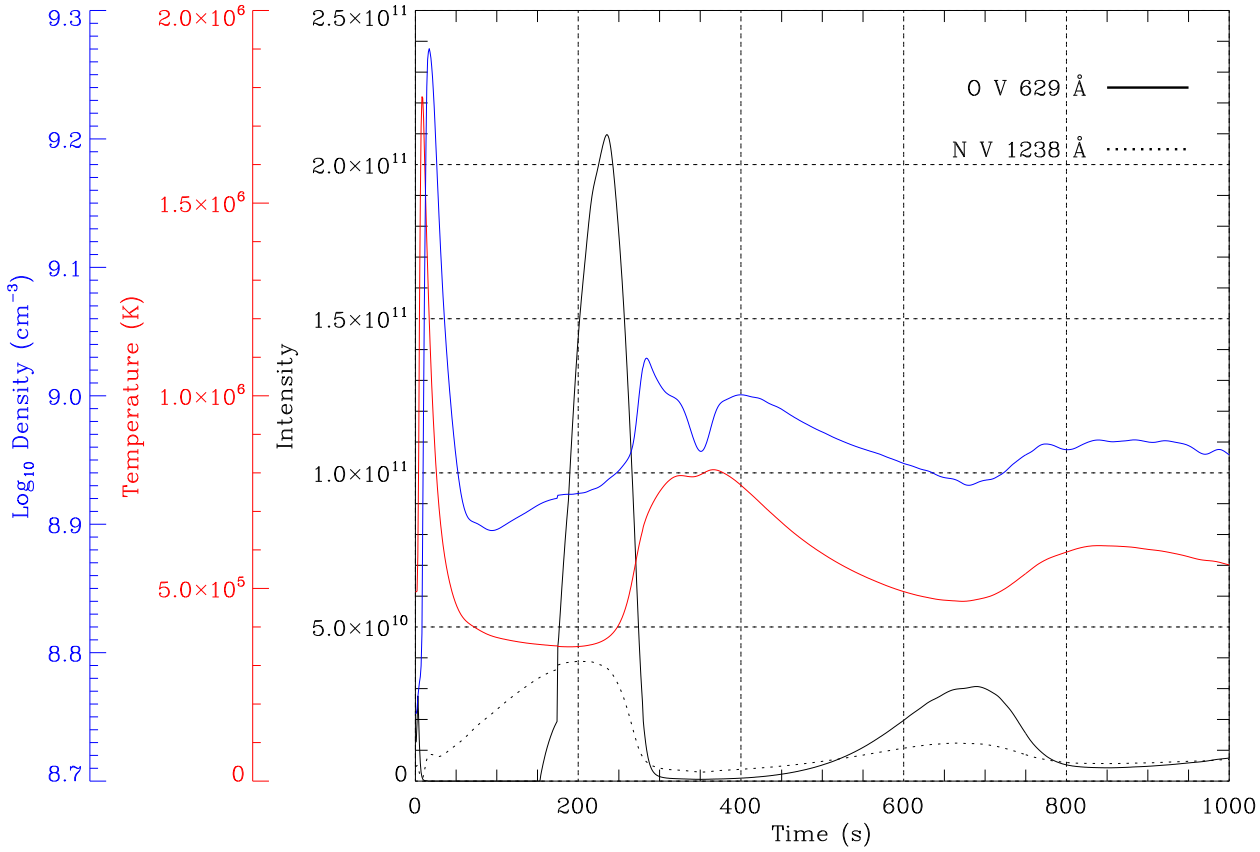

Figure 5.12: The density, temperature, and intensity (arbitrary units) of a summed loop section (3.30–5.00 Mm). The solid black line represents the O V intensity, the dotted black line the N V intensity, the red line the temperature (K), and the blue line the base 10 logarithmic density (cm^{-3}). The simulation parameters are identical to those of Figure 5.10.

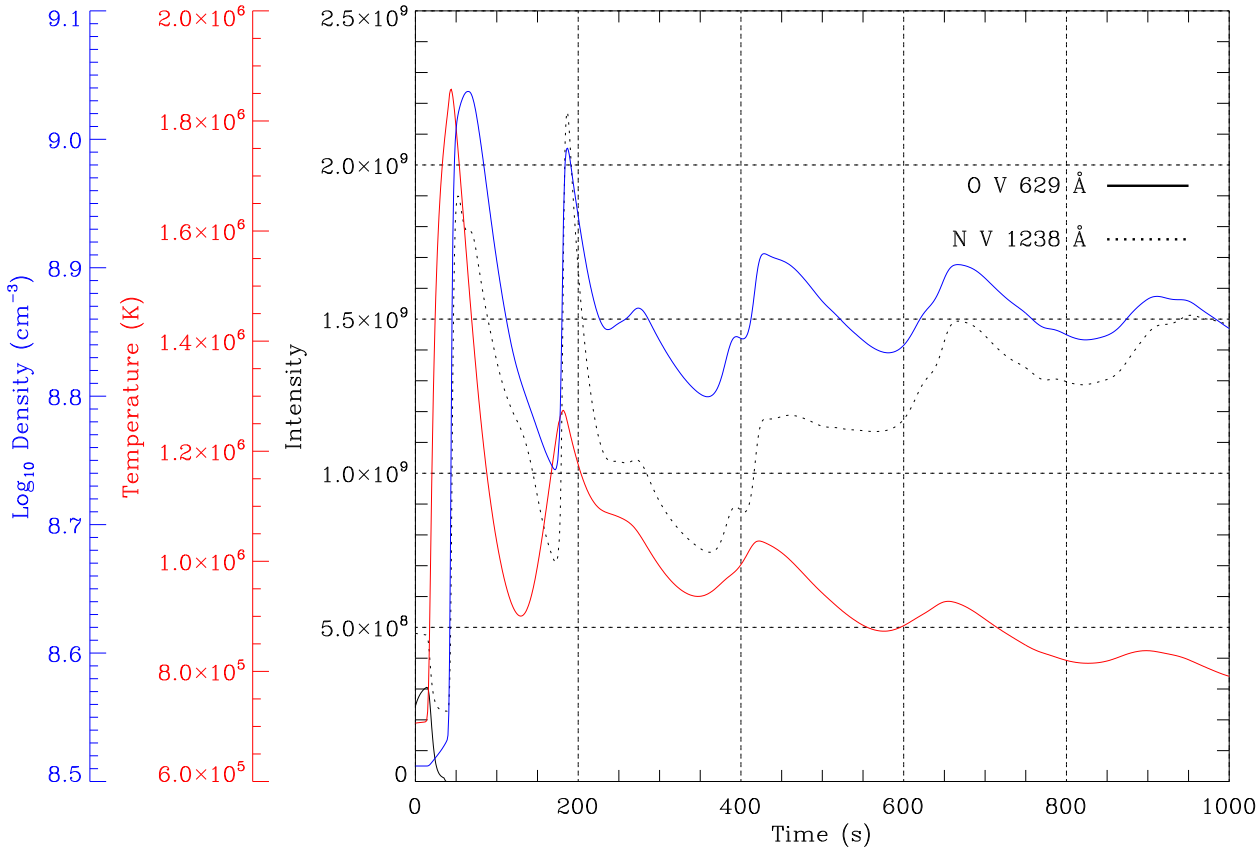

Figure 5.13: The density, temperature, and intensity (arbitrary units) of a loop section summed (14.78–15.5 Mm) at the apex of the loop. The solid black line represents the O V intensity, the dotted black line the N V intensity, the red line the temperature (K), and the blue line the base 10 logarithmic density (cm^{-3}).

the loop itself, resulting in the masking of the redshift.

The N V observed line profiles display a relatively consistent initial state for the first four frames (Figure 5.2), the transient pulse for the next four, and then it returns to a state very similar to the initial four. However our results begin 75 s into the simulation where the heating pulse is already over but material is still flowing along the loop towards the opposite footpoint. This suggests that the mechanism of action for the observed event was not itself observed, or was possibly not a heating pulse.

The TRACE observations (Figure 5.1) suggest the involvement of multiple pulses along the loop due to the different brightenings shown simultaneously in different positions. However this is inconsistent with our findings, arrived at using a single heating pulse.

Contrary to the observations where the apex has an O V response and the footpoint doesn't, our simulations find the O V response fell the closer we got to the apex (Figure 5.13) from the chromosphere once the heating had begun. We therefore conclude that the two events are not likely to be connected through the loop. A likely explanation for the high O V intensity at the apex is the bright feature intersecting with the loop as seen in the TRACE observations (Figure 5.1).

Chapter 6

Summary & Conclusions

The body of work composing this thesis was undertaken with the coronal heating problem in mind. A full explanation for coronal heating requires us to understand the Sun as much as possible, particularly its mechanisms for generating, transporting, and dissipating energy. We combined observations with detailed non-equilibrium ionisation simulations to investigate three transient events that have occurred within the solar atmosphere. The simulations allowed us to create synthetic observations for comparison to the actual observations such that we could suggest properties for the observed events such as temperatures, the energy involved, Doppler shifts, and others.

The first body of research (Chapter 3) reproduced AIA observations reported by Innes and Teriaca (2013) interpreted as a flow along a loop. Our simulations were able to create synthetic light curves to match the observations. While injecting cold plasma into the loop's first footpoint was attempted, we found the best match when a single heating pulse was applied at the first footpoint of a 10.2 Mm long loop. This caused chromospheric material to flow up and along the loop before rebounding at the opposite footpoint and returning. As this work used absolute intensity, which is affected by the loop's cross-sectional area, we were able to calculate the heating pulse to be consistent with the energy of a nanoflare.

The investigation of an active region in Chapter 4 took observations from EIS across a range of three spectral lines of different temperatures. We created synthetic

line profiles to model the relative intensity of the three spectral lines and their Doppler shifts using single pulse footpoint heating, single pulse apex heating, single pulse uniform heating, and random heating. We found that the observed structure was best modelled by a multi-threaded loop 100 Mm long containing at least 100 threads along the line of sight, each undergoing a cyclical process of heating and cooling within a time interval of 80 minutes.

Centred around an explosive event observed by SUMER and TRACE, Chapter 5 created synthetic line profiles to match the SUMER observations. We found that the observations were best approximated by a 30 Mm loop with a single heating pulse applied at the top of its first footpoint. Differences between our results and the observations allowed us to infer that the O v observations consisted entirely of background intensity at the footpoint. A rise and fall in the intensity of N v at the footpoint was reproduced, however the N v observations at the footpoint were postulated to have the background contributing significantly to the Doppler shift, and the O v intensity at the apex was likely due to the bright intersecting feature seen in the TRACE observations (Figure 5.1). This work highlights the need to use multiple observations, for example spectral and imaging, where possible to allow for the most accurate interpretation of what is seen, and to be exceedingly careful of contributions from both the background and other phenomena in addition to that of your target.

6.1 Future Work

The techniques learned through carrying out this research could be applied to the modelling of other loop observations in a shorter amount of time. It would be interesting to see if more complicated scenarios could be replicated, for example in Chapter 5 the observed loop was intersected twice by the SUMER slit however the relatively horizontal feature seen in the TRACE observations (Figure 5.1) is believed to contaminate the data from the higher intersection. The modelling of both structures separately and then combining the forward modelled intensity could

be investigated if the contaminating feature could be modelled as a loop.

Looking back at Chapter 4 where the observations were not clear as to whether or not the structure was a loop or an open structure, comparisons of our results from loop simulations versus open structure simulations would be interesting. An open structure model (Mueller, 2015) was briefly investigated but not pursued due to time constraints.

With the HYDRAD code having been used for all of the research in this thesis, a natural progression would be the development of tools to accompany it. While a robust tool with a simple to use interface, a way to automate a parameter search for example would have been of great value time wise. Additionally, a significant portion of time was spent on the creation of analysis procedures in IDL (Interactive Data Language) which if made more general and user friendly could be a useful accompaniment. Such work may not create direct science output itself, but increasing the efficiency of users could result in studies taking less time paving the way for more.

Bibliography

Adelberger, E. G., A. García, R. G. H. Robertson, K. A. Snover, A. B. Balantekin, K. Heeger, M. J. Ramsey-Musolf, D. Bemmerer, A. Junghans, C. A. Bertulani, J.-W. Chen, H. Costantini, P. Prati, M. Couder, E. Uberseder, M. Wiescher, R. Cyburt, B. Davids, S. J. Freedman, M. Gai, D. Gazit, L. Gialanella, G. Imbriani, U. Greife, M. Hass, W. C. Haxton, T. Itahashi, K. Kubodera, K. Langanke, D. Leitner, M. Leitner, P. Vetter, L. Winslow, L. E. Marcucci, T. Motobayashi, A. Mukhamedzhanov, R. E. Tribble, K. M. Nollett, F. M. Nunes, T.-S. Park, P. D. Parker, R. Schiavilla, E. C. Simpson, C. Spitaleri, F. Strieder, H.-P. Trautvetter, K. Suemmerer, and S. Typel (2011), "Solar fusion cross sections. II. The pp chain and CNO cycles." *Reviews of Modern Physics*, 83, 195–246.

Aschwanden, M. J. (2006), *Physics of the Solar Corona: An Introduction with Problems and Solutions*, 2nd edition. Springer.

Aschwanden, M. J. and C. E. Parnell (2002), "Nanoflare Statistics from First Principles: Fractal Geometry and Temperature Synthesis." *Astrophys. J.*, 572, 1048–1071.

Aschwanden, M. J., T. D. Tarbell, R. W. Nightingale, C. J. Schrijver, A. Title, C. C. Kankelborg, P. Martens, and H. P. Warren (2000), "Time Variability of the "Quiet" Sun Observed with TRACE. II. Physical Parameters, Temperature Evolution, and Energetics of Extreme-Ultraviolet Nanoflares." *Astrophys. J.*, 535, 1047–1065.

Benz, A. O. and S. Krucker (2002), "Energy Distribution of Microevents in the Quiet Solar Corona." *Astrophys. J.*, 568, 413–421.

Bertaux, J. L., E. Kyrölä, E. Quémerais, R. Pellinen, R. Lallement, W. Schmidt, M. Berthé, E. Dimarellis, J. P. Goutail, C. Taulemesse, C. Bernard, G. Leppelmeier, T. Summanen, H. Hannula, H. Huomo, V. Kehlä, S. Korpela, K. Leppälä, E. Strömmer, J. Torsti, K. Viherkanto, J. F. Hochedez, G. Chretiennot, R. Peyroux, and T. Holzer (1995), "SWAN: A Study of Solar Wind Anisotropies on SOHO with Lyman Alpha Sky Mapping." *Solar Phys.*, 162, 403–439.

Bewsher, D., D. E. Innes, C. E. Parnell, and D. S. Brown (2005), "Comparison of blinkers and explosive events: A case study." *Astron. Astrophys.*, 432, 307–317.

Borrini, G. and G. Noci (1982), "Non-equilibrium ionization in coronal loops." *Solar Phys.*, 77, 153–166.

Bradshaw, S. J. (2009), "A numerical tool for the calculation of non-equilibrium ionisation states in the solar corona and other astrophysical plasma environments." *Astron. Astrophys.*, 502, 409–418.

Bradshaw, S. J. and P. J. Cargill (2006), "Explosive heating of low-density coronal plasma." *Astron. Astrophys.*, 458, 987–995.

Bradshaw, S. J. and P. J. Cargill (2013), "The Influence of Numerical Resolution on Coronal Density in Hydrodynamic Models of Impulsive Heating." *Astrophys. J.*, 770, 12.

Bradshaw, S. J. and J. A. Klimchuk (2011), "What Dominates the Coronal Emission Spectrum During the Cycle of Impulsive Heating and Cooling?" *Astrophys. J. Suppl.*, 194, 26.

Bradshaw, S. J. and H. E. Mason (2003a), "A self-consistent treatment of radiation in coronal loop modelling." *Astron. Astrophys.*, 401, 699–709.

Bradshaw, S. J. and H. E. Mason (2003b), "The radiative response of solar loop plasma subject to transient heating." *Astron. Astrophys.*, 407, 1127–1138.

Bray, R. J., L. E. Cram, C. Durrant, and R. E. Loughhead (1991), *Plasma Loops in the Solar Corona*. Cambridge University Press.

Brooks, D. H., H. P. Warren, I. Ugarte-Urra, and A. R. Winebarger (2013), "High Spatial Resolution Observations of Loops in the Solar Corona." *Astrophys. J. Lett.*, 772, L19.

Browning, P. K., C. Gerrard, A. W. Hood, R. Kevis, and R. A. M. van der Linden (2008), "Heating the corona by nanoflares: simulations of energy release triggered by a kink instability." *Astron. Astrophys.*, 485, 837–848.

Brueckner, G. E. and J.-D. F. Bartoe (1983), "Observations of high-energy jets in the corona above the quiet sun, the heating of the corona, and the acceleration of the solar wind." *Astrophys. J.*, 272, 329–348.

Brueckner, G. E., R. A. Howard, M. J. Koomen, C. M. Korendyke, D. J. Michels, J. D. Moses, D. G. Socker, K. P. Dere, P. L. Lamy, A. Llebaria, M. V. Bout, R. Schwenn, G. M. Simnett, D. K. Bedford, and C. J. Eyles (1995), "The Large Angle Spectroscopic Coronagraph (LASCO)." *Solar Phys.*, 162, 357–402.

Crosby, N. B., M. J. Aschwanden, and B. R. Dennis (1993), "Frequency distributions and correlations of solar X-ray flare parameters." *Solar Phys.*, 143, 275–299.

Culhane, J. L., L. K. Harra, A. M. James, K. Al-Janabi, L. J. Bradley, R. A. Chaudry, K. Rees, J. A. Tandy, P. Thomas, M. C. R. Whillock, B. Winter, G. A. Doschek, C. M. Korendyke, C. M. Brown, S. Myers, J. Mariska, J. Seely, J. Lang, B. J. Kent, B. M. Shaughnessy, P. R. Young, G. M. Simnett, C. M. Castelli, S. Mahmoud, H. Mapson-Menard, B. J. Probyn, R. J. Thomas, J. Davila, K. Dere, D. Windt, J. Shea, R. Hagood, R. Moye, H. Hara, T. Watanabe, K. Matsuzaki, T. Kosugi, V. Hansteen, and Ø. Wikstol (2007), "The EUV Imaging Spectrometer for Hinode." *Solar Phys.*, 243, 19–61.

de Pontieu, B., S. McIntosh, V. H. Hansteen, M. Carlsson, C. J. Schrijver, T. D. Tarbell, A. M. Title, R. A. Shine, Y. Suematsu, S. Tsuneta, Y. Katsukawa, K. Ichimoto, T. Shimizu, and S. Nagata (2007), "A Tale of Two Spicules: The Impact of Spicules on the Magnetic Chromosphere." *Pub. Astron. Soc. Japan*, 59, S655–S662.

Del Zanna, G., K. P. Dere, P. R. Young, E. Landi, and H. E. Mason (2015), "CHIANTI - An atomic database for emission lines. Version 8." *Astron. Astrophys.*, 582, A56.

Delaboudinière, J.-P., G. E. Artzner, J. Brunaud, A. H. Gabriel, J. F. Hochedez, F. Millier, X. Y. Song, B. Au, K. P. Dere, R. A. Howard, R. Kreplin, D. J. Michels, J. D. Moses, J. M. Defise, C. Jamar, P. Rochus, J. P. Chauvineau, J. P. Marioge, R. C. Catura, J. R. Lemen, L. Shing, R. A. Stern, J. B. Gurman, W. M. Neupert, A. Maucherat, F. Clette, P. Cugnon, and E. L. van Dessel (1995), "EIT: Extreme-Ultraviolet Imaging Telescope for the SOHO Mission." *Solar Phys.*, 162, 291–312.

Dere, K. P., J.-D. F. Bartoe, G. E. Brueckner, J. Ewing, and P. Lund (1991), "Explosive events and magnetic reconnection in the solar atmosphere." *J. Geophys. Res.*, 96, 9399–9407.

Dere, K. P., E. Landi, H. E. Mason, B. C. Monsignori Fossi, and P. R. Young (1997), "CHIANTI - an atomic database for emission lines." *Astron. Astrophys. Suppl.*, 125.

Ding, J. Y., M. S. Madjarska, J. G. Doyle, Q. M. Lu, K. Vanninathan, and Z. Huang (2011), "Magnetic reconnection resulting from flux emergence: implications for jet formation in the lower solar atmosphere?" *Astron. Astrophys.*, 535, A95.

Domingo, V., B. Fleck, and A. I. Poland (1995), "The SOHO Mission: an Overview." *Solar Phys.*, 162, 1–37.

Doyle, J. G., A. Giunta, A. Singh, M. S. Madjarska, H. Summers, B. J. Kellett, and M. O'Mullane (2012), "The Diagnostic Potential of Transition Region Lines Undergoing Transient Ionization in Dynamic Events." *Solar Phys.*, 280, 111–124.

Doyle, J. G., B. Ishak, M. S. Madjarska, E. O'Shea, and E. Dzifćáková (2006a), "Dynamic features in the solar atmosphere with unusual spectral line enhancements and Doppler-shifts." *Astron. Astrophys.*, 451, L35–L38.

Doyle, J. G., B. Ishak, I. Ugarte-Urra, P. Bryans, and H. P. Summers (2005a), "Evidence for explosive event activity originating in the chromosphere." *Astron. Astrophys.*, 439, 1183–1189.

Doyle, J. G., M. S. Madjarska, I. Roussev, L. Teriaca, and J. Giannikakis (2002), "Temporal variability in the Doppler-shift of solar transition region lines." *Astron. Astrophys.*, 396, 255–267.

Doyle, J. G., M. D. Popescu, and Y. Taroyan (2006b), "Repetitive occurrence of explosive events at a coronal hole boundary." *Astron. Astrophys.*, 446, 327–331.

Doyle, J. G., H. P. Summers, and P. Bryans (2005b), "The effect of metastable level populations on the ionization fraction of Li-like ions." *Astron. Astrophys.*, 430, L29–L32.

Fröhlich, C., J. Romero, H. Roth, C. Wehrli, B. N. Andersen, T. Appourchaux, V. Domingo, U. Telljohann, G. Berthomieu, P. Delache, J. Provost, T. Toutain, D. A. Crommelynck, A. Chevalier, A. Fichot, W. Däppen, D. Gough, T. Hoeksema, A. Jiménez, M. F. Gómez, J. M. Herreros, T. R. Cortés, A. R. Jones, J. M. Pap, and R. C. Willson (1995), "VIRGO: Experiment for Helioseismology and Solar Irradiance Monitoring." *Solar Phys.*, 162, 101–128.

Gabriel, A. H., G. Grec, J. Charra, J.-M. Robillot, T. Roca Cortés, S. Turck-Chièze, R. Bocchia, P. Boumier, M. Cantin, E. Cespédes, B. Cougrand, J. Crétolle, L. Damé, M. Decaudin, P. Delache, N. Denis, R. Duc, H. Dzitko, E. Fossat, J.-J. Fourmond, R. A. García, D. Gough, C. Grivel, J. M. Herreros, H. Lagardère, J.-P. Moalic, P. L. Pallé, N. Pétrou, M. Sanchez, R. Ulrich, and H. B. van der Raay (1995), "Global Oscillations at Low Frequency from the SOHO Mission (GOLF)." *Solar Phys.*, 162, 61–99.

García, R. A., S. Turck-Chièze, S. J. Jiménez-Reyes, J. Ballot, P. L. Pallé, A. Eff-Darwich, S. Mathur, and J. Provost (2007), "Tracking Solar Gravity Modes: The Dynamics of the Solar Core." *Science*, 316, 1591.

Golub, L., E. Deluca, G. Austin, J. Bookbinder, D. Caldwell, P. Cheimets, J. Cirtain, M. Cosmo, P. Reid, A. Sette, M. Weber, T. Sakao, R. Kano, K. Shibasaki, H. Hara, S. Tsuneta, K. Kumagai, T. Tamura, M. Shimojo, J. McCracken, J. Carpenter, H. Haight, R. Siler, E. Wright, J. Tucker, H. Rutledge, M. Barbera, G. Peres, and S. Varisco (2007), "The X-Ray Telescope (XRT) for the Hinode Mission." *Solar Phys.*, 243, 63–86.

Golub, L. and J. M. Pasachoff (1997), *The Solar Corona*. Cambridge University Press.

Handy, B. N., L. W. Acton, C. C. Kankelborg, C. J. Wolfson, D. J. Akin, M. E. Bruner, R. Caravalho, R. C. Catura, R. Chevalier, D. W. Duncan, C. G. Edwards, C. N. Feinstein, S. L. Freeland, F. M. Friedlaender, C. H. Hoffmann, N. E. Hurlburt, B. K. Jurcevich, N. L. Katz, G. A. Kelly, J. R. Lemen, M. Levay, R. W. Lindgren, D. P. Mathur, S. B. Meyer, S. J. Morrison, M. D. Morrison, R. W. Nightingale, T. P. Pope, R. A. Rehse, C. J. Schrijver, R. A. Shine, L. Shing, K. T. Strong, T. D. Tarbell, A. M. Title, D. D. Torgerson, L. Golub, J. A. Bookbinder, D. Caldwell, P. N. Cheimets, W. N. Davis, E. E. Deluca, R. A. McMullen, H. P. Warren, D. Amato, R. Fisher, H. Maldonado, and C. Parkinson (1999), "The transition region and coronal explorer." *Solar Phys.*, 187, 229–260.

Harrison, R. A., E. C. Sawyer, M. K. Carter, A. M. Cruise, R. M. Cutler, A. Fludra, R. W. Hayes, B. J. Kent, J. Lang, D. J. Parker, J. Payne, C. D. Pike, S. C. Peskett, A. G. Richards, J. L. Gulhane, K. Norman, A. A. Breeveld, E. R. Breeveld, K. F. Al Janabi, A. J. McCalden, J. H. Parkinson, D. G. Self, P. D. Thomas, A. I. Poland, R. J. Thomas, W. T. Thompson, O. Kjeldseth-Moe, P. Brekke, J. Karud, P. Maltby, B. Aschenbach, H. Bräuninger, M. Kühne, J. Hollandt, O. H. W.

Siegmund, M. C. E. Huber, A. H. Gabriel, H. E. Mason, and B. J. I. Bromage (1995), "The Coronal Diagnostic Spectrometer for the Solar and Heliospheric Observatory." *Solar Phys.*, 162, 233–290.

Heyvaerts, J. and E. R. Priest (1983), "Coronal heating by phase-mixed shear Alfven waves." *Astron. Astrophys.*, 117, 220–234.

Hollweg, J. V. and G. Yang (1988), "Resonance absorption of compressible magnetohydrodynamic waves at thin 'surfaces'." *J. Geophys. Res.*, 93, 5423–5436.

Hovestadt, D., M. Hilchenbach, A. Bürgi, B. Klecker, P. Laeverenz, M. Scholer, H. Grünwaldt, W. I. Axford, S. Livi, E. Marsch, B. Wilken, H. P. Winterhoff, F. M. Ipavich, P. Bedini, M. A. Coplan, A. B. Galvin, G. Gloeckler, P. Bochsler, H. Balsiger, J. Fischer, J. Geiss, R. Kallenbach, P. Wurz, K.-U. Reiche, F. Gliem, D. L. Judge, H. S. Ogawa, K. C. Hsieh, E. Möbius, M. A. Lee, G. G. Managadze, M. I. Verigin, and M. Neugebauer (1995), "CELIAS - Charge, Element and Isotope Analysis System for SOHO." *Solar Phys.*, 162, 441–481.

Huang, Z., M. S. Madjarska, E. M. Scullion, L.-D. Xia, J. G. Doyle, and T. Ray (2017), "Explosive events in active region observed by IRIS and SST/CRISP." *Mon. Not. Roy. Astron. Soc.*, 464, 1753–1761.

Huang, Z., M. S. Madjarska, L. Xia, J. G. Doyle, K. Galsgaard, and H. Fu (2014), "Explosive Events on a Subarcsecond Scale in IRIS Observations: A Case Study." *Astrophys. J.*, 797, 88.

Innes, D. E., P. Brekke, D. Germerott, and K. Wilhelm (1997), "Bursts of Explosive Events in the Solar Network." *Solar Phys.*, 175, 341–348.

Innes, D. E. and L. Teriaca (2013), "Quiet Sun Explosive Events: Jets, Splashes, and Eruptions." *Solar Phys.*, 282, 453–469.

Innes, D. E. and G. Tóth (1999), "Simulations of small-scale explosive events on the Sun." *Solar Phys.*, 185, 127–141.

Ionson, J. A. (1978), "Resonant absorption of Alfvenic surface waves and the heating of solar coronal loops." *Astrophys. J.*, 226, 650–673.

Klimchuk, J. A. and S. J. Bradshaw (2014), "Are Chromospheric Nanoflares a Primary Source of Coronal Plasma?" *Astrophys. J.*, 791, 60.

Kohl, J. L., R. Esser, L. D. Gardner, S. Habbal, P. S. Daigneau, E. F. Dennis, G. U. Nystrom, A. Panasyuk, J. C. Raymond, P. L. Smith, L. Strachan, A. A. van Ballegooijen, G. Noci, S. Fineschi, M. Romoli, A. Ciaravella, A. Modigliani, M. C. E. Huber, E. Antonucci, C. Benna, S. Giordano, G. Tondello, P. Nicolosi, G. Naletto, C. Pernechele, D. Spadaro, G. Poletto, S. Livi, O. von der Lühe, J. Geiss, J. G. Timothy, G. Gloeckler, A. Allegra, G. Basile, R. Brusa, B. Wood, O. H. W. Siegmund, W. Fowler, R. Fisher, and M. Jhabvala (1995), "The Ultraviolet Coronagraph Spectrometer for the Solar and Heliospheric Observatory." *Solar Phys.*, 162, 313–356.

Krucker, S. and A. O. Benz (1998), "Energy Distribution of Heating Processes in

the Quiet Solar Corona." *Astrophys. J. Lett.*, 501, L213.

Labs, D. and H. Neckel (1968), "The Radiation of the Solar Photosphere from 2000 Å to 100 μm." *Z. Astrophys.*, 69, 1.

Lemen, J. R., A. M. Title, D. J. Akin, P. F. Boerner, C. Chou, J. F. Drake, D. W. Duncan, C. G. Edwards, F. M. Friedlaender, G. F. Heyman, N. E. Hurlburt, N. L. Katz, G. D. Kushner, M. Levay, R. W. Lindgren, D. P. Mathur, E. L. McFeaters, S. Mitchell, R. A. Rehse, C. J. Schrijver, L. A. Springer, R. A. Stern, T. D. Tarbell, J. P. Wuelser, C. Wolfson, C. J. Yanari, J. A. Bookbinder, P. N. Cheimets, D. Caldwell, E. E. Deluca, R. Gates, L. Golub, S. Park, W. A. Podgorski, R. I. Bush, P. H. Scherrer, M. A. Gummin, P. Smith, G. Auker, P. Jerram, P. Pool, R. Soufli, D. L. Windt, S. Beardsley, M. Clapp, J. Lang, and N. Waltham (2012), "The Atmospheric Imaging Assembly (AIA) on the Solar Dynamics Observatory (SDO)." *Solar Phys.*, 275, 17–40.

Madjarska, M. S., J. G. Doyle, and B. de Pontieu (2009), "Explosive Events Associated with a Surge." *Astrophys. J.*, 701, 253–259.

Mariska, J. T., G. A. Doschek, J. P. Boris, E. S. Oran, and T. R. Young, Jr. (1982), "Solar transition region response to variations in the heating rate." *Astrophys. J.*, 255, 783–796.

McIntosh, S. W. and B. De Pontieu (2009), "Observing Episodic Coronal Heating Events Rooted in Chromospheric Activity." *Astrophys. J. Lett.*, 706, L80–L85.

Mitalas, R. and K. R. Sills (1992), "On the photon diffusion time scale for the sun." *Astrophys. J.*, 401, 759.

Moriyasu, S., T. Kudoh, T. Yokoyama, and K. Shibata (2004), "The Nonlinear Alfvén Wave Model for Solar Coronal Heating and Nanoflares." *Astrophys. J. Lett.*, 601, L107–L110.

Mueller, B. A. (2015), *The Source and Time Variability of the Slow Solar Wind*. Master's thesis, Rice University.

Müller, D. A. N., V. H. Hansteen, and H. Peter (2003), "Dynamics of solar coronal loops. I. Condensation in cool loops and its effect on transition region lines." *Astron. Astrophys.*, 411, 605–613.

Müller-Mellin, R., H. Kunow, V. Fleißner, E. Pehlke, E. Rode, N. Röschmann, C. Scharmberg, H. Sierks, P. Rusznyak, S. McKenna-Lawlor, I. Elendt, J. Sequeiros, D. Meziat, S. Sanchez, J. Medina, L. Del Peral, M. Witte, R. Marsden, and J. Henrion (1995), "COSTEP - Comprehensive Suprathermal and Energetic Particle Analyser." *Solar Phys.*, 162, 483–504.

Ning, Z., D. E. Innes, and S. K. Solanki (2004), "Line profile characteristics of solar explosive event bursts." *Astron. Astrophys.*, 419, 1141–1148.

O'Dwyer, B., G. Del Zanna, H. E. Mason, M. A. Weber, and D. Tripathi (2010), "SDO/AIA response to coronal hole, quiet Sun, active region, and flare plasma." *Astron. Astrophys.*, 521, A21.

Ofman, L. and M. J. Aschwanden (2002), "Damping Time Scaling of Coronal Loop Oscillations Deduced from Transition Region and Coronal Explorer Observations." *Astrophys. J. Lett.*, 576, L153–L156.

Parker, E. N. (1988), "Nanoflares and the solar X-ray corona." *Astrophys. J.*, 330, 474–479.

Parnell, C. E. and P. E. Jupp (2000), "Statistical Analysis of the Energy Distribution of Nanoflares in the Quiet Sun." *Astrophys. J.*, 529, 554–569.

Pesnell, W. D., B. J. Thompson, and P. C. Chamberlin (2012), "The Solar Dynamics Observatory (SDO)." *Solar Phys.*, 275, 3–15.

Peter, H., S. Bingert, J. A. Klimchuk, C. de Forest, J. W. Cirtain, L. Golub, A. R. Winebarger, K. Kobayashi, and K. E. Korreck (2013), "Structure of solar coronal loops: from miniature to large-scale." *Astron. Astrophys.*, 556, A104.

Phillips, K. J. H. (1992), *Guide to the Sun*, 1st edition. Cambridge University Press.

Priest, E. (2014), *Magnetohydrodynamics of the Sun*. Cambridge University Press.

Reale, F. (2014), "Coronal Loops: Observations and Modeling of Confined Plasma." *Living Reviews in Solar Physics*, 11, 4.

Reale, F., G. Peres, S. Serio, R. M. Betta, E. E. DeLuca, and L. Golub (2000), "A Brightening Coronal Loop Observed by TRACE. II. Loop Modeling and Constraints on Heating." *Astrophys. J.*, 535, 423–437.

Roussev, I., J. G. Doyle, K. Galsgaard, and R. Erdélyi (2001), "Modelling of solar explosive events in 2D environments. III. Observable consequences." *Astron. Astrophys.*, 380, 719–726.

Scherrer, P. H., R. S. Bogart, R. I. Bush, J. T. Hoeksema, A. G. Kosovichev, J. Schou, W. Rosenberg, L. Springer, T. D. Tarbell, A. Title, C. J. Wolfson, I. Zayer, and MDI Engineering Team (1995), "The Solar Oscillations Investigation - Michelson Doppler Imager." *Solar Phys.*, 162, 129–188.

Scherrer, P. H., J. Schou, R. I. Bush, A. G. Kosovichev, R. S. Bogart, J. T. Hoeksema, Y. Liu, T. L. Duvall, J. Zhao, A. M. Title, C. J. Schrijver, T. D. Tarbell, and S. Tomczyk (2012), "The Helioseismic and Magnetic Imager (HMI) Investigation for the Solar Dynamics Observatory (SDO)." *Solar Phys.*, 275, 207–227.

Shimizu, T. (1995), "Energetics and Occurrence Rate of Active-Region Transient Brightenings and Implications for the Heating of the Active-Region Corona." *Pub. Astron. Soc. Japan*, 47, 251–263.

Sterling, A. C. (2000), "Solar Spicules: A Review of Recent Models and Targets for Future Observations - (Invited Review)." *Solar Phys.*, 196, 79–111.

Stix, M. (2004), *The Sun: An Introduction*, 2nd edition. Springer.

Taroyan, Y. and S. J. Bradshaw (2014), "Forward-Modeling of Doppler Shifts in EUV Spectral Lines." *Solar Phys.*, 289, 1959–1970.

Taroyan, Y., S. J. Bradshaw, and J. G. Doyle (2006), "Nanoflare heating of coronal loops: hydrodynamic response and observational consequences." *Astron. Astrophys.*, 446, 315–325.

Taroyan, Y. and R. Erdélyi (2009), "Heating Diagnostics with MHD Waves." *Space Sci. Rev.*, 149, 229–254.

Taroyan, Y., R. Erdélyi, and S. J. Bradshaw (2011), "Observational Signatures of Impulsively Heated Coronal Loops: Power-Law Distribution of Energies." *Solar Phys.*, 269, 295–307.

Teriaca, L., D. Banerjee, A. Falchi, J. G. Doyle, and M. S. Madjarska (2004), "Transition region small-scale dynamics as seen by SUMER on SOHO." *Astron. Astrophys.*, 427, 1065–1074.

Teriaca, L., M. S. Madjarska, and J. G. Doyle (2002), "Transition region explosive events: Do they have a coronal counterpart?" *Astron. Astrophys.*, 392, 309–317.

Torsti, J., E. Valtonen, M. Lumme, P. Peltonen, T. Eronen, M. Louhola, E. Riihonen, G. Schultz, M. Teittinen, K. Ahola, C. Holmlund, V. Kelhä, K. Leppälä, P. Ruuska, and E. Strömmer (1995), "Energetic Particle Experiment ERNE." *Solar Phys.*, 162, 505–531.

Tsuneta, S., K. Ichimoto, Y. Katsukawa, S. Nagata, M. Otsubo, T. Shimizu, Y. Suematsu, M. Nakagiri, M. Noguchi, T. Tarbell, A. Title, R. Shine, W. Rosenberg, C. Hoffmann, B. Jurcevich, G. Kushner, M. Levay, B. Lites, D. Elmore, T. Matsushita, N. Kawaguchi, H. Saito, I. Mikami, L. D. Hill, and J. K. Owens (2008), "The Solar Optical Telescope for the Hinode Mission: An Overview." *Solar Phys.*, 249, 167–196.

Warren, H. P., I. Ugarte-Urra, P. R. Young, and G. Stenborg (2011), "The Temperature Dependence of Solar Active Region Outflows." *Astrophys. J.*, 727, 58.

Wentzel, D. G. (1974), "Coronal heating by Alfven waves." *Solar Phys.*, 39, 129–140.

Wentzel, D. G. (1976), "Coronal heating by Alfven waves. II." *Solar Phys.*, 50, 343–360.

Wilhelm, K., W. Curdt, E. Marsch, U. Schühle, P. Lemaire, A. Gabriel, J. C. Vial, M. Grewing, M. C. E. Huber, S. D. Jordan, A. I. Poland, R. J. Thomas, M. Kühne, J. G. Timothy, D. M. Hassler, and O. H. W. Siegmund (1995), "SUMER - Solar Ultraviolet Measurements of Emitted Radiation." *Solar Phys.*, 162, 189–231.

Winebarger, A. R., A. G. Emslie, J. T. Mariska, and H. P. Warren (2002), "Energetics of Explosive Events Observed with SUMER." *Astrophys. J.*, 565, 1298–1311.

Winebarger, A. R., R. W. Walsh, R. Moore, B. De Pontieu, V. Hansteen, J. Cirtain, L. Golub, K. Kobayashi, K. Korreck, C. DeForest, M. Weber, A. Title, and S. Kuzin (2013), "Detecting Nanoflare Heating Events in Subarcsecond Inter-moss Loops Using Hi-C." *Astrophys. J.*, 771, 21.

Woods, T. N., F. G. Eparvier, R. Hock, A. R. Jones, D. Woodraska, D. Judge, L. Didkovsky, J. Lean, J. Mariska, H. Warren, D. McMullin, P. Chamberlin, G. Berthiaume, S. Bailey, T. Fuller-Rowell, J. Sojka, W. K. Tobiska, and R. Viereck (2012), "Extreme Ultraviolet Variability Experiment (EVE) on the Solar Dynamics Observatory (SDO): Overview of Science Objectives, Instrument Design, Data Products, and Model Developments." *Solar Phys.*, 275, 115–143.